SODIUM-COUPLED LIGAND BINDING AND GATING MECHANISM OF A GLUTAMATE TRANSPORTER HOMOLOGUE

A Dissertation

Presented to the Faculty of the Weill Cornell Graduate School

of Medical Sciences

in Partial Fulfillment of the Requirements for the Degree of

Doctor of Philosophy

By

SeCheol Oh

December 2017

© 2017 SeCheol Oh

SODIUM-COUPLED LIGAND BINDING AND GATING MECHANISM OF A GLUTAMATE TRANSPORTER HOMOLOGUE

SeCheol Oh, Ph.D.

Cornell University 2017

The excitatory amino acid transporters (EAATs) are membrane transport proteins that clear neurotransmitter glutamate from the synaptic cleft and terminate neurotransmission. The clearance of glutamate is critical for brain functions because accumulated glutamate in the synaptic cleft is toxic for neuronal cells, and ultimately induces brain damage. Consistently, malfunction of EAATs is associated with brain disease such as epilepsy, ataxia and neurodegeneration.

To transport glutamate into cytoplasm, EAATs harness free energy stored in the form of ionic electrochemical gradients across the membrane. They couple transport of one glutamate to symport of three sodium ions and a proton, and to antiport of a potassium ion. Many elucidated aspects of the mechanism of ion-coupled glutamate transport are based on studies of its archaeal homologue, Glt_{Ph}, a sodium-coupled aspartate transporter from *Pyrococcus horikoshii*. Glt_{Ph} is a great structural and functional framework to understand sodium-substrate coupling in the family of glutamate transporters. First, like EAATs, Glt_{Ph} couples transport of one aspartate to symport of three sodium ions. Second, Glt_{Ph} has sequence identity with EAATs of ca 37% overall, and higher homology in sodium and substrate binding sites. Third, crystal structures of Glt_{Ph} in key functional states have been determined to high resolutions.

It has been shown that sodium and aspartate binding to Glt_{Ph} are tightly coupled. In the absence of sodium, aspartate shows no appreciable affinity to Glt_{Ph}, but in the presence of millimolar sodium concentrations, aspartate binds with nanomolar affinity. However, the molecular mechanism of the tight sodium-aspartate coupling remains unclear. To investigate the sodium-coupled mechanism, we crystallized Glt_{Ph} in apo, sodium-bound and sodium/aspartate-bound states. Comparison of the structures shows that sodium binding induces exposure of substrate binding site to the solvent upon opening of the extracellular gate and a conformational change of a highly conserved motif in substrate binding site, which is important in both aspartate and sodium binding. In addition, we found a new cation binding site, which may serve as a potassium binding site in EAATs.

We further investigated how sodium ion binding affects ligand release and binding to Glt_{Ph} in a cytoplasmic-facing conformation. The kinetics of inhibitor binding, which mimics the earlier events of substrate binding, suggests that binding follows a sodium-dependent ‘conformational selection’ mechanism, whereby rate-limiting binding of the first sodium ion stabilizes conformation of the transporter competent to bind substrate. The kinetics of ligand dissociation suggests that dissociation of one or two sodium ions precedes and determines the rate of ligand dissociation. Overall, aspartate binding kinetics suggest that sodium ion bindings before and after controls the rate of aspartate binding and dissociation.

BIOGRAPHICAL SKETCH

SeCheol Oh was born in Seoul, South Korea. He studied chemistry at the Korea Advanced Institute of Science and Technology (KAIST), where he obtained his B.S. degree and M.S. degree. In his M.S. study, he determined crystal structures of hagfish Variable Lymphocyte Receptors, important proteins in the agnathan adaptive immune system. After M.S., he served as an army officer for three years in Korea Military Academy. Then, he enrolled in the graduate program at Weill Cornell Medical College in 2010. He joined the laboratory of Dr. Olga Boudker. In Boudker lab, he investigated ion-coupled mechanisms of sodium-coupled amino acid transporter Glt_{Ph}, which is the central topic of this dissertation.

To my family, for their love and support

ACKNOWLEDGMENTS

First of all, I would like to thank my advisor Dr. Olga Boudker for the opportunity to study and work in her lab. In addition to her passion for science, the inspiration and guidance she has provided me have made this journey possible. I am indebted to her for her generous support and care throughout the years. I would also like to thank the members of my thesis committee, Dr. David Eliezer and Dr. Alessio Accardi, who have been very insightful and supportive throughout my graduate studies. I hope that someday I could help others in scientific community as they have done for me. I am also grateful to Dr. Kirk Deitsch for serving as the chairperson for my thesis defense.

I would like to thank all the past and present members of Boudker lab. Their advice and encouragement have been invaluable. I would like to specially acknowledge the members of the lab who have contributed directly to this thesis work including Dr. Nicolas Reyes, and Dr. Gregory Verdon on functional and structural studies of Glt_{Ph} together.

Lastly, I am most grateful to my family for their love and support.

TABLE OF CONTENTS

LIST OF FIGURES

LIST OF TABLES

CHAPTER 1

INTRODUCTION

1.1. Neurotransmitter glutamate and glutamate transporters

Glutamate is a most abundant excitatory neurotransmitter in the brain. In presynaptic neurons, glutamate molecules are packaged into synaptic vesicles and released into the synaptic cleft via exocytosis (Figure 1.1). The released glutamate binds to ionitropic or metabotrpic glutamate receptors on the postsynaptic membrane, inducing changes of ion permeability and membrane potential of the postsynaptic neurons. Glutamate molecules are transported from the synaptic cleft into the cytoplasm of presynaptic neurons and glial cells by excitatory amino acid transporters (EAATs). Therefore, low glutamate concentration in the synaptic cleft is maintained, likely below in nanomolar range (Danbolt, et al., 2001). When EAATs malfunction, glutamate accumulated in the synaptic cleft over-activates glutamate receptors and increases membrane permeability for calcium (Ca^{2+}) ion. Increased cytoplasmic Ca^{2+} concentrations lead to onset of apoptosis, and ultimately to brain damage. Indeed, the malfunction and decreased expression of EAATs is associated with epilepsy and neurodegeneration as well as poor recovery from ischemia, stroke and traumatic brain damage (Maragakis and Rothstein, 2004, Fukamachi, et al., 2001, Rao et al., 2001, Watase et al., 1998, Tanaka et al., 1997).

There are five EAAT subtypes in humans. EAAT2 is universally expressed throughout the body; EAAT1 is expressed in glia and EAAT3 in neurons. EAAT4 and EAAT5 are expressed in specialized brain ganglia and in

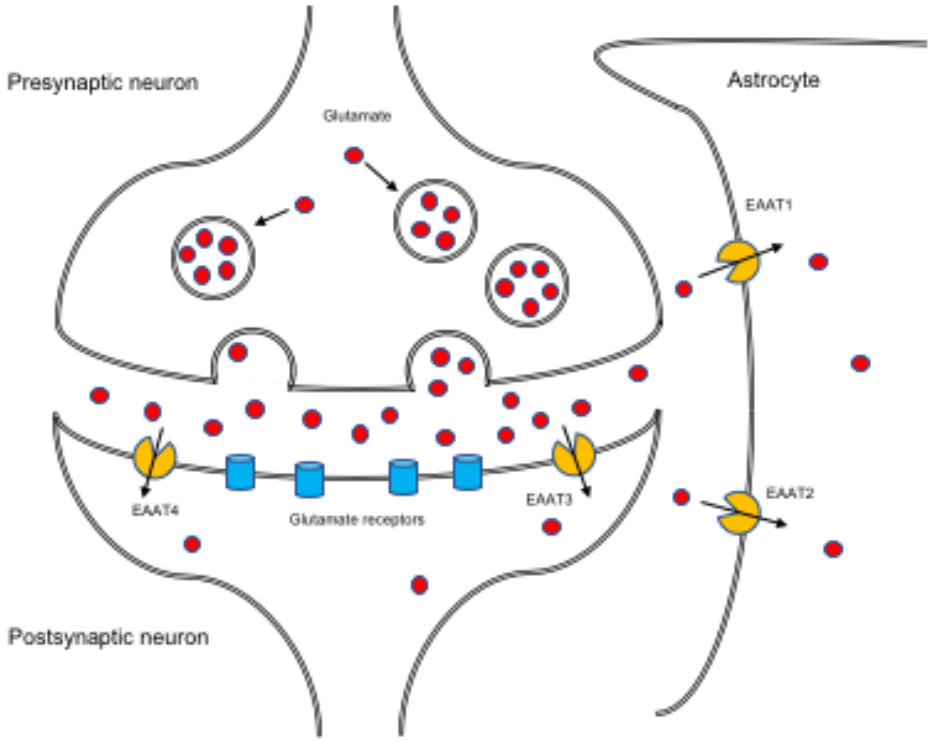

Figure 1.1. Schematic diagram of a glutamatergic synapse.
In presynaptic neurons, glutamate (red circles) is accumulated in synaptic vesicles, and released into the synapse by exocytosis. Released glutamate binds to glutamate receptors (blue) change the membrane potential. Glutamate is removed from the synapse by glutamate transporters (yellow) expressed on the membranes of postsynaptic neurons and astrocytes.

retina, respectively (Danbolt, 2001, Vandenberg and Ryan, 2013) (Figure 1.1). EAATs terminate neurotransmission by translocating glutamate from the synaptic cleft into the cytoplasm across the membrane. Because glutamate uptake is a thermodynamically 'uphill' process, glutamate transporters harness the free energy for the uptake from the ionic gradient across the membrane. One glutamate molecule is transporter together with three Na^+ ions and a H^+, and one K^+ ion is counter-transported (Zerangue and Kavanaugh, 1996). Despite the abundance of functional studies on EAATs, the key questions regarding the glutamate transport mechanism, such as where do substrate and ions binding, how substrate binding is coupled to ion-binding, and how EAATs change their conformation to open and close the sites to the extracellular and intracellular solution, remained unanswered because of the lack of structural information.

1.2. Glt_{Ph}, crystal structures and transport mechanism

Glt_{Ph}, a membrane protein from *Pyrococcus horikoshii*, is an archaeal homologue of EAATs with 37 % amino acid sequence identity. Like EAATs, Glt_{Ph} transports one aspartate molecule across the cell membrane together with three Na^+ ions (Groeneveld and Slotboom, 2010). Otherwise, its function is independent of H^+ and K^+, unlike EAATs (Ryan et al., 2009).

A remarkable property of Glt_{Ph} is its crystallizability. Crystal structures of Glt_{Ph} have guided us to better understanding of the ion-coupled transport mechanism. Glt_{Ph} is an excellent model system to study ion-coupled, especially Na^+-coupled, mechanism of EAATs. The first Glt_{Ph} structure showed that Glt_{Ph} exists as a homo-trimer and has bowl-like shape (Figure 1.2a, Yernool et al., 2004). It has 8 trans-membrane domains (TMs) and two re-

entrant ‘hairpin’ domains (HPs) (Figure 1.2b, Yernool et al., 2004). Substrate binding site is located in the middle of the membrane and is covered by HP2 domain. Glt_{Ph} structures in L-asp-bound and an inhibitor TBOA-bound states show that HP2 domain acts as an extracellular gate (Figure 1.2c, Boudker, 2007). Moreover, the structures show details of the substrate and ion binding coordination (Figure 1.2d-e, Boudker, 2007). Residues from TM7, TM8, HP1 and HP2 make up substrate-binding site. The key residues, which are highly conserved in Glt_{Ph} and EAATs interact with substrate: R397 and T314 coordinate directly γ-carboxyl group of the substrate aspartate. T398 and D394 interact with the amino group of the substrate aspartate. Na1 and Na2 sites were identified using thallium soaks of L-asp bound crystals and detecting anomalous scattering from the metal. In Na1 site, D405 is a key residue that coordinates Na^+ ion in the site. Carbonyl groups of N310 and N401 also contribute to the site. Na2 site between the carboxyl-terminal ends of HP2a and TM7a helices. Carbonyl groups of T352, T308, S349 and I350 interact with the ion in the site. In the inhibitor-bound state, Na2 site was not fully formed because HP2 is open in the structure (Figure 1.2e). Therefore, it was suggested that Na2 site is the last Na^+ binding site among the three Na^+ binding sites to be occupied by the ion (Boudker et al., 2007). Na3 site has not been identified yet. However, in a crystallographic study of another closely related archaeal homologue, Na3 site has been tentatively identified (Guskov et al., 2016). Because of its high homology with Glt_{Ph} in this site, it is strongly believed that Glt_{Ph} has the same Na3 site (Figure 1.2f).

Crystal structure of Glt_{Ph} in an inward-facing state yielded insight into the transport mechanism. The structure shows that Glt_{Ph} protomer consists of two domains; the scaffold domain (TM1, TM2, TM4 and TM5), which is nearly

Figure 1.2. Crystal structures of Glt_{Ph}.
a. Ribbon representation of the trimer, in which the protomers are red, blue and green, viewed from the extracellular side of the membrane.
b. Schematic representation of Glt_{Ph} transmembrane topology.
c. Solvent- accessible surface view of a single subunit in complex with TBOA (left) and with aspartate (right); the 3L4 loop (green), TM7 (orange), HP1 (yellow), HP2 (red) and TM8 (magenta).
d. Aspartate-binding site showing HP1 (yellow), TM7 (orange), HP2 (red) and TM8 (magenta). A remarkable number of polar contacts solvate the highly-charged substrate and include interactions with D394, main-chain carbonyls of R276 (HP1) and V355 (HP2), the amide nitrogen of N401 (TM8), the hydroxyl of T398 (TM8), the main-chain nitrogen of S278, the guanidinium group of R397 (TM8), the hydroxyl of T314 (TM7) and the main-chain nitrogen of G359 (HP2).
e. Na^+ ion binding sites. Left, oxygen atoms that are within 3.5 Å of the sodium ions are labelled and connected to the sodium ions by dashed lines. Light blue arrows represent the dipole moments of helices TM7a and HP2a. Right, Opening of HP2 observed in the TBOA-bound structure destroys sodium site 2. The dashed arrow indicates the direction of HP2 motion in the TBOA-bound state. Sodium bound at site 2 in aspartate-bound Glt_{Ph} is shown as a sphere, with coordinating oxygen interactions depicted by dashed lines.
f. a proposed Na3 site.
(Adapted from Yernool et al., 2004, Boudker et al., 2007, Verdon et al., 2014).

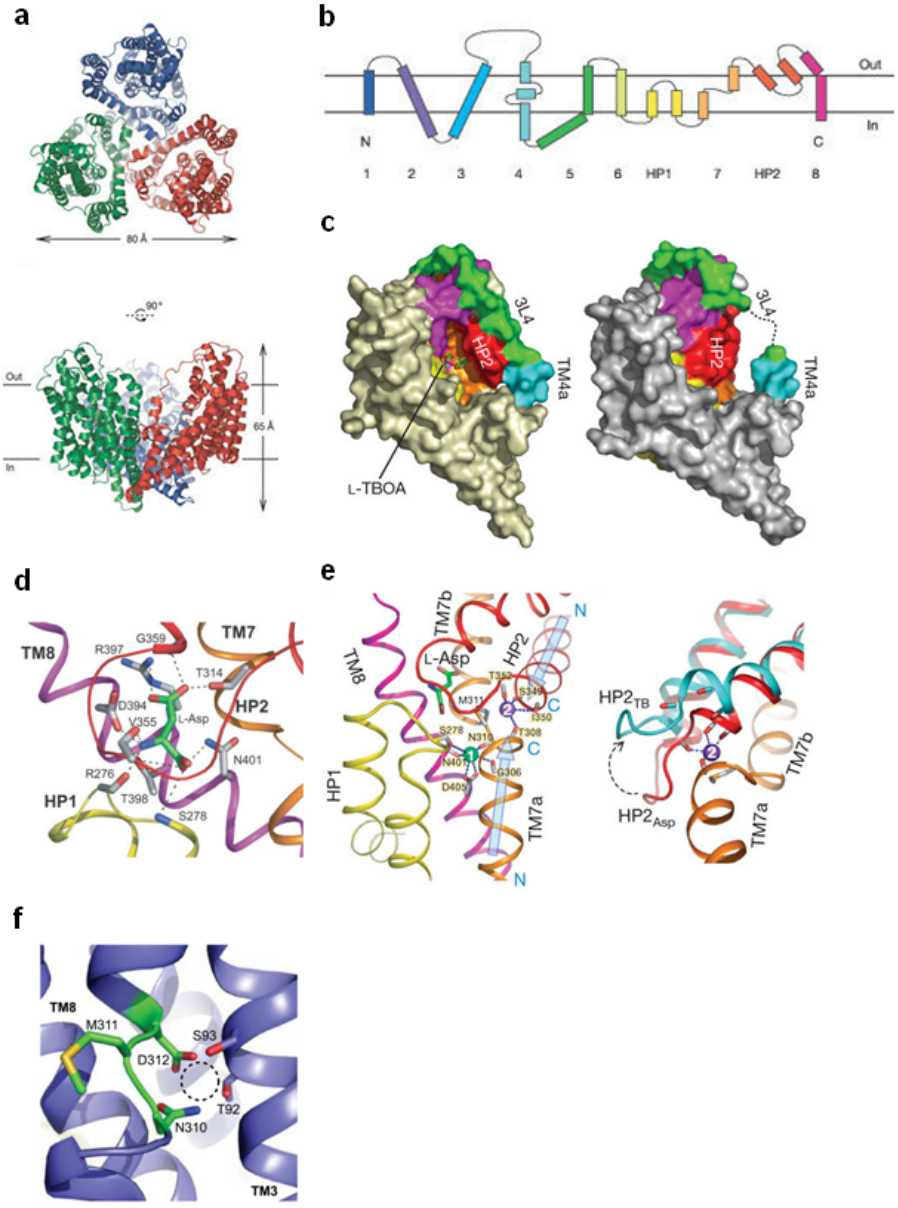
a
80 Å
90°
Out
In
65 Å
b
Out
In
N
C
1
2
3
4
5
6
HP1
7
HP2
8
c
3L4
HP2
TM4a
L-TBOA
d
TM8
TM7
R397
G359
T314
D394
V355
L-Asp
HP2
N401
R276
HP1
T398
S278
e
TM7b
TM8
L-Asp
HP2
N
C
HP1
TM7a
N
HP2TB
HP2Asp
TM7b
TM7a
f
TM8
M311
S93
D312
T92
N310
TM3

rigid throughout the transport cycle, and the transport domain (TM3, TM6, TM7, TM8, HP1 and HP2), which is mobile unit that harbors substrate and ion binding sites (Figure 1.3a, Reyes et al., 2009). Aspartate and Na^+ binding sites are closer to the cytoplasmic side in the crystal structure of Glt_{Ph} in the inward-facing state. Based on structural comparison of Glt_{Ph} in the outward- and inward-facing states, an 'elevator' mechanism of transport has been suggested (Figure 1.3b, Reyes et al., 2009). According to the mechanism, the transport domain moves across the membrane as a rigid body, translocating the substrate and coupled ions. To date, more transporters have been reported to follow the elevator mechanism (Lee et al., 2013, Mancusso et al., 2012, Mulligan et al., 2016, Johnson et al., 2012, Bolla et al., 2015, Su et al., 2015, Coincon et al., 2016). The elevator along with rocker-stitch and rocking bundle mechanisms are the most commons mechanisms of membrane transporters (Drew and Boudker, 2016).

1.3. Functional studies of Glt_{Ph}

Together with the structural studies, functional studies of Glt_{Ph} have enriched our understanding of the family. A wide variety of methodologies have been used: Reconstitution of protein in liposomes, single-molecule Forster resonance energy transfer (smFRET), continuous wave and EPR double electron-electron resonance (DEER) spectroscopy, isothermal titration calorimetry (ITC), fluorescence-based assay, and so on.

The stoichiometry of the Na^+-coupled uptake was determined using reconstituted proteoliposomes and radioactive ^{14}C-aspartate and $^{22}Na^+$ (Groeneveld and Slotboom, 2010). The established stoichiometry was 1:3, the

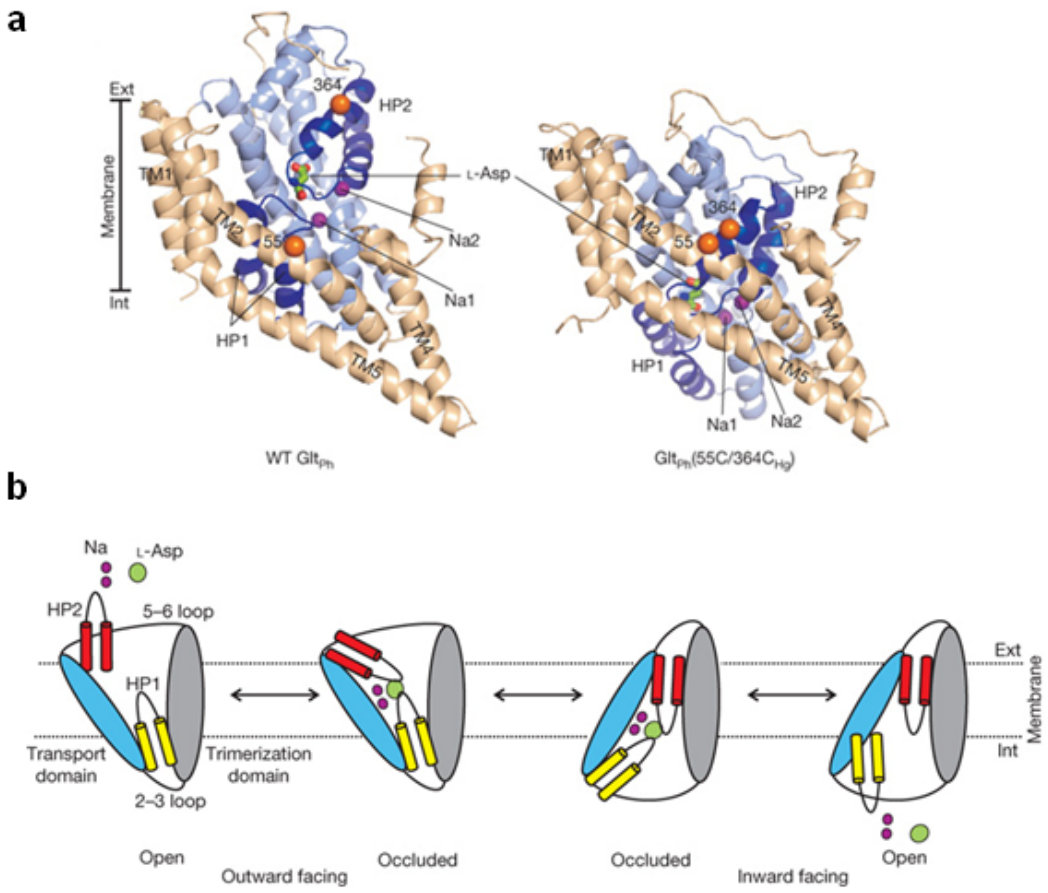

Figure 1.3. Elevator mechanism of Glt_{Ph}.
a. Cartoon representation of the single protomers. Wild-type (WT) Glt_{Ph} and $Glt_{Ph}(55C/364C_{Hg})$ are shown on the left and right, respectively. TM1, TM2, TM4 and TM5 are colored wheat, with the reminder of the protomer light blue. Substrate and Na^+ ions are shown as stick and purple spheres, respectively. **b**. Schematic model of elevator mechanism. Shown is a single transporter protomer. Substrate and sodium binding to the outward and inward facing states is coupled to the closure of the extracellular and intracellular gates, HP2 (red) and HP1 (yellow), respectively. Isomerization between the outward and inward facing occluded states occurs upon movement of the transport domain (blue), relative to the trimerization domain (grey). The inward facing open state has not been structurally characterized and is hypothetical.
Reprinted with permission of Nature Publishing Group (from Reyes et al., 2009).

same as in EAATs. Uptake turnover rate at room temperature (RT) is 0.005 s^{-1}. It means that the transport cycle of Glt_{Ph} is very slow at RT, unlike transport cycle of EAATs, which turn over in milliseconds (Arriza et al., 1994, Bergles et al., 2002, Fairman et al., 1995, Grewer et al., 2000, Tzingounis et al., 2007, Wadiche et al., 1995, Wadiche et al., 1998, Vandenberg and Ryan, 2013). The basis of the difference between the uptake rates of EAATs and Glt_{Ph} remains unanswered. Also, a recent study showed that the substrate uptake might be affected by lipid environment (McIlwain et al., 2016).

The first smFRET study on Glt_{Ph} showed that the aspartate-loaded transporters exist in two modes: dynamic mode, in which translocation across the membrane occurs frequently, and quiescent mode, in which translocation does not occur for an extended period of time. It was suggested that the switch to the dynamic mode is based on dislodging of the transport domain from the scaffold domain (Akyuz et al., 2013). Another smFRET study shows that each protomer in a homo-trimer functions independently to each other (Erkens et al., 2013).

By using ITC, fluorescence-based assay and double-cysteine mutants to Glt_{Ph} conformationally constrained in either outward- or inward-facing state, Nicolas Reyes and I studied energetics of Na^+-coupled aspartate binding from the extracellular and the cytoplasmic side. Aspartate binding depends steeply on Na^+ concentration consistent that all three Na^+ ions being coupled to aspartate binding. Heat capacity change (ΔCp) measurements suggested that L-asp binding in the inward-facings state is more dynamic, complex process than in the outward-facing state (Reyes et al., 2013).

DEER spectroscopy was used to study state distribution of Glt_{Ph} under various conditions, in other words, conformational ensemble. The study,

showed that protomers sample the inward- and outward-facing state with almost equal probabilities and the energy difference between the states is small (-0.25 ~ 0.3 kcal mol^{-1}) (Georgieva et al., 2013).

EPR spectroscopy was used to detect local conformational changes of the extracellular gate HP2 in Glt_{Ph} (Focke et al., 2011). Surprisingly, HP2 appeared to be in a similar conformation in the apo-, asp-bound state. Moreover, Na^+ and aspartate binding induced opposite movement of HP2. The authors hypothesized that Na^+ binding induces opening of HP2 while the consequent aspartate binding closes the gate.

Kinetic study is also a powerful approach to understand ligand binding mechanism. Using tryptophan mutants sensitive to ion and substrate binding, and stopped-flow assay, kinetics of Na^+ and substrate binding to Glt_{Ph} were studied. In a kinetics study, one or two slow Na^+ binding precedes the relatively fast substrate binding. It implies that the first, slow Na^+ binding is a rate-determining step (Hanelt et al., 2015). In another kinetics study, it was suggested that substrate binding to Na^+-bound transporter follows 'induced fit' mechanism. It implies that conformational change occurs after initial substrate binding, which might be upon the third Na^+ binding occurs after substrate binding (Ewers et al., 2013). The weakness of these studies was that they were conducted on an unconstrained Glt_{Ph}, which was free to sample both outward- and inward-facing states, complicating kinetic analysis.

1.4. Overview of dissertation

While earlier crystallographic studies outlined the elevator mechanism of sodium and aspartate transport by Glt_{Ph}, important questions remained unanswered: what is the structure of 'empty' transporter during the return step

of the transport cycle; what is the molecular mechanism of coupledand aspartate binding and how uncoupled transport of Na+ ions is prevented? To answer the questions, we solved crystal structures of Glt_{Ph} in several different states and studied the kinetics of ligand binding and release in the inward-facing state.

In chapter 2, I describe the crystal structures of Glt_{Ph} in apo, Na^+-bound, and Na^+/L-asp bound states. The structures show that Na^+ binding reshapes L-asp binding site and opens the extracellular gate HP2 in a manner that would prevent translocation of Na^+ ions alone. Also, I show the crystal structure of Glt_{Ph} in an apo, inward-facing state. Comparison with apo outward-facing state reveals that the isomerization of the unloaded transporter between the inward- and the outward-facing state involves a rigid-body motion of the transport domain, similar to that of the substrate-loaded transporter. In addition, we identified a new cation binding site. The location of the site suggests that it might mimic K^+-binding sites in in EAATs; based on this, we proposed a potential mechanism of K+ antiport in mammalian transporters. Based on the structures, we propose a scheme of transport cycle of Glt_{Ph} and EAATs describing ion-coupled global and local conformational changes. These studies were conducted in collaboration with Gregory Verdon and published in eLife (Verdon et al., 2014).

In chapter 3, I show a kinetic study of L-asp and inhibitor binding and dissociation in a Glt_{Ph} variant conformationally constrained in the inward-facing state. Taken together these studies suggest a scheme of coupled binding and dissociation of three Na^+ ions and L-asp : one Na^+ ion binds first in a rate-limiting step establishing a conformation of the transporter competent to bind substrate. One Na^+ ion binds last and is in a rapid equilibrium between bound

and free states; its release is prerequisite for the release of L-asp. The third Na^+ ion binds before L-asp when present at high concentrations but after L-asp when present at low concentration; regardless of the order of binding its release is also needed for L-asp release. Manuscript describing these studies is in preparation for submission.

In chapter 4, I summarize our findings and suggest future studies to further understand the sodium-coupled mechanism of Glt_{Ph} and EAATs.

CHAPTER 2

Coupled ion binding and structural transitions along the transport cycle of glutamate transporters*

2.1 Abstract

Membrane transporters that clear the neurotransmitter glutamate from synapses are driven by symport of sodium ions and counter-transport of a potassium ion. Previous crystal structures of a homologous archaeal sodium and aspartate symporter showed that a dedicated transport domain carries the substrate and ions across the membrane. Here, we report new crystal structures of this homologue in ligand-free and ions-only bound outward- and inward-facing conformations. We show that after ligand release, the apo transport domain adopts a compact and occluded conformation that can traverse the membrane, completing the transport cycle. Sodium binding primes the transport domain to accept its substrate and triggers extracellular gate opening, which prevents inward domain translocation until substrate binding takes place. Furthermore, we describe a new cation-binding site ideally suited to bind a counter-transported ion. We suggest that potassium binding at this site stabilizes the translocation-competent conformation of the unloaded transport domain in mammalian homologues.

*Verdon, G., Oh, S., Serio, R.N., & Boudker, O. Coupled ion binding and structural transitions along the transport cycle of glutamate transporters. *eLife* (2014).

2.2 Introduction

Glutamate transporters, or excitatory amino acid transporters (EAATs), reside in the plasma membranes of glial cells and neurons, where they catalyze the re-uptake of the neurotransmitters glutamate and aspartate (L-asp) (Danbolt 2001). EAATs terminate neurotransmission events supporting memory formation and cognition, and prevent excitotoxicity caused by overstimulation of glutamate receptors. Dysfunction of EAATs is linked to neurological disorders, poor recovery from stroke and traumatic brain injuries (Yi and Hazell, 2006; Sheldon and Robinson, 2007; Kim et al., 2011). To maintain steep trans-membrane glutamate gradients, EAATs transport one substrate molecule together with three sodium ions (Na^+) and one proton. After their release into the cytoplasm, counter-transport of one potassium ion (K^+) resets the transporter for the next cycle (Zerangue and Kavanaugh, 1996; Levy et al., 1998; Owe et al., 2006).

Key mechanistic and structural insights into this family of transporters come from studies on an archaeal homologue from *Pyrococcus horikoshii*, Glt_{Ph} (Figure 2.1), which symports L-asp together with three Na^+ ions (Groeneveld and Slotboom, 2010); however, it shows no dependence on counter-transport of K^+ under the conditions tested (Ryan et al., 2009). Glt_{Ph}, like EAATs, is a homo-trimer (Gendreau et al., 2004; Yernool et al., 2004). Each protomer consists of a central scaffolding trimerization domain and a peripheral transport domain containing the substrate and ion binding sites (Boudker et al., 2007; Reyes et al., 2009). When bound to Na^+ and L-asp ('fully bound' from here on), each transport domain moves by ~15 Å across the membrane from an outward- to an inward-facing position, in which the substrate binding site is near the extracellular solution and the cytoplasm,

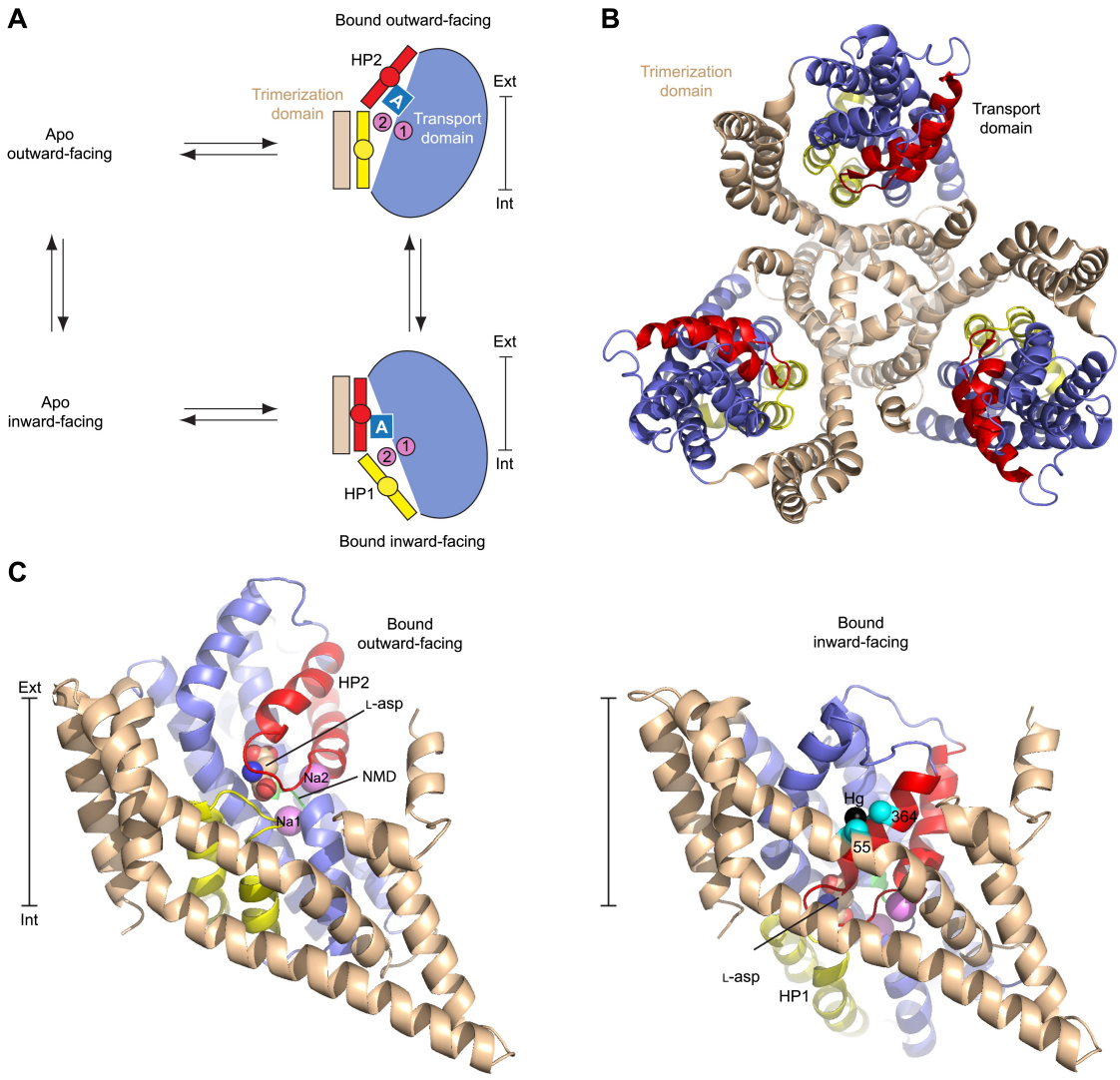

Figure 2.1. Alternating access mechanism in Glt_{Ph}.
(**A**) The transporter consists of a rigid trimerization domain (light brown) and a dynamic transport domain (blue, with HP1 yellow and HP2 red). The apo outward-facing transporter binds the substrate (blue square) and Na^+ ions (pink circles) within the transport domain under the tip of HP2. The transport domain moves into the inward-facing state, in which the ligands are occluded from the cytoplasm by the tips of HP1 and HP2, and then released. (**B**) Glt_{Ph} trimer viewed from the extracellular medium. (**C**) Single protomers of the outward-facing Glt_{Ph} (PDB code 2NWX) (left), and Glt_{Ph}^{in} (PDB code 3KBC) (right). Cα atoms of the cross-linked cysteine residues and Hg^{2+} ion are shown as spheres. The bar next to the structures indicates approximately the thickness of the membrane, separating the extracellular (Ext) and intracellular (Int) solutions.

respectively (Reyes et al., 2009). Structurally symmetric helical hairpins, HP1 and HP2, occlude the bound substrate from the solvent and are thought to serve as gates (Boudker et al., 2007; Huang and Tajkhorshid, 2008; Shrivastava et al., 2008; Reyes et al., 2009; DeChancie et al., 2010; Focke et al., 2011; Zomot and Bahar, 2013). Two Na^+-binding sites (Na1 and Na2), neither of which directly coordinates the substrate, were identified crystallographically using thallium (Tl^+) (Boudker et al., 2007). The location of the third Na^+-binding site is being debated (Holley and Kavanaugh, 2009; Huang and Tajkhorshid, 2010; Larsson et al., 2010; Tao et al., 2010; Bastug et al., 2012; Teichman et al., 2012). A highly conserved non-helical Asn310-Met311-Asp312 (NMD) motif interrupts trans-membrane segment (TM) 7 (see below). It lines the back of the substrate- and ion-binding sites and is involved in binding of the ligands (Rosental et al., 2006; Tao et al., 2006; Rosental and Kanner, 2010). The main chain carbonyl oxygen of Asn310 contributes to Na1 site, while the side chain of Met311 protrudes between the substrate, Na1 and Na2 binding sites (Boudker et al., 2007). Symport requires that neither the substrate nor the ions alone are efficiently transported (Crane, 1977). Therefore to traverse the membrane, the transport domains of Glt_{Ph} and EAATs must be loaded with both Na^+ ions and substrate. To complete the transport cycle, the transport domain of Glt_{Ph} must also translocate readily when it is free of both solutes (apo), while in EAATs it requires binding of a K^+ ion. To establish the structural underpinnings of these processes, we determined crystal structures of the outward- and inward-facing states of Glt_{Ph} in apo and ions-only bound forms (Tables 2.1, 2.2 and 2.3). We find that the apo transport domain shows identical structures when facing outward or inward. While ligand-binding sites are distorted, the domain

Table 2.1. X-ray crystallographic data and refinement statistics for Glt_{Ph}-R397A and Glt_{Ph}-K55C-A364C$_{Hg}$ (Glt_{Ph}^{in}) structures deposited at the PDB

	Glt_{Ph}^{in}			
	apo	**Tl^+-bound (apo conf.)**	**alkali-free**	**Tl^+-bound (bound conf.)**
Data collection				
Space group	$C222_1$	$C222_1$	$C222_1$	$C222_1$
Cell dimensions				
a, *b*, *c* (Å)	109.93, 201.81, 207.14	106.98, 196.56, 206.50	106.95, 196.84, 207.48	110.83, 200.43, 206.40
α, β, γ (°)	90.00, 90.00, 90.00	90.00, 90.00, 90.00	90.00, 90.00, 90.0	90.00, 90.00, 90.00
Resolution (Å)	100.0–3.25 (3.31–3.25)	100.0–3.75 (3.81–3.75)	100.0–3.50 (3.56–3.50)	100.0–4.0 (4.14–4.0)
R_{sym} or R_{merge}	10.9 (88.6)	14.0 (94.4)	8.0 (88.1)	16.3 (75.2)
$I/\sigma I$	12.3 (1.2)	8.95 (1.1)	13.5 (1.2)	7.9 (1.3)
Completeness (%)	98.7 (88.1)	99.7 (99.8)	94.4 (92.7)	65.2 (6.5)
Redundancy	5.6 (2.8)	3.8 (3.7)	3.3 (3.2)	3.4 (3.5)
Refinement				
Resolution (Å)	15.0–3.25	15.0–3.75	15.0–3.5	15.0–4.0
No. reflections	34534	21565	25446	11105
R_{work}/R_{free}	22.2/25.8	23.0/25.7	26.3/27.8	25.8/29.6
No. atoms				
Protein	9121	9114	9088	8985
Ligand/ion	3	9	3	9
B-factors				
Protein	108.5	141.8	144.2	137.2
Ligand/ion	135.3	170.8	214.1	102.3
R.m.s. deviations				
Bond lengths (Å)	0.010	0.013	0.005	0.012
Bond angles (°)	1.680	1.861	1.116	1.407
PDB code	4P19	4P1A	4P3J	4P6H

Table 2.1 (Continued)

	Glt_{Ph}-R397A		
	Apo	**Na^+-bound**	**Na^+/aspartate-bound**
Data collection			
Space group	$P2_1$	$P3_1$	$P3_1$
Cell dimensions			
a, *b*, *c* (Å)	112.37, 424.42, 113.99	110.58, 110.58, 306.92	116.96, 116.96, 313.52
α, β, γ (°)	90.00, 119.40, 90.00	90.00, 90.00, 120.00	90.00, 90.00, 120.00
Resolution (Å)	100.0–4.00 (4.14–4.00)	50.0–3.39 (3.51–3.39)	100.0–3.50 (3.63–3.50)
R_{sym} or R_{merge}	7.8 (62.2)	14.0 (>100)	8.4 (>100)
$I/\sigma I$	9.3 (1.3)	13.8 (1.4)	10.6 (0.4)
Completeness (%)	67.9 (13.0)	87.3 (12.0)	98.1 (96.6)
Redundancy	1.8 (2.0)	11.8 (8.6)	4.5 (4.2)
Refinement			
Resolution (Å)	20.0–4.0	12.0–3.41	15.0–3.50
No. reflections	52068	48366	55613
R_{work}/R_{free}	24.9/26.6	28.4/29.3	24.3/26.8
No. atoms			
Protein	35277	17580	18192
Ligand/ion	N/A	6	54/12
Water	N/A	6	6
B-factors			
Protein	139.5	152.0	97.1
Ligand/ion	N/A	145.1	84.7/86.9
Water	N/A	102.6	144.6
R.m.s. deviations			
Bond lengths (Å)	0.010	0.010	0.015
Bond angles (°)	1.393	1.468	1.735
PDB code	4OYE	4OYF	4OYG

Table 2.2. Completeness of datasets corrected for anisotropy

Tl^+-bound Glt_{Ph}^{in} (bound conformation)		Na^+-bound Glt_{Ph}-R397A	
Resolution range (Å)	**Completeness (%)**	**Resolution range (Å)**	**Completeness (%)**
100.0–8.62	99.3	50.00–7.30	99.6
8.62–6.84	99.9	7.30–5.79	100.0
6.84–5.97	100.0	5.79–5.06	100.0
5.97–5.43	99.9	5.06–4.60	100.0
5.43–5.04	99.9	4.60–4.27	100.0
5.04–4.74	69.6	4.27–4.02	100.0
4.74–4.50	39.2	4.02–3.82	100.0
4.50–4.31	23.6	3.82–3.65	98.6
4.31–4.14	14.4	3.65–3.51	63.0
4.14–4.00	6.5	3.51–3.39	12.0

Apo Glt_{Ph}-R397A	
Resolution range (Å)	**Completeness (%)**
100.0–8.62	85.0
8.62–6.84	75.6
6.84–5.97	75.5
5.97–5.43	75.3
5.43–5.04	75.2
5.04–4.74	75.8
4.74–4.50	75.3
4.50–4.31	75.4
4.31–4.14	51.7
4.14–4.00	13.0

Table 2.3. X-ray crystallographic data and refinement statistics for Glt_{Ph}-R397A and Glt_{Ph}-K55C-A364C_{Hg} structures not deposited at the PDB

	Glt_{Ph}-R397A	**Glt_{Ph}^{in}**	
	Tl^+-bound (apo conf.)	**Tl^+/Na^+ (apo conf.)**	**Tl^+/k^+ (apo conf.)**
Data collection			
Space group	$P2_1$	$C222_1$	$C222_1$
Cell dimensions			
a, *b*, *c* (Å)	115.18, 428.53, 116.61	108.11, 198.86, 206.34	106.59, 198.48, 205.82
α, β, γ (°)	90.00, 119.49, 90.00	90.00, 90.00, 90.00	90.00, 90.00, 90.00
Resolution (Å)	30.0–5.0 (5.18–5.00)	100.0–4.0 (4.07–4.00)	100.0–4.15 (4.22–4.15)
R_{sym} or R_{merge}	10.9 (>100)	15.0 (92.2)	13.9 (94.1)
$I/\sigma I$	13.8 (1.9)	8.9 (1.5)	9.2 (1.5)
Completeness (%)	86.4 (75.1)	99.9 (100)	94.5 (90.2)
Redundancy	5.5 (5.8)	3.9 (3.9)	4.0 (3.9)
Refinement			
Resolution (Å)	20.0–5.0	15.0–4.0	15.0–4.15
No. reflections	34747	18184	15419
R_{work}/R_{free}	22.0/26.5	28.2/31.7	28.3/31.2
No. atoms			
Protein	35107	9135	9135
Ligand/ion	N/A	N/A	N/A
Water	N/A	N/A	N/A
B-factors			
Protein	223.00	183.6	194.4
Ligand/ion	N/A	N/A	N/A
Water	N/A	N/A	N/A
R.m.s. deviations			
Bond lengths (Å)	0.008	0.006	0.008
Bond angles (°)	1.186	1.266	1.440

remains compact, suggesting that it relocates across the membrane as a rigid body, similarly to when it is fully bound (Reyes et al., 2009). Ion binding to Na1 site, located deep in the core of the transport domain, triggers structural changes that are propagated to the extracellular gate HP2, at least in part, by the side chain of Met311 in the NMD motif. Consequently HP2, which in the apo form is collapsed into the substrate binding and Na2 sites, frees the sites, assuming conformations more similar to the conformation observed in the fully bound transporter. We suggest that these Na^+-dependent structural changes underlie the high cooperativity of Na^+ and substrate binding, which is thought to be one of the key coupling mechanisms (Reyes et al., 2013). Furthermore, in the structure of Na^+-bound outward-facing Glt_{Ph} we observe opening of HP2 tip, which may facilitate L-asp access to its binding site and prevent the inward movement of the Na^+-only bound transport domain, as previously suggested (Focke et al., 2011). Remarkably, soaks of apo Glt_{Ph} crystals in Tl^+ reveal new cation-binding sites within the apo-like protein architecture. One such site overlaps with the substrate-binding site. Because binding of a cation to this site would compete with binding of Na^+ and the transported substrate, it is well suited to serve as a binding site for a counter-transported ion. We propose that the closed translocation-competent conformation of the transport domain free of Na^+ and substrate is intrinsically stable in Glt_{Ph} but not in EAATs, in which K^+ binding at the newly identified site is required, coupling transport cycle completion to K^+ counter-transport.

2.3 Results

Remodeling of the apo transport domain

To determine the structure of apo Glt_{Ph}, we used R397A mutant that shows a drastically decreased affinity for substrate (Figure 2.2). When fully bound, Glt_{Ph}-R397A crystallizes in the outward-facing state, like wild type Glt_{Ph}, except that L-asp coordination is slightly altered because the mutant is missing the key coordinating side chain of Arg397 (Figure 2.2-2.3; Bendahan et al., 2000; Boudker et al., 2007). These results suggest that R397A is suitable to capture the apo and ions-only bound outward-facing states for their structural characterization. However, removal of Arg397 may affect local electrostatics, potentially altering ion binding; thus, these studies should be interpreted with caution. Apo Glt_{Ph}-R397A also crystallized in an outward-facing conformation that is similar to the structure reported for a close Glt_{Ph} homologue (Jensen et al., 2013). To obtain an apo inward-facing state, we used Glt_{Ph}-K55C-A364C mutant trapped in the inward-facing state upon cross-linking with mercury (Reyes et al., 2009) (Glt_{Ph}^{in}, Figure 2.1). The positions and orientations of the transport domains relative to the trimerization domains remain essentially unchanged in the apo and fully bound forms of Glt_{Ph}-R397A and Glt_{Ph}^{in} (Figure 2.4). In contrast, the conformations of the transport domains themselves differ significantly. Most remarkably, the apo conformations of the transport domain are nearly identical in the outward- and inward-facing states (Figure 2.5-2.7) and are therefore independent of the transport domain orientations and crystal packing environments.

The conformational differences between fully bound and apo forms of the transport domain include a concerted movement of HP2 and TM8a, which form the extracellular surface of the domain, and local rearrangements at the

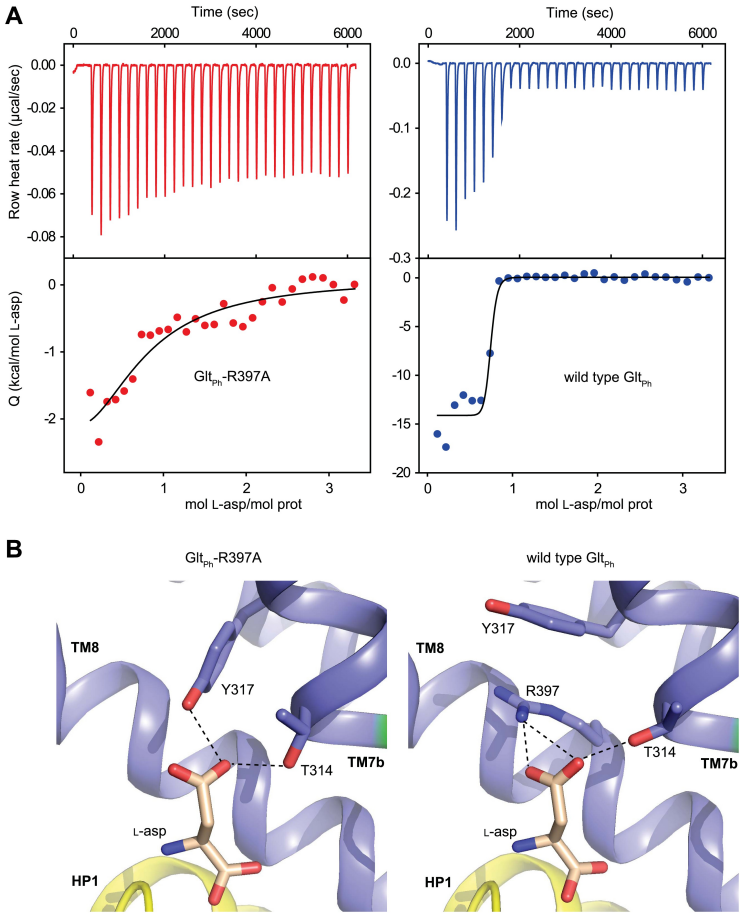

Figure 2.2. Substrate binding to Glt_{Ph}-R397A.
(**A**) Raw binding heat rates measured by isothermal titration calorimetry (top) and binding isotherms (bottom) obtained for Glt_{Ph}-R397A (left) and wild type Glt_{Ph} (right) at 25°C in the presence of 100 mM NaCl. The solid lines through the data are fits to the independent binding sites model with the following parameters for Glt_{Ph}-R397A and wild type Glt_{Ph}, respectively: enthalpy change (ΔH) of −3.2 and −14.3 kcal/mol; the apparent number of binding sites (n) of 0.8 and 0.7 per monomer; dissociation constant (K_d) of 6.6 µM and 27 nM. Note that L-asp binding to the wild type transporter is too tight at 100 mM NaCl to be accurately measured in this experiment. The binding K_d has been estimated to be ~1 nM (Boudker et al., 2007). (**B**) L-asp binding site in Glt_{Ph}-R397A (left) and wild type Glt_{Ph} (right). L-asp and residues coordinating the side chain carboxylate are shown as sticks with carbon atoms colored light brown and blue, respectively. Potential hydrogen bonds (distances less than 3.5 Å) between the L-asp side chain carboxylate and transporter residues are shown as dashed lines. Note that Y317, which forms cation-π interactions with guanidium group of R397 in wild type Glt_{Ph}, interacts directly with L-asp in Glt_{Ph}-R397A.

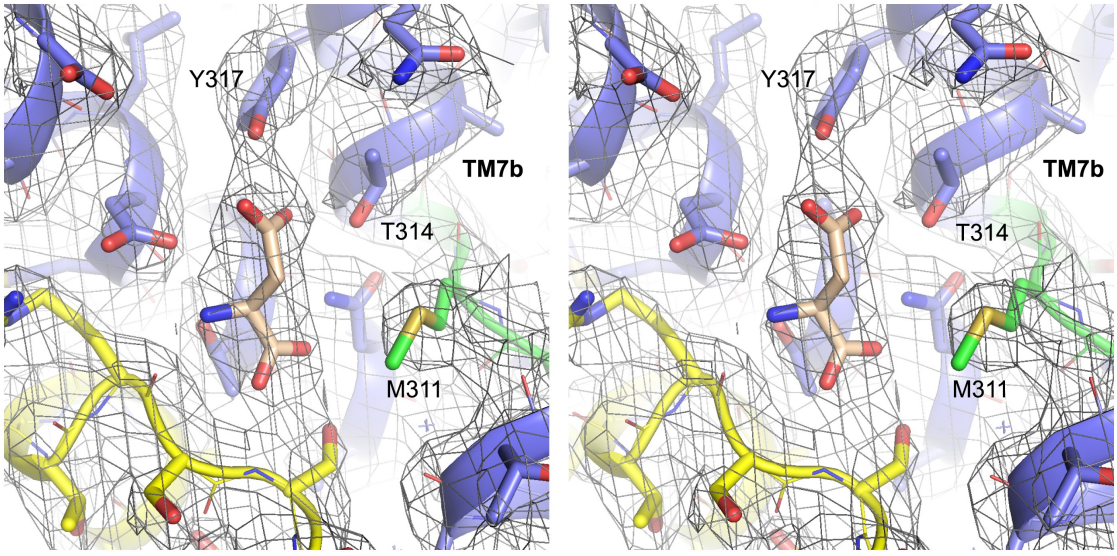

Figure 2.3. Structure of Glt_{Ph}-R397A bound to Na^+ and L-asp.
Stereo view of the averaged $2F_o$-F_c electron density map contoured at 1σ (grey mesh) around residues in L-asp binding site of Glt_{Ph}-R397A.

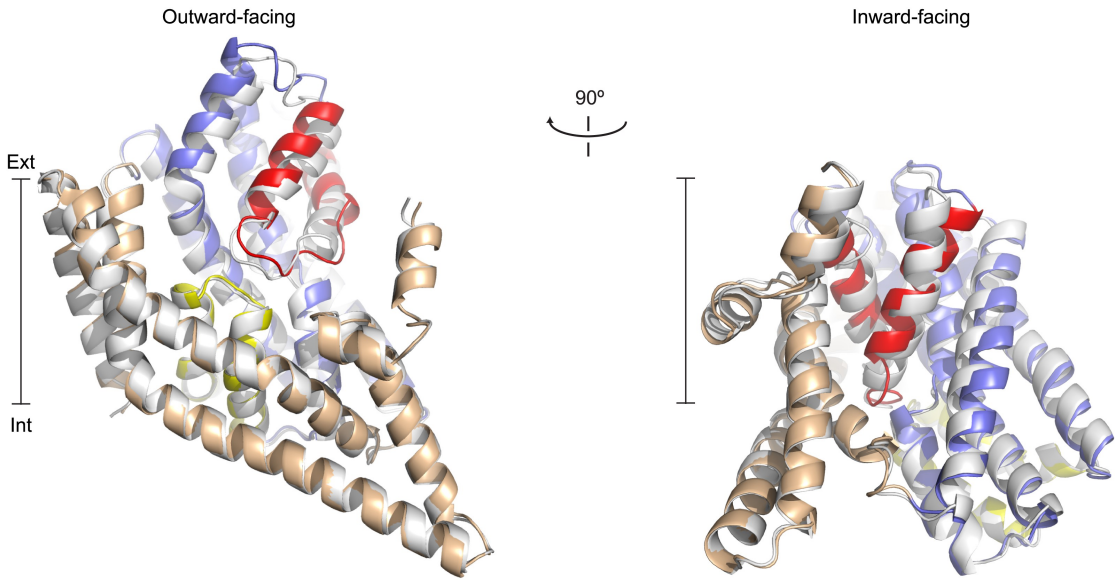

Figure 2.4. Apo protomer structures.
(**A**) Glt_{Ph} protomers in the outward-facing state (left) and a Glt_{Ph}^{in} protomer (right) viewed from within the plane of the membrane. Shown are superimpositions between apo (colors) and fully bound protomers (grey).

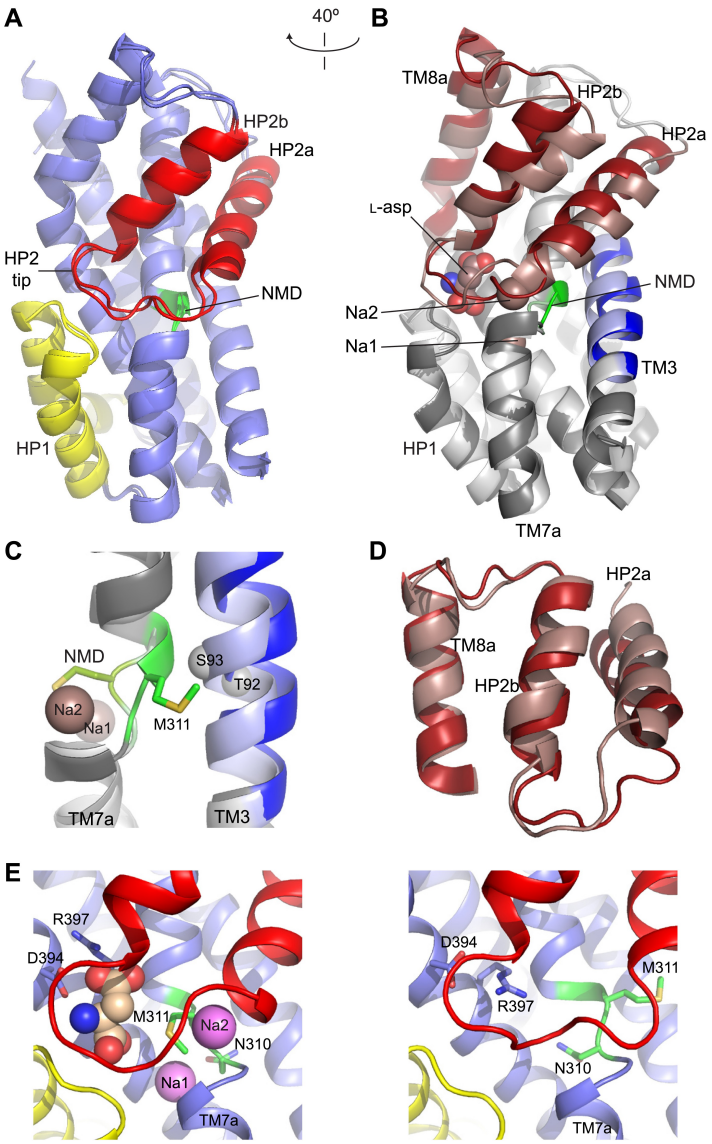

Figure 2.5. Structures of the apo transport domain.
(**A**) Superimposition of the nearly identical apo transport domains in the outward- and inward-facing states. HP1, HP2, and NMD motif are colored yellow, red, and green, respectively. The remainder of the domain is blue. (**B**) Superimposition of the fully bound (light colors, PDB accession number 2NWX) and apo Glt_{Ph}^{in} (dark colors) transport domains. (**C**) The NMD motif and adjacent TM3. Met311 is shown as sticks, and the light blue spheres indicate the Cα positions for T92 and S93. (**D**) The HP2-TM8a structural modules in the fully bound (pink) and apo (red) transport domains superimposed on TM8a and HP2b to emphasize the re-orientation of the HP2a. (**E**) The Na^+ and L-asp binding sites in the fully bound (left) and apo forms (right).

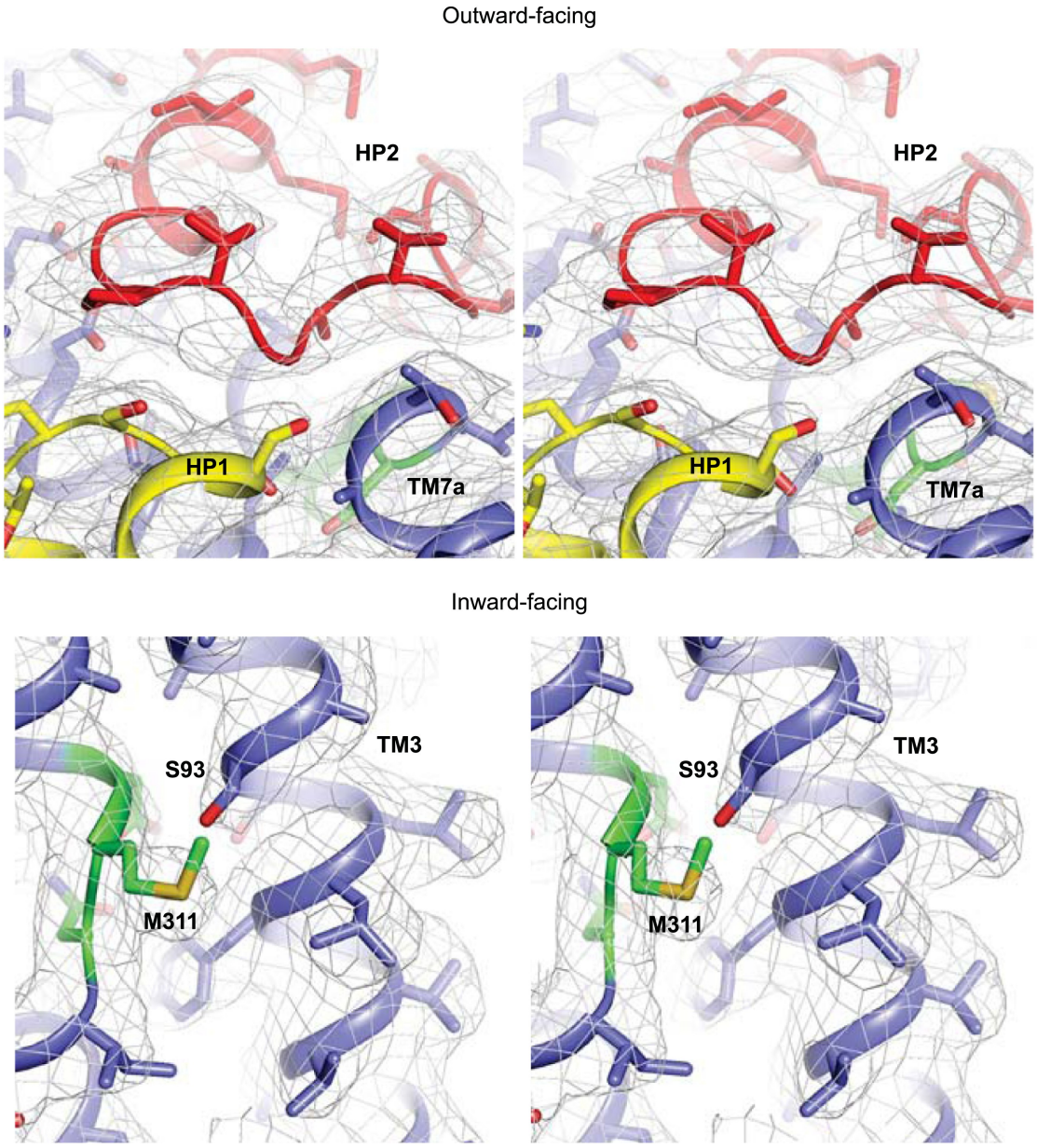

Figure 2.6. Apo protomer structures.
Stereo views of the averaged $2F_o$-F_c electron density maps contoured at 1σ around HP2 tip of the apo Glt_{Ph}-R397A (top) and the NMD motif and TM3 of the apo Glt_{Ph}^{in} (bottom).

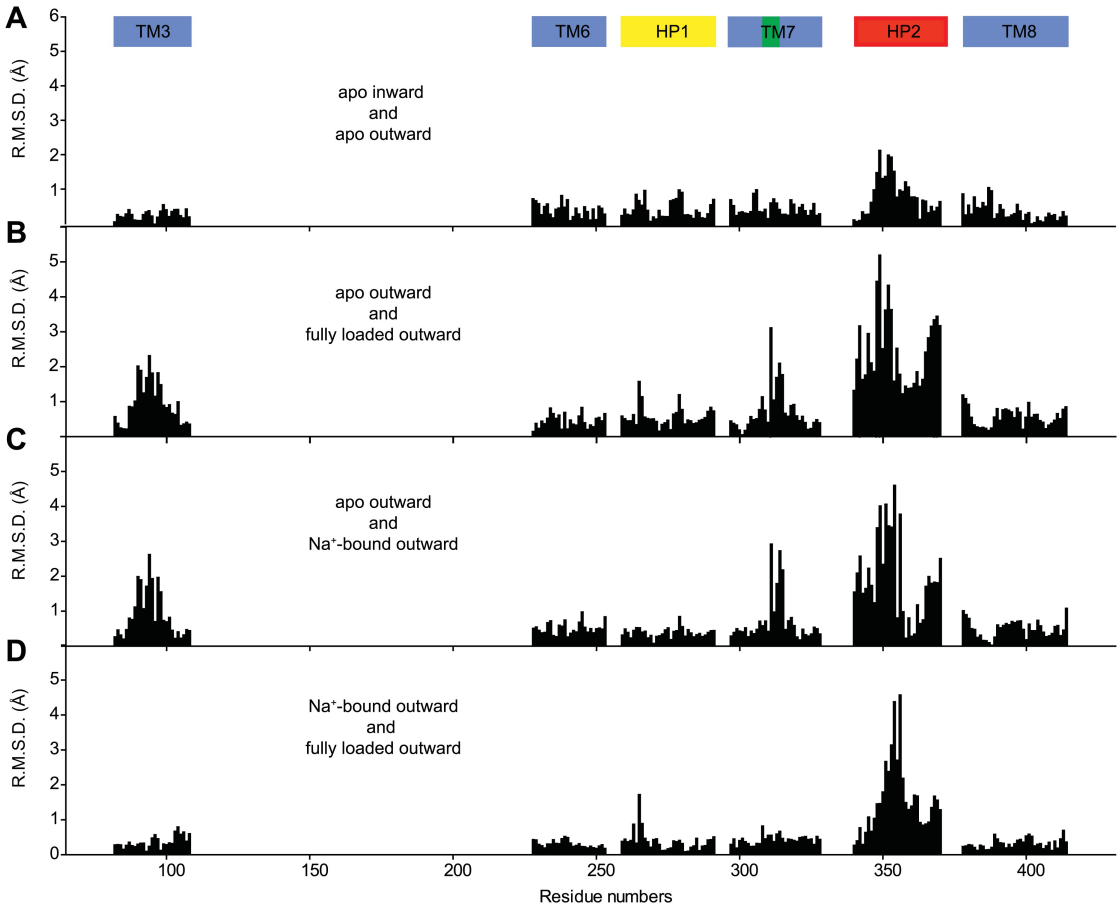

Figure 2.7. Structural comparison of the transport domain in various states.
Plotted are root mean square deviations (R.M.S.D.s) of the main chain atoms calculated per residue using VMD for the transport domains in (**A**) apo outward- and inward-facing states, (**B**) outward-facing apo and fully bound forms, (**C**) outward-facing apo and Na^+-bound forms and (**D**) outward-facing Na^+-bound and fully loaded forms. The loop regions were excluded from the calculations. Notably, there are no significant structural differences between the apo transport domains in the outward- and inward-facing states. Comparison of the apo and fully bound forms of the domain shows differences in TM3, near NMD motif in TM7 and in HP2. Most of these differences are also observed when apo transport domain is compared to Na^+-bound form. In contrast, differences between the Na^+-bound and fully loaded forms are confined mostly to the tip of HP2.

ligand binding sites, involving HP2, the NMD motif and TM3 (Figure 2.5, Figure 2.7-2.8). In HP2, the last helical turn of HP2a unwinds, and HP2a together with the loop region at HP2 tip collapse into the substrate and Na2 binding sites. Within the NMD motif, the side chain of Asn310 rotates away from TM3 and partially fills the empty Na1 site, while the side chain of Met311 undergoes an opposite movement, flipping away from the binding sites (Figure 2.8). Finally, TM3 bends away from the NMD motif, particularly around Thr92 and Ser93 (Figure 2.5). Notably, these residues together with the side chain of Asn310 form one of the proposed third Na^+-binding sites (Huang and Tajkhorshid, 2010; Bastug et al., 2012). Thus, all known ligand-binding sites are distorted in the apo forms (Figure 2.8).

The overall structures of the apo transport domain remain as closed and compacted as in the fully bound forms (Figure 2.9). Therefore, we propose that the unloaded transport domains traverse the membrane as rigid bodies as deduced previously for the fully loaded transport domains (Reyes et al., 2009).

Insight into the coupling mechanism

In Glt_{Ph}, cooperative binding of Na^+ ions and L-asp is central to tightly coupled transport of the solutes (Reyes et al., 2013). Our structures of the apo and fully bound Glt_{Ph} suggest that binding of L-asp and Na^+ at the Na2 site is coupled because the same structural element, the tip of HP2, contributes to both sites and is restructured upon binding. Thus, structural changes in HP2 upon binding of either L-asp or Na^+ ion should greatly favor binding of the other. Met311 in the NMD motif is the only residue that is shared between the Na1 site and the substrate and Na2 sites and also undergoes a conformational change upon ligand binding. To examine whether the structural changes in

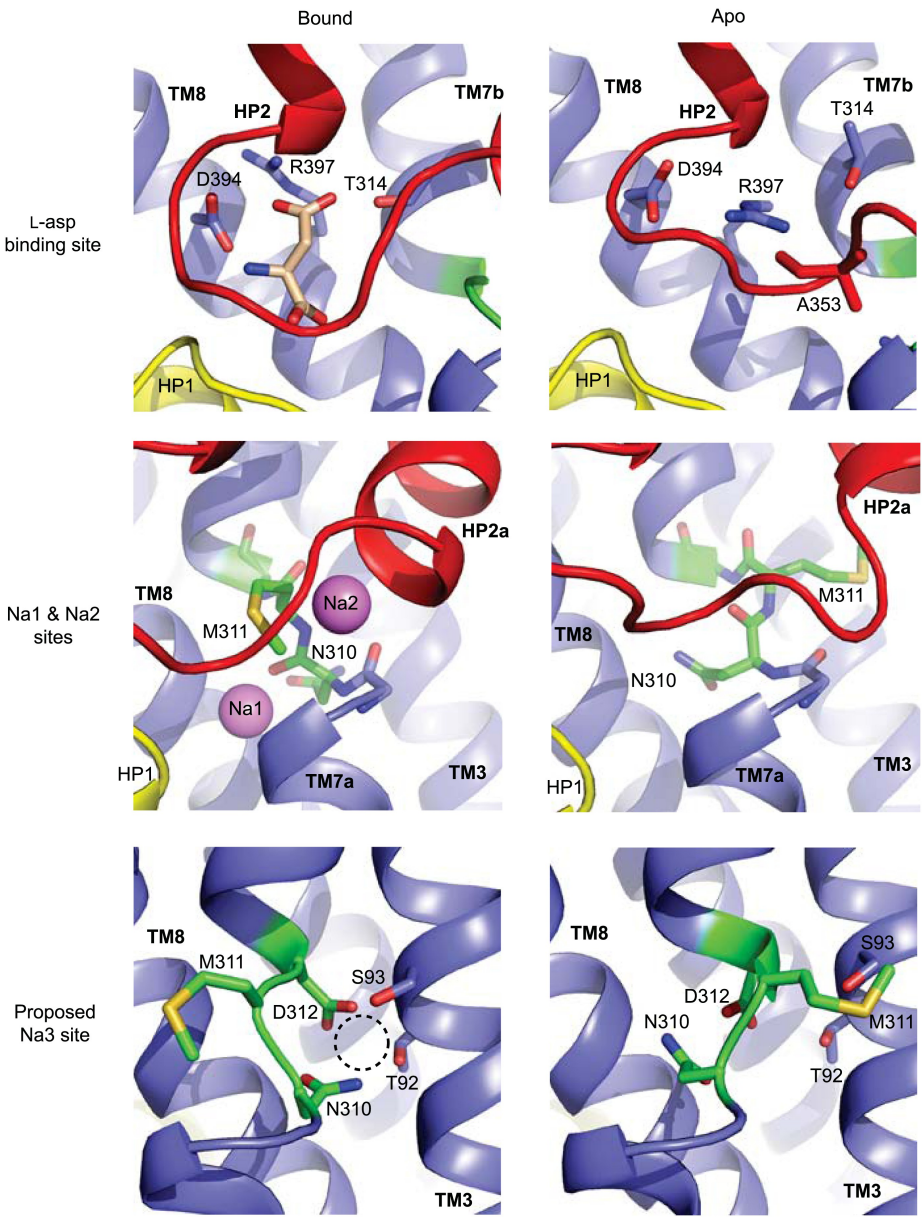

Figure 2.8. Remodeling of L-asp and Na^+ binding sites in the apo conformations.
Close-up views of the fully bound (left) and apo (right) transport domains at L-asp binding site (top), Na1 and Na2 sites (middle), and one of the proposed locations for the third Na^+ binding site (Huang and Tajkhorshid, 2010; Bastug et al., 2012) (dashed circle).

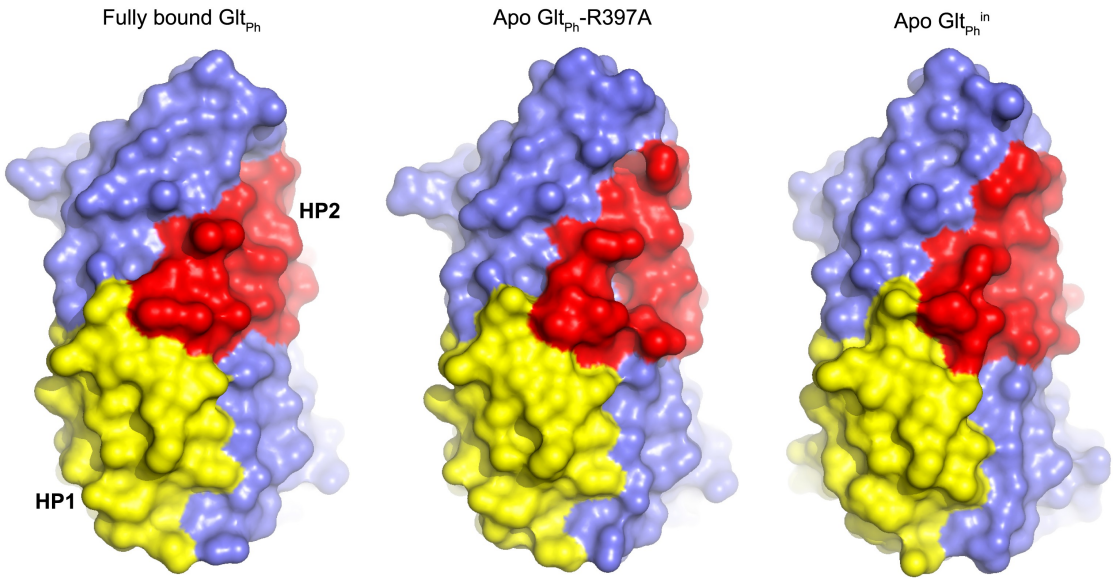

Figure 2.9. Transport domain remains compact.
Surface representation of the transport domain in fully bound and apo forms.

HP2 upon binding of L-asp and Na^+ at the Na2 site could occur independently from those in the NMD motif upon Na^+ binding at the Na1 site, we modeled transport domains with HP2 in the bound conformation and the NMD motif in the apo conformation, or *vice versa* (Figure 2.10). In both models, the side chain of Met311 clashes with residues in HP2, suggesting that the conformational changes in HP2 and the NMD motif must be concerted.

We then mutated bulky Met311 to either another bulky residue, leucine, or to a smaller residue, alanine, which is not expected to experience similar clashes. For these mutants, generated in the context of unconstrained wild type Glt_{Ph} and inward cross-linked Glt_{Ph}^{in}, we measured the dependence of L-asp dissociation constant on Na^+ concentration (Figure 2.10). While this dependence is very steep for the wild type Glt_{Ph} constructs (Reyes et al., 2013) and nearly as steep for the M311L mutants, it is substantially shallower for the M311A mutants. The most parsimonious interpretation of these results is that M311A mutation reduces binding cooperativity between the substrate and Na^+ ions. However, it is also possible, though we think unlikely, that the mutation abrogates ion binding at one or more Na^+-binding sites in the tested concentration range (1–100 mM). Mutating the equivalent methionine to smaller residues in EAAT3 also resulted in less steep dependence of the ionic currents on Na^+ concentration (Rosental and Kanner, 2010). Based on these results, we hypothesize that Met311 is key to the allosteric coupling between the Na1, L-asp and Na2 sites. Consistently, bulky methionine or leucine residues are found at this position in ~85% of glutamate transporter homologues. However, it should be noted that methionine is conserved in the Na^+-coupled Glt_{Ph} and EAATs, while a characterized proton-coupled homologue has leucine at this position (Gaillard et al., 1996). Hence, it is

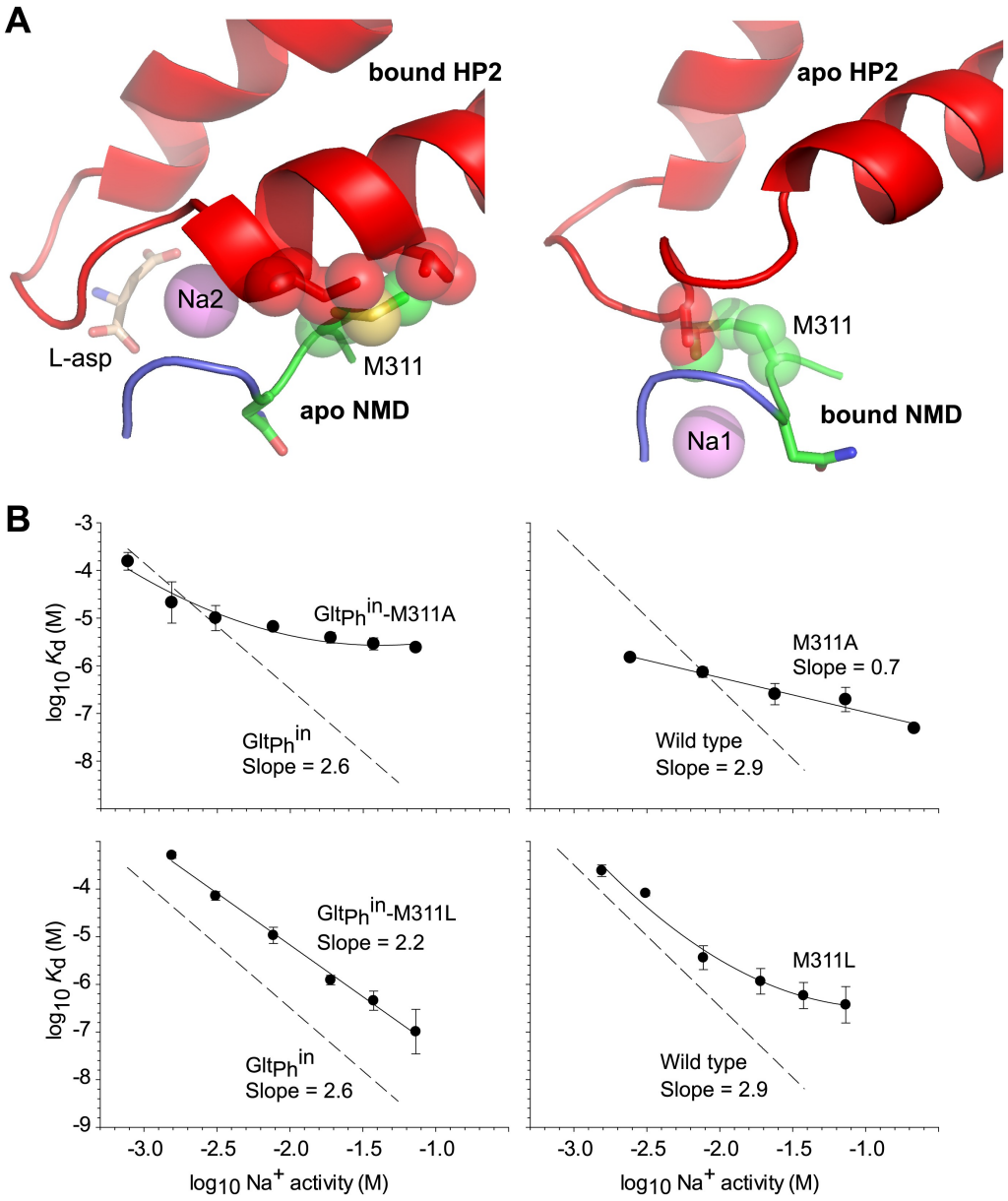

Figure 2.10. Met311 is key to the allosteric coupling.
(**A**) Structural models combining HP2 bound to L-asp and Na^+ at Na2 site with apo conformation of the NMD motif (left), and apo conformation of HP2 with the NMD motif bound to Na^+ at Na1 site (right). Met311 and clashing residues in HP2 are shown as sticks and transparent spheres. (**B**) The dependence of L-asp dissociation constant, K_d, on Na^+ activity plotted on a log–log scale for mutants within the context of $GltPh^{in}$ (left) and unconstrained $GltPh$ (right). The data were fitted to straight lines with slopes shown on the graph or to arbitrary lines for clarity. Dashed lines and corresponding slopes correspond to published dependences for $GltPh^{in}$ and $GltPh$ (Reyes et al., 2013).

possible that the methionine thioether, which is proximal to both Na1 and Na2 sites, plays a direct role in Na^+ binding.

Our hypothesis further predicts that binding of an ion at Na1 site should prime the transporter to accept its substrate. Therefore, we crystallized Glt_{Ph}-R397A in the presence of 400 mM Na^+, but in the absence of L-asp. We also soaked crystals of apo Glt_{Ph}^{in} in Tl^+, an ion with strong anomalous signal that seems to mimic some aspects of Na^+ in $Glt_{Ph}$and EAATs (Boudker et al., 2007; Tao et al., 2008). The obtained outward- and inward-facing structures pictured the transport domains in conformations overall similar to those observed in the fully bound transporter: straightened TM3, Met311 pointing toward the binding sites, extended helix in HP2a and HP2 tip raised out of the substrate binding site (Figure 2.11). Indeed, the structure of Tl^+-bound Glt_{Ph}^{in} is indistinguishable from the fully bound Glt_{Ph}^{in} and both Na1 and Na2 sites are occupied by Tl^+ ions (Figure 2.11). The structure of Na^+-bound Glt_{Ph}-R397A differs significantly from the fully bound Glt_{Ph}-R397A only at the tip of HP2 (Figure 2.7, also see below). The coordinating residues at the Na1 site are correctly positioned and the site is likely occupied by a Na^+ ion. The Na2 site still shows a distorted geometry: the last helical turn of HP2a points away from the site due to the altered conformation of the tip of HP2 (Figure 2.11). Collectively, our results demonstrate that binding of the coupled ions, notably at the Na1 site, is sufficient to trigger isomerization of the transport domain from the apo conformation to the bound-like conformation. The energetic penalty associated with this isomerization likely explains why Na^+ ions alone bind weakly to the transporter (Reyes et al., 2013). This experimental observation contrasts with highly favorable calculated binding energies (approximately −10 kcal/mol for Na1) that were obtained using fully bound protein conformation and where the

Figure 2.11. Structures of ions-only bound transport domain.
(**A**) Superimposition of the fully bound transport domains (grey) and Tl^+-bound Glt_{Ph}^{in} transport domain in the bound-like conformation (colors), with the averaged anomalous difference Fourier map contoured at 8σ (cyan mesh). (**B**) Superimposition of the fully bound (grey) and Na^+-only bound Glt_{Ph}-R397A (colors) transport domains. (**C**) Na^+ and L-asp binding sites with fully-bound structure shown in white and Na^+-bound structure in colors. Hinge glycine residues are shown as spheres. The modeled Na^+ ion in Na1 site is pink. (**D**) Superimposition of the HP2-TM8 in the fully bound transport domain (grey) and in Glt_{Ph}-R397A bound to Na^+ only (colors), showing similar conformations of HP2a. (**E**) WebLogo representation of the consensus sequence and relative abundance of residues in HP2 tip. (**F**) Surface representation of the transport domain of Glt_{Ph}-R397A bound to Na^+ only showing access to the substrate-binding site. L-asp was placed into the binding site for reference.

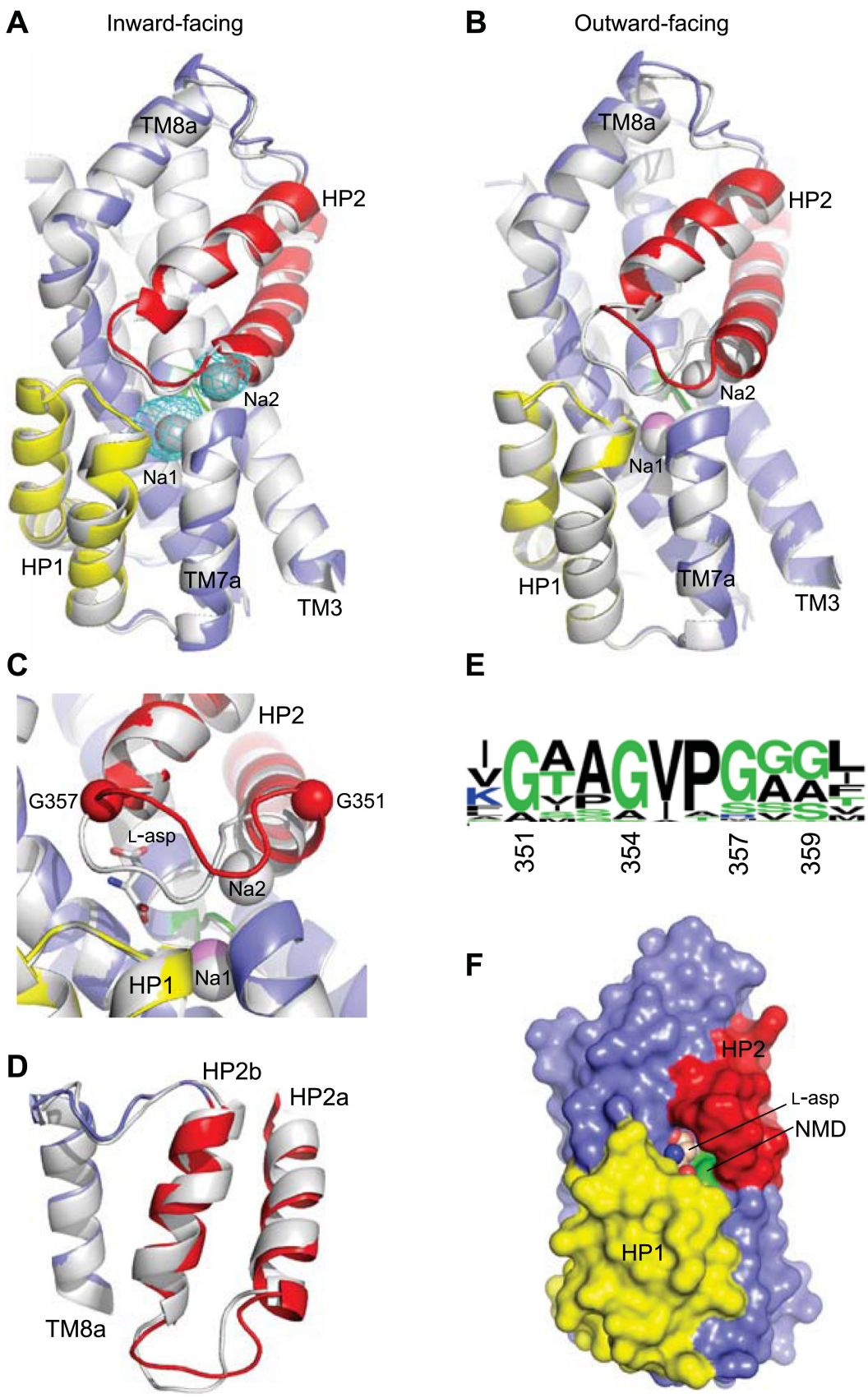
A
Inward-facing
TM8a
HP2
Na2
Na1
HP1
TM7a
TM3
B
Outward-facing
TM8a
HP2
Na2
Na1
HP1
TM7a
TM3
C
HP2
G357
G351
L-asp
Na2
HP1
Na1
D
HP2b
HP2a
TM8a
E
351
354
357
359
F
HP2
L-asp
NMD
HP1

reference ion-free state is the same as the bound state (Larsson et al., 2010; Bastug et al., 2012; Heinzelmann et al., 2013).

Na^+-mediated gating in the outward-facing state

The structure of the Na^+-only bound Glt_{Ph}-R397A shows HP2 in a conformation overall similar to that observed in the fully bound transporter, but with an opened tip (Figure 2.11-2.12). This opening is smaller than the opening observed previously in the structure of Glt_{Ph} in complex with the blocker L-threo-β-benzyloxyaspartate (Figure 2.13; Boudker et al., 2007), and it is hinged at two well-conserved glycine residues at positions 351 and 357 (Figure 2.11). Interestingly, among the nine amino acids forming the tip in Glt_{Ph} (residues 351 to 359), five are glycines in the consensus sequence generated for the glutamate transporter family, although not all are present in each homologue (Figure 2.11, 2.14). We suggest that the glycines support the structural flexibility of the HP2 tip in all members of the family, but that the structural specifics of the tip opening may vary among homologues.

To test whether the trans-membrane movement of the transport domain is possible when the tip of HP2 is opened, we modeled the open tip conformation in the context of the previously reported early transition intermediate structure (Figure 2.15; Verdon and Boudker, 2012). In this structure, the transport domain tilts towards the trimerization domain but does not yet undergo a significant translation toward the cytoplasm. We find that such intermediate state with the opened tip of HP2 can be achieved without major steric clashes, while further progression of the transport domain to the inward-facing position could be impeded because the tip is likely to clash with TM5 in the trimerization domain (Figure 2.15). Also in the inward-facing state

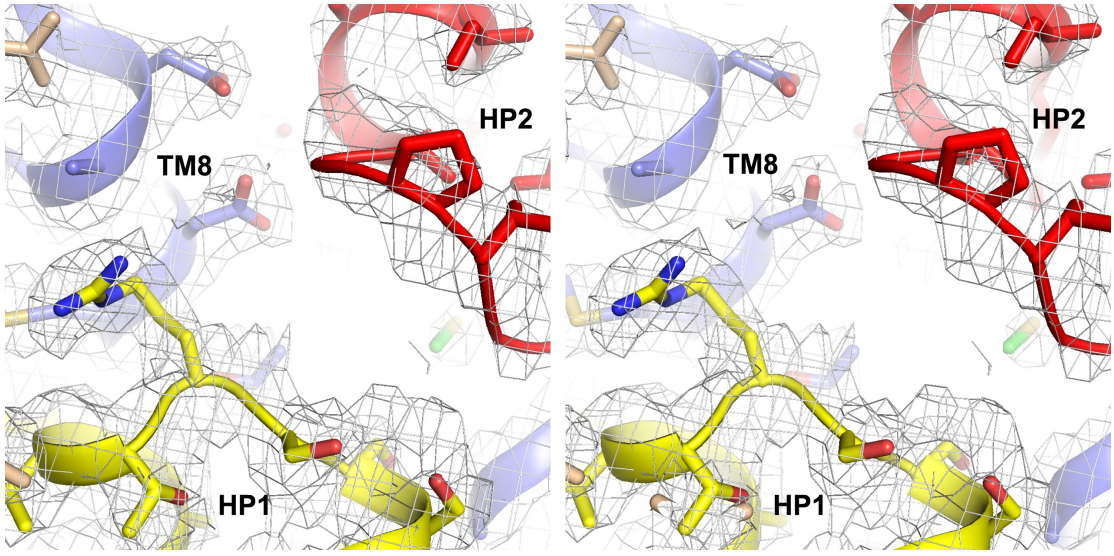

Figure 2.12. Na^+ only bound Glt_{Ph}-R397A.
Stereo view of the averaged $2F_o$-F_c electron density map contoured at 1σ around HP1 and HP2.

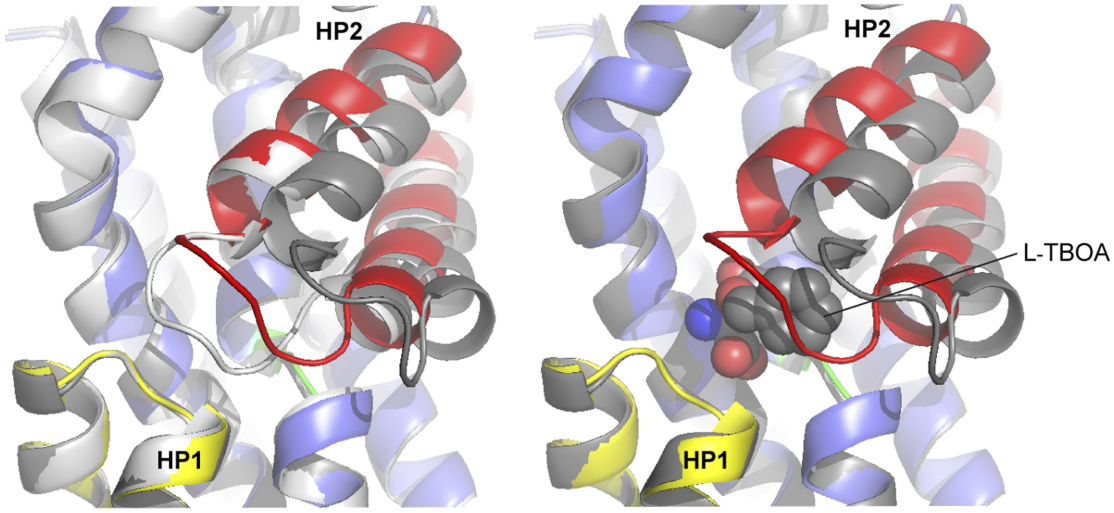

Figure 2.13. Superimposition of the transport domains bound to Na^+ and L-asp (light grey), Na^+ and L-TBOA (dark grey) and Na^+ only (colors). Ligands are omitted for clarity, except that L-TBOA is shown as spheres in the right panel. Notably, the observed additional opening of HP2 is necessary to accommodate L-TBOA.

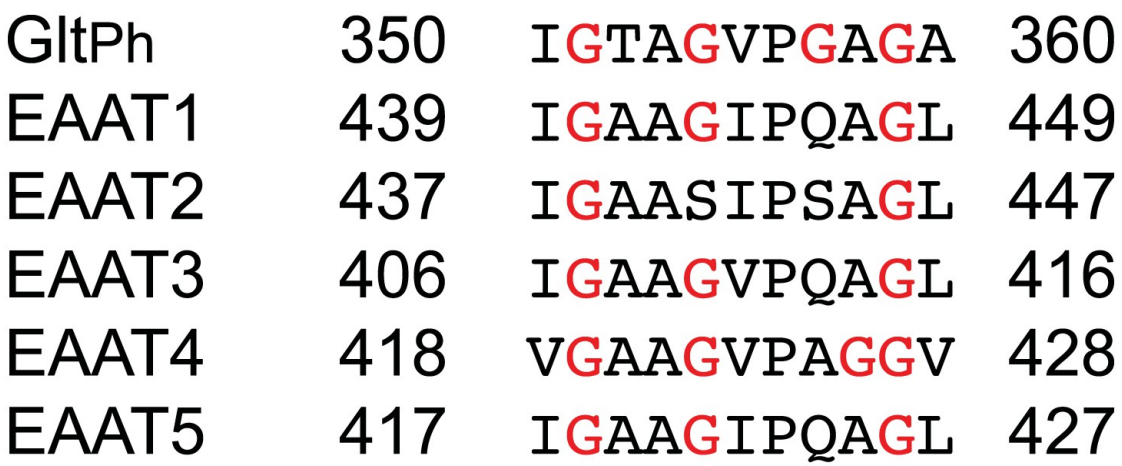

Figure 2.14. Sequence alignment for the HP2 tip region of Glt_{Ph} and human EAAT sub-types 1–5.

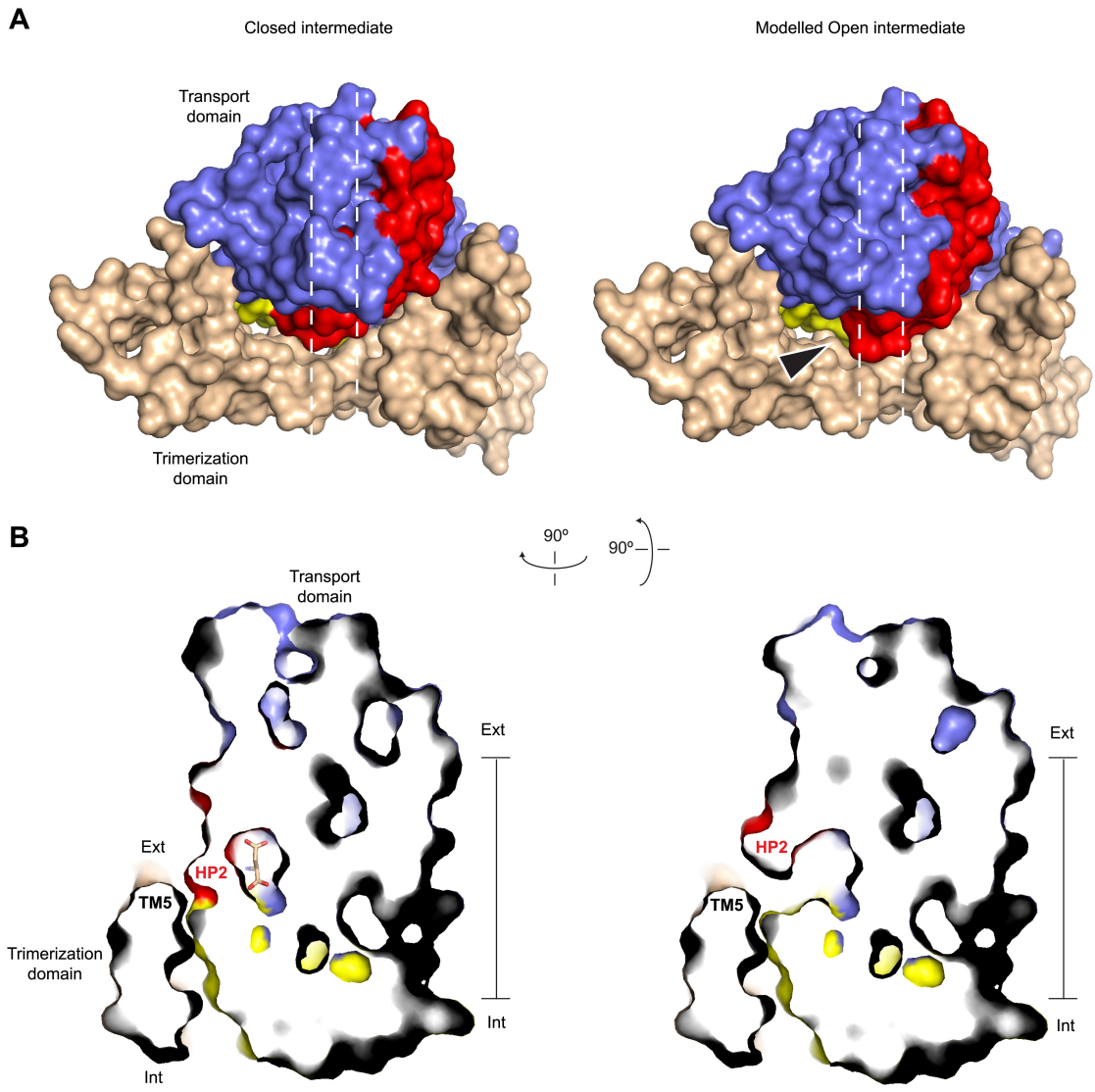

Figure 2.15. Modeled Na^+-bound early transition intermediate between the outward- and inward-facing states.
(**A**) Surface representations of the protomer in the fully bound intermediate state (PDB code 3V8G) (left), and the modeled Na^+-bound intermediate with an open HP2 tip (right) viewed from the extracellular space (top). The model reveals no clashes, suggesting that the observed opening of HP2 is structurally compatible with the intermediate orientation of the transport domain. The arrows indicate the point of access to the domain interface with potentially increased solvent accessibility. (**B**) Side views of thin cross-sections of the closed fully bound (left) and open Na^+-only bound (right) intermediate state. The protomers are sliced normal to the membrane plane, as indicated by the dashed lines in **A**.

HP2 is packed against the trimerization domain and cannot open in a manner observed in the outward-facing state. Consistently, HP2 is closed in Glt_{Ph}^{in} bound to Tl^+ (Figure 2.11).

Therefore, opening of the HP2 tip upon Na^+ binding in the outward-facing state may serve as a structural mechanism preventing uncoupled uptake of Na^+ ions. We suggest that the structural changes in the NMD motif and HP2 that are triggered upon Na^+ binding at the Na1 site may lead to the loss of direct interactions between the tip of HP2 and the rest of the transport domain, resulting in tip opening. Subsequent binding of L-asp and Na^+ at the Na2 site is then required to provide compensatory interactions, allowing HP2 tip to close. Similar conformational behavior has been observed for transporters with the LeuT fold: when bound to Na^+ ions only, substrate binding sites are open to the extracellular solution, and substrate binding is required for occlusion (Weyand et al., 2008; Krishnamurthy and Gouaux, 2012).

We do not see a transition into an open conformation in the inward-facing Glt_{Ph}^{in} bound to Tl^+ ions (Figure 2.11). This may be because Tl^+ ions do not faithfully mimic Na^+ ions and fail to induce an open state or it may be because Na^+ bound inward-facing state is, indeed, closed. This latter possibility does not contradict the requirements of symport because the measured dissociation constant for Na^+ ions in the inward-facing state (250 mM) (Reyes et al., 2013), is far above Na^+ concentration in the cytoplasm (10 mM) and therefore, Na^+-bound inward-facing state is not expected to be significantly populated.

We and others have proposed that transition intermediates mediate fluxes of polar solutes, including anions, because potentially hydrated cavities

form in such intermediates at the interface between the trimerization and transport domains (Stolzenberg et al., 2012; Verdon and Boudker, 2012; Li et al., 2013). Interestingly, because the tip of HP2 forms part of this interface in the fully bound intermediate state of the transporter, opening of the tip in the Na^+-only bound form may increase solvent accessibility to the interface (Figure 2.15).

New cation-binding sites

While soaking apo Glt_{Ph}^{in} crystals in Tl^+ solutions, we observed that only in approximately one third of crystals Tl^+ ions bound to the Na1 and Na2 sites, inducing transition from apo- to bound-like conformation as described above. In the majority of the crystals, we observed no conformational changes of the transport domain and Tl^+ ions incorporated at two previously uncharacterized sites (Figure 2.16), within the small cavities that remain under the collapsed HP2 (Figure 2.17). One site, termed Na2', involves residues of HP2 and TM7a that form the Na2 site, but in a different ion coordinating geometry due to the conformational difference in HP2 (Figure 2.16). The second site, termed Ct, overlaps with the L-asp binding site and is formed by the side chains of highly conserved Asp394 and Thr398 in TM8 and main chain carbonyl oxygen atoms of HP1 and HP2 (Figure 2.16). Tl^+ soaks of the outward-facing apo Glt_{Ph}-R397A also showed no conformational changes of the transport domain, with Tl^+ binding at the Ct site, but not at the Na2' site (Figure 2.16). The ion selectivity of the Ct site remains ambiguous, because neither 300 mM K^+ nor 10 mM Na^+ efficiently inhibited incorporation of Tl^+ (150 mM) at this site in Glt_{Ph}^{in} (Figure 2.18). Crystals deteriorated at higher Na^+ concentrations. In

Figure 2.16. New cation binding sites.
(**A**) Superimpositions of Glt_{Ph}^{in} (left) and outward-facing Glt_{Ph}-R397A (right) transport domains in the apo form (grey) with Tl^+-bound apo-like conformations (colors). Averaged anomalous difference Fourier maps are contoured at 8σ (cyan mesh). (**B**) Modeled Tl^+ ions bound to the Ct and Na2' sites (left), and L-asp aspartate and Na^+ ions bound to the Na1 and Na2 sites in the fully bound transport domain (right). (**C**) Close-up view of Tl^+ in the Ct site of apo-like Glt_{Ph}^{in} and L-asp in the fully bound transporter.

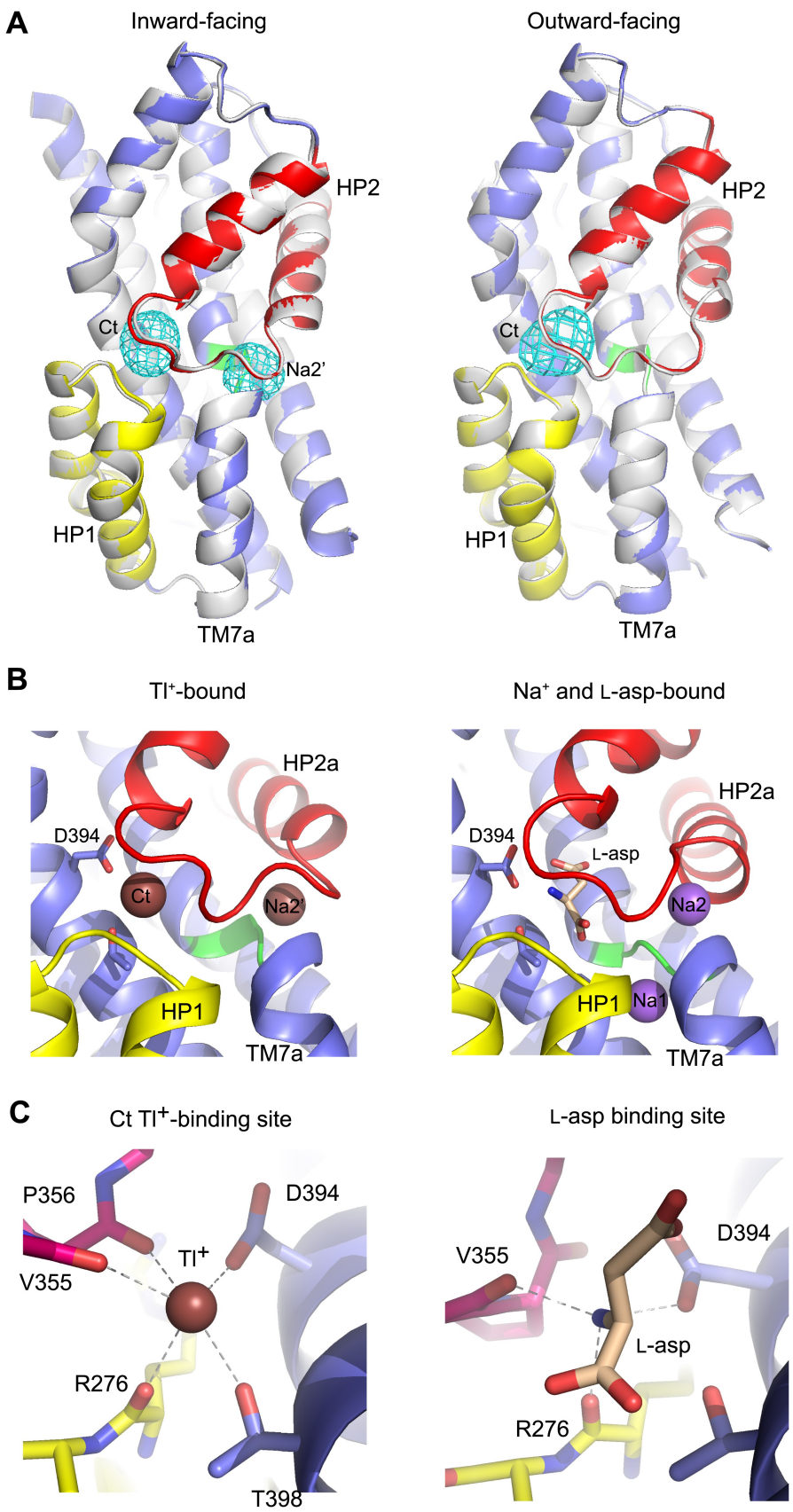
A
Inward-facing
Outward-facing
HP2
Ct
Na2'
HP1
TM7a
HP2
Ct
HP1
TM7a
B
Tl+-bound
Na+ and L-asp-bound
HP2a
D394
Ct
Na2'
HP1
TM7a
HP2a
D394
L-asp
Na2
HP1
Na1
TM7a
C
Ct Tl+-binding site
L-asp binding site
P356
D394
Tl+
V355
R276
T398
V355
D394
L-asp
R276

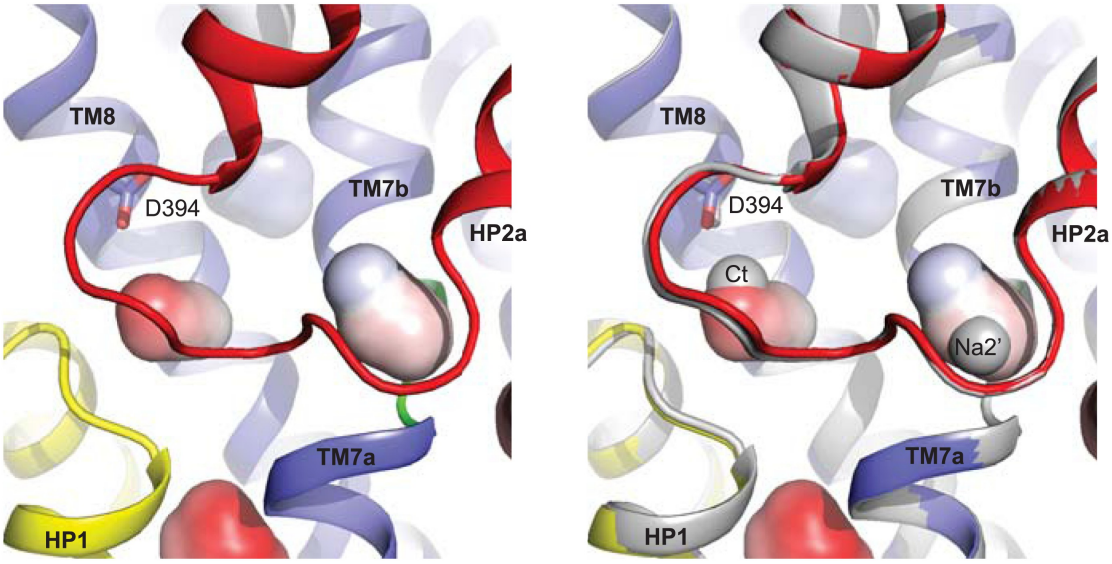

Figure 2.17. Transport domain internal cavities.
Internal cavities in the apo Glt_{Ph}^{in} structure (left). Cavities were calculated using solvent radius of 1.4 Å and colored by local electrostatic potential with red and blue being negative and positive, respectively. The same structure superimposed with the Tl^{+}-bound apo-like Glt_{Ph}^{in} (right). The Tl^{+}-bound structure is shown in grey and Tl^{+} ions at the Ct and Na2' sites are shown as spheres.

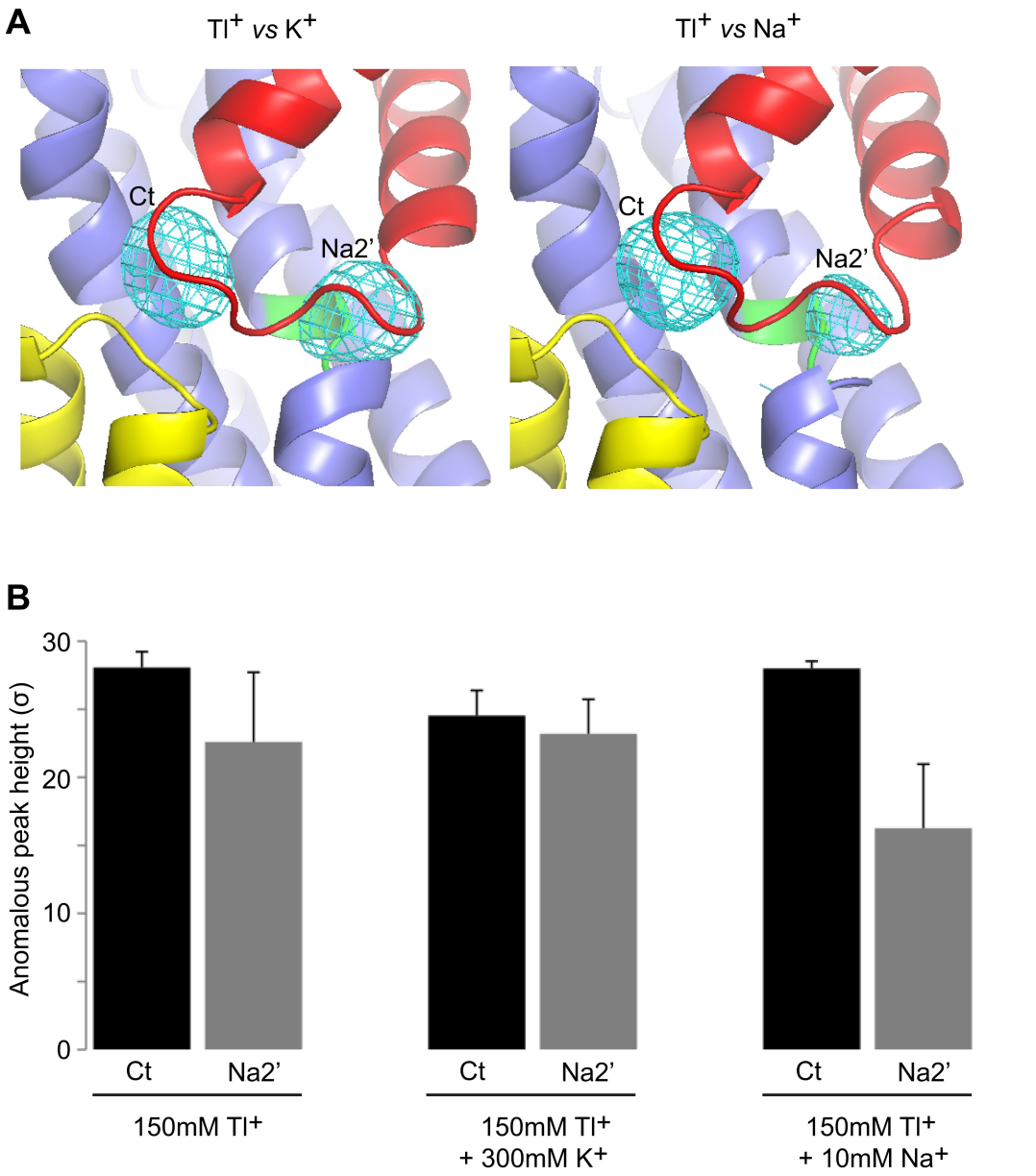

Figure 2.18. Specificity of the new cation binding sites in apo-like Glt_{Ph}^{in}. (**A**) Averaged anomalous difference Fourier maps contoured at 8σ (cyan mesh) for Tl^+-soaked (150 mM) Glt_{Ph}^{in} in the presence of 300 mM K^+ (left) and 10 mM Na^+ (right) showing a decrease of the Tl^+ signal at Na2' site in the presence of Na^+. (**B**) Means of the anomalous difference Fourier peak heights in the three protomers and their associated standard deviations at the Ct and Na2' sites in Glt_{Ph}^{in} crystals. Soaking conditions are listed below the graphs.

contrast, the Na2' site seems to show a preference for Na^+, which even at low concentration (10 mM) interfered significantly with Tl^+ binding.

The functional relevance of these sites is speculative at present. However, it is remarkable that the Ct site is positioned exactly at the same place as the amino group of the bound L-asp and share several coordinating moieties. Therefore, binding of a cation at the Ct site and binding of the substrate are mutually exclusive. Because the Ct site is observed only in the apo-like conformation, cation binding at this site would also inhibit the transition into the bound-like conformation upon Na^+ binding at the Na1 site. Finally, the Ct site is observed in both the inward- and outward-facing states, suggesting that the apo-like transport domain could carry the ion across the membrane. These are the exact properties expected for the K^+-binding site in EAATs. Moreover, it has been previously proposed that K^+ binds to EAATs at a similar position (Holley and Kavanaugh, 2009). Most remarkably, in an insect K^+-independent dicarboxylate transporter, an asparagine to aspartate mutation at the position equivalent to Asp394 in Glt_{Ph} changes the transporter substrate specificity to amino acid glutamate, and also leads to dependence on K^+ counter-transport (Wang et al., 2013). Therefore this aspartate plays a key role in both binding the amino group of substrate and coupling to K^+ counter-transport. Consistently, Asp394 in Glt_{Ph} coordinates both the amino group of the bound substrate and Tl^+ in the Ct site. Notably, while Tl^+ mimics, to some extent, Na^+ ions in Glt_{Ph} and EAATs, it is a better mimic of K^+ ions in EAATs (Boudker et al., 2007; Tao et al., 2008).

Movement of HP1 in the inward-facing state

To examine whether a complete removal of Na^+ and K^+ ions had an effect on the structure of Glt_{Ph}^{in}, we soaked apo Glt_{Ph}^{in} crystals (typically grown in the presence of K^+) in alkali-free buffer. Interestingly, we observed a small, but reproducible structural change in several crystals examined: HP1 and TM7a that form the transport domain cytoplasmic surface moved slightly towards TM8, with the tip of HP1 detaching from that of HP2 (Figure 2.19-2.20). This movement is observed clearly in one protomer (chain B in 4P3J), in which these helices are not involved in crystal packing contacts. It is reminiscent of the isomerization of the structurally symmetric HP2 and TM8a on the extracellular side of the domain observed upon the transition from bound to apo forms (Figure 2.19). It was suggested previously that HP1 participates in intracellular gating in Glt_{Ph} (Reyes et al., 2009; DeChancie et al., 2010). Indeed, the observed movement of HP1 generates a small opening, leading to the substrate and Ct sites (Figure 2.21), and it is reminiscent of the movement observed in molecular dynamics simulations (DeChancie et al., 2010; Zomot and Bahar, 2013). However, this conformational difference is too small to be interpreted unambiguously.

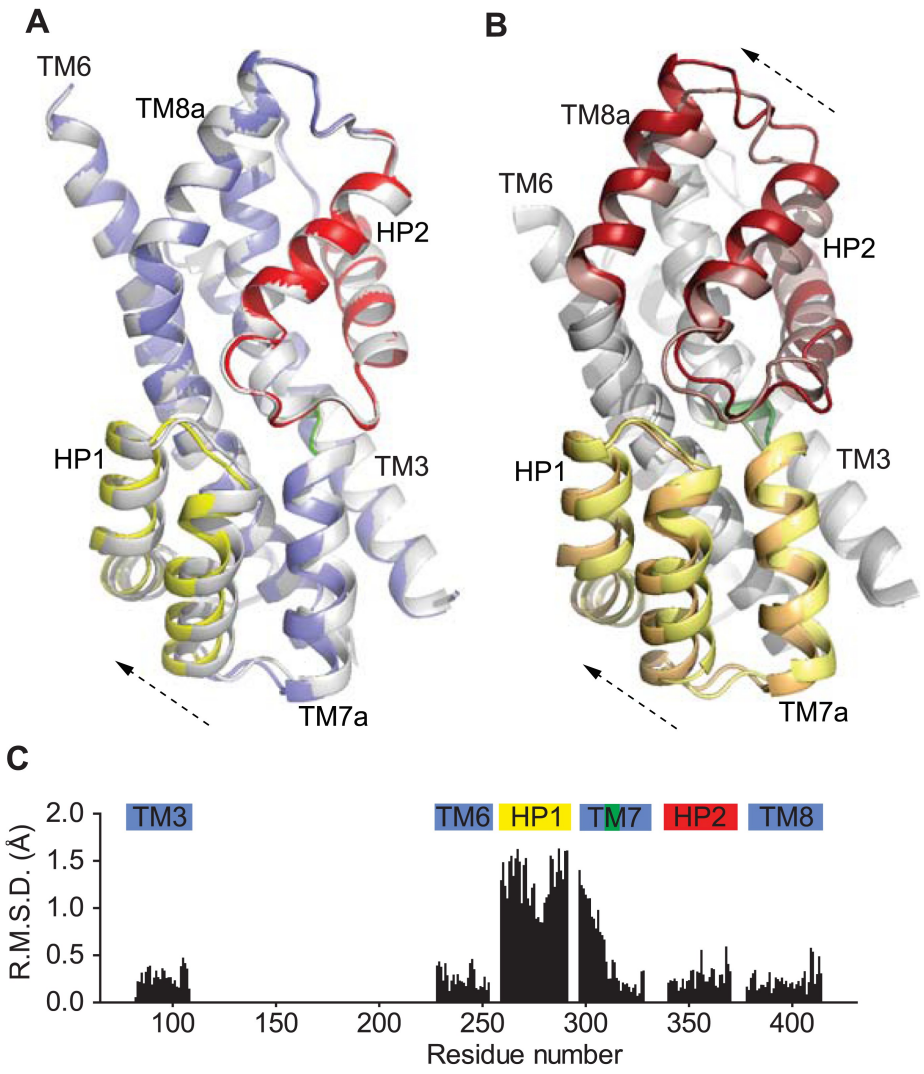

Figure 2.19. Movements of the HP1-TM7a structural module.
(**A**) Superimposition of Glt_{Ph}^{in} transport domains when bound to Tl^{+} in the apo-like conformation (grey) and when prepared in an alkali-free solution (colors). (**B**) The transport domains of the fully bound Glt_{Ph} (light colors) and alkali-free Glt_{Ph}^{in} (dark colors) superimposed on TM6. Arrows indicate movements of the structurally symmetric HP1-TM7a and HP2-TM8a modules. (**C**) Per residue main chain R. M. S. D. values calculated for the structures of the inward-facing transport domains bound to Tl^{+} in apo-like conformation and alkali-free shown in **A** and superimposed on HP2. The bars above the plot represent secondary structure elements colored as in **A**.

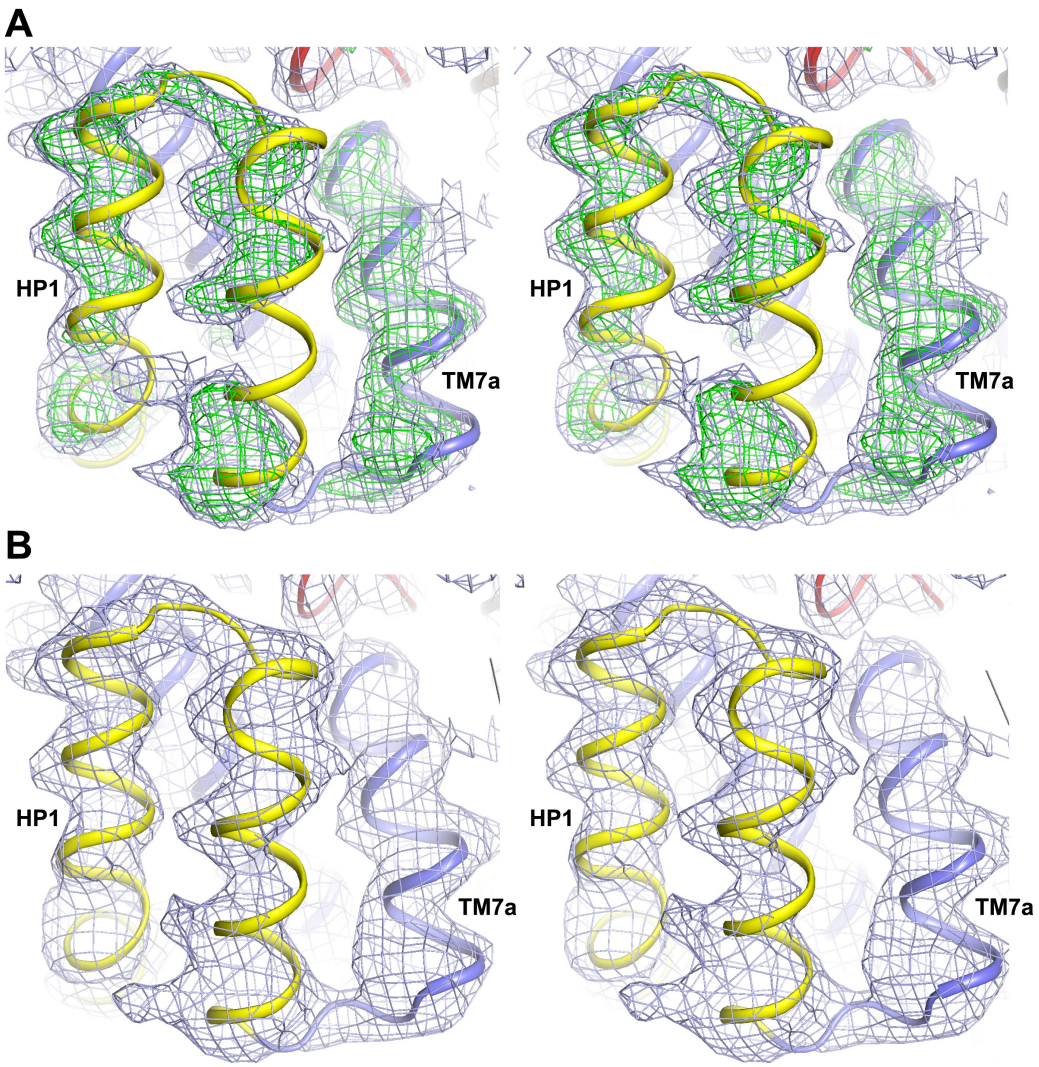

Figure 2.20. Alkali-free inward-facing Glt_{Ph}^{in}.
(**A**) Stereo view of the $2F_o$-F_c (1σ) and F_o-F_c (3σ) omit maps obtained after molecular replacement using Tl^+-bound Glt_{Ph}^{in} and refinement of a model with HP1 and TM7a omitted, in the protomer showing the detachment of HP1. The model shown is that of Tl^+-bound Glt_{Ph}^{in}. It is clear that HP1 and TM7a do not fit well into the electron density. (**B**) Stereo view of the $2F_o$-F_c (1σ) map around HP1 and TM7a obtained after refinement of a complete model. The model was generated by moving HP1 and TM7a as a rigid-body to fit into the electron density, with no further manual rebuilding.

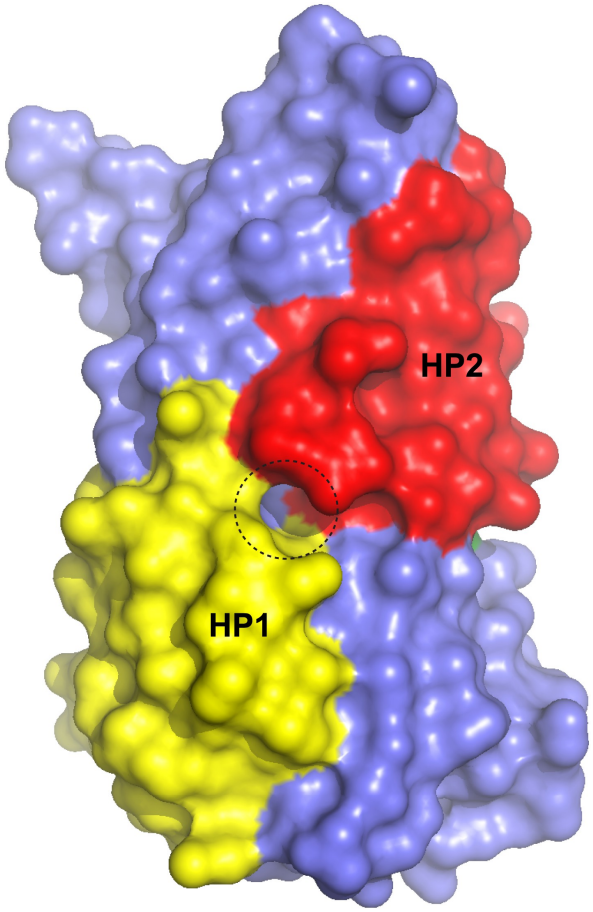

Figure 2.21. Surface representation of the alkali-free inward-facing Glt_{Ph}^{in} transport domain in this protomer after refinement.
A dashed circle indicates a small opening between HP1 and HP2.

2.4 Discussion

Our apo and ions-only bound structures reveal a remarkable structural plasticity of Glt_{Ph} transport domain that is likely a conserved feature in the glutamate transporter family. In addition to the large trans-membrane rigid-body movements of the transport domain between outward- and inward-facing orientations, local conformational changes within the domain accompany binding and release of the transported substrate and ions (Figure 2.22). These local changes provide a structural explanation of how Na^+ gradients are harnessed to drive concentrative substrate uptake, supporting two previously proposed coupling mechanisms (Focke et al., 2011; Reyes et al., 2013): allosterically coupled binding of the substrate and symported Na^+ ions, and opening of HP2 upon Na^+ binding, which impedes the inward trans-membrane movement of the Na^+-only bound transport domain.

The apo transport domains in the outward- and inward-facing states are essentially identical and as compact as when they are fully bound, consistent with previous spectroscopic experiments (Focke et al., 2011). Therefore, the apo transport domain is likely able to transition readily between the cytoplasmic and extracellular orientations. Consistently, previous spectroscopic studies showed that the transport domains continuously sample the outward- and inward-facing positions with nearly equal probabilities either when bound to Na^+ and L-asp or when free of the solutes (Akyuz et al., 2013; Erkens et al., 2013; Georgieva et al., 2013; Hanelt et al., 2013). Moreover, these transitions are more frequent in the apo transporter, consistent with a lack of large energetic barriers (Akyuz et al., 2013). In Glt_{Ph}, the compact translocation-competent apo conformation of the transport domain is stabilized by interactions between the collapsed HP2, and HP1,

TM7, and TM8. In EAATs, by contrast, we speculate that these interactions are insufficient and that K^+ binding to the Ct site is required to stabilize the translocation-competent closed conformation that can return to the outside, ensuring coupling between substrate uptake and counter-transport of K^+ ion. Local structural differences in EAATs in the vicinity of the Ct site may underlie the higher affinity and specificity of this site for K^+ ion.

In conclusion, we have shown structurally that ion binding and unbinding events in Glt_{Ph} and, by analogy, in EAATs control the conformational state of the transporter, determining its competence to bind substrate and undergo transitions between the outward- and inward-facing states. Studies establishing the location of the Na3 binding site; the potential role of the Ct site in binding K^+; and the gating mechanism in the inward-facing state will be necessary to verify and refine our proposed mechanisms.

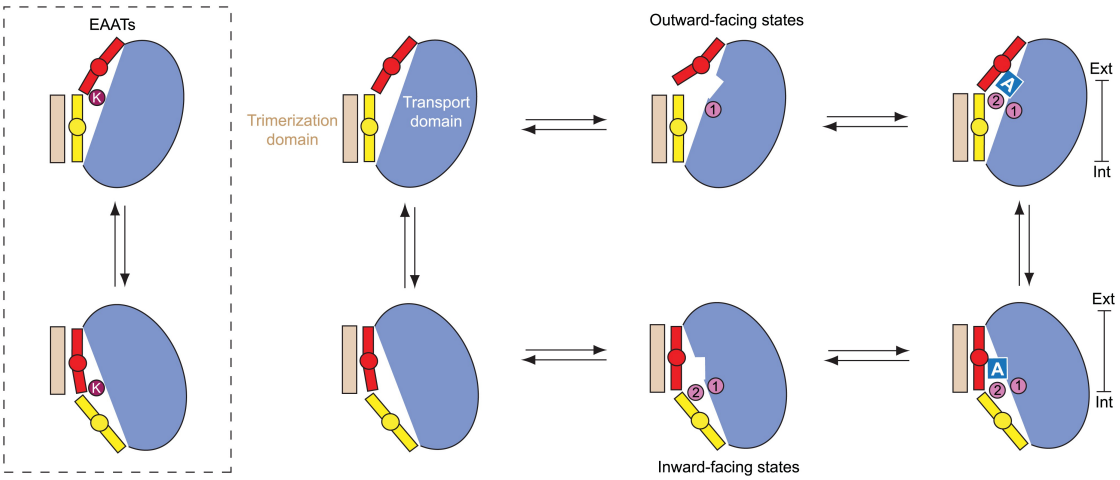

Figure 2.22. Proposed transport cycle for Glt_{Ph} and EAATs.
Ion binding to the Na1 site of the outward-facing apo transport domain triggers isomerization into bound-like conformation, formation of the L-asp and Na2 binding sites and HP2 opening, impeding translocation of the domain. Closure of HP2, coupled to L-asp and Na2 binding, allows translocation. After the release of the ligands into the cytoplasm by as yet an unknown gating mechanism, the domain is in a compact apo state, and returns to the extracellular side. Notably, binding of cations to the inward-facing state does not lead to a crystallographically observed gate opening that would impede translocation. However, Na^+ affinity in this state is only ~250 mM (Reyes et al., 2013), and it will remain largely unbound when facing the cytoplasm. Hence, uncoupled Na^+ transport should be limited. In EAATs, an open conformation of the gates might be more favored in the apo state, and K^+ binding at the Ct site might be required to stabilize translocation-competent conformation of the apo transport domain.

2.5 Materials and methods

DNA constructs, mutagenesis, protein expression, and purification

R397A mutation was introduced by PCR into Glt_{Ph} containing seven point mutations to histidine (Yernool et al., 2004), referred as wild type Glt_{Ph} for brevity. Proteins were produced in *Escherichia coli* DH10b strain (Invitrogen, Inc., Grand Island, NY) as fusions with a thrombin cleavage site, and a metal-affinity octa-histidine at their carboxyl-terminus. Proteins were purified by nickel-affinity chromatography, digested with thrombin to remove the affinity tag, and purified by size exclusion chromatography (SEC) in appropriate buffers as described below. Protein concentrations were determined by measuring the absorbance at 280 nm using an extinction coefficient of 26,820 $M^{-1}.cm^{-1}$.

Crystallization, and soaking experiments

Outward-facing state

Glt_{Ph}-R397A was purified by SEC in 10 mM HEPES/Tris, pH 7.4, 200 mM choline chloride and 7 mM *n*-decyl-α-D-maltopyranoside (Anatrace, inc., Maumee, OH). Crystallization experiments were setup using the hanging-drop vapor diffusion method, by mixing protein (~7 mg/ml) and well solutions (1:1 vol:vol), and incubated at 4°C. Na^+-bound Glt_{Ph}-R397A crystals were grown in 18–20% PEG 400, 0.1 M citric acid/Tris pH 4.5 and 0.4 M NaCl. Fully bound Glt_{Ph}-R397A crystals were obtained in the same crystallization conditions supplemented with 5 mM L-asp. The crystals were cryo-protected by soaking in the well solution supplemented with 10% glycerol and 7 mM *n*-decyl-α-D-maltopyranoside and frozen in liquid nitrogen. Apo crystals were grown in 18–20% PEG 400, 0.1 M citric acid/Tris pH 4.5, and 0.4 M choline chloride. Tl^+-bound Glt_{Ph}-R397A crystals were obtained by soaking Glt_{Ph}-R397A apo

crystals in several changes of solutions containing 18–20% PEG 400, 0.1 M citric acid/Tris pH 4.5, 0.1 M $TlNO_3$, 7 mM *n*-decyl-α-D-maltopyranoside and 10% glycerol.

Inward-facing state

Glt_{Ph}-K55C-A364C was purified by SEC in 10 mM HEPES/KOH, pH 7.4, 150 mM KCl, and 7 mM *n*-decyl-α-D-maltopyranoside. Cross-linking was carried out by mixing protein at ~3 mg/ml with a 10-fold molar excess of $HgCl_2$ for 20 min on ice. The samples were diluted ~10-fold with the SEC buffer and concentrated to remove partially the excess of $HgCl_2$. For crystallization, the protein samples at 2.75 mg/ml were supplemented with 20–50 mM $MgCl_2$ and 0.2 to 0.5 mM of a mixture of *E. coli* polar lipid extract and egg PC (3:1 wt:wt) (Avanti Polar Lipids, Inc., Alabaster, AL) and incubated on ice for 45 min. Crystallization was carried out using hanging drop diffusion methods in 96-well plates at 4°C. Initial crystallization conditions were identified using a replica of the crystallization screen MemGold (Molecular Dimensions., Altamonte Springs, FL), in which Na^+-containing compounds were replaced with K^+-containing compounds. The screen was prepared using the liquid handler Formulator (Formulatrix, Inc., Waltham, MA). Glt_{Ph}^{in}crystals were grown in 14–20% PEG 400, and 0.1 M potassium citrate, pH 5.0 to 6.0. For Tl^+ soaking, crystals were washed in 20% PEG 400, 20 mM MES/Tris, pH 6.5, 20 mM KNO_3, 20 mM $MgNO_3$, and 10 mM *n*-decyl-α-D-maltopyranoside, and then incubated in 20% PEG 400, 20 mM MES/Tris, pH 6.5, 5 mM $MgNO_3$, 10 mM *n*-decyl-α-D-maltopyranoside, and 150 mM $TlNO_3$. In ion competition experiments, the soaking solution was further supplemented with either $NaNO_3$ or KNO_3. To obtain an alkali-free structure, crystals were soaked in solution containing 20% PEG 400, 20 mM MES/Tris, pH 6.5, 5 mM $MgCl_2$, and

10 mM *n*-decyl-α-D-maltopyranoside. Crystals were directly frozen in liquid nitrogen.

Data collection and structure determination

Diffraction data were collected at the National Synchrotron Light Source beamlines X25 and X29 (Brookhaven National Laboratory). Data from crystals soaked in Tl^+ were collected at a wavelength of 0.97 Å. Data were processed using HKL2000 (Otwinowski and Minor, 1997), and further analyzed using the CCP4 program suite (Collaborative Computational Project, 1994). Anisotropy correction was performed as described previously (Strong et al., 2006). Briefly, resolution limits along the *a*, *b*, and *c* axes were determined using the UCLA–MBI Diffraction Anisotropy server (http://services.mbi.ucla.edu/anisoscale/) and applied as cutoffs to truncate the dataset obtained after processing of diffraction images. After scaling in HKL2000, structure factors were anisotropically scaled using PHASER (McCoy et al., 2007), and a negative B factor correction was applied to these structure factors using CAD. Initial phases were determined by molecular replacement with PHASER (McCoy et al., 2007), using the structure of Glt_{Ph} either in the outward-facing state (PDB code 2NWX) or the inward-facing state (PDB code 3KBC) as the search model. Refinement was carried out by rounds of manual model building in COOT (Emsley and Cowtan, 2004) and refinement in REFMAC5 with TLS (Winn et al., 2001). With the exception of the analysis of the data from alkali-free Glt_{Ph}^{in} crystals, where protomers in the trimer were clearly not identical, the electron density maps and the anomalous difference Fourier maps were three or sixfold averaged in real space. Strict non-crystallographic symmetry constrains were also applied during structural refinement in REFMAC5 when

necessary. Structures of the transport domain were superimposed and R.M.S.D.s calculated using VMD software (Humphrey et al., 1996). All structural figures were prepared using Pymol (DeLano Scientific, LLC) (DeLano, 2008).

Isothermal titration calorimetry (ITC)

ITC experiments were performed as described previously (Reyes et al., 2013). Briefly, Glt_{Ph} mutant proteins were purified by SEC in 10 mM HEPES/Tris, pH 7.4, 200 mM choline chloride, 0.5 mM *n*-dodecyl-β-D-maltopyranoside and concentrated to 4 mg/ml. The protein was diluted to 40 μM in buffer containing 20 mM HEPES/Tris, pH 7.4, 200 mM choline chloride, 1 mM *n*-dodecyl-β-D-maltopyranoside and various NaCl concentrations. ITC experiments were performed using a small cell NANO ITC (TA instruments, Inc., New Castle, DE) at 25°C. Protein samples were placed into the instrument cell and titrated with L-asp solution prepared in the same buffer. The isotherms were analyzed using the NanoAnalyze software (TA instruments, Inc., New Castle, DE), and fitted to independent binding sites model.

Fluorescence-based binding assays

Fluorescence-based binding assays were performed as described previously (Reyes et al., 2013). In brief, 100 μg/ml of protein in 20 mM HEPES/Tris, pH 7.4, 200 mM choline chloride, 0.4 mM *n*-dodecyl-β-D-maltopyranoside, 200 nM styryl fluorescent dye RH421 (Invitrogen, Inc., Grand Island, NY) were titrated with L-asp in the presence of various concentrations of NaCl at 25°C. Fluorescence experiments were carried out using a QuantaMaster (Photon International Technology, Inc., Edison, NJ). The RH421 dye was excited at

532 nm, and the fluorescence was collected at 628 nm. Fluorescence emissions were measured after at least 1000 s equilibration. The data were analyzed using SigmaPlot12 (Systat software, Inc., San Jose, CA). Fractional fluorescence changes were corrected and normalized with respect to the dilution factors and maximal fluorescence changes, respectively. Corrected fluorescence changes were plotted as a function of ligand concentration and fitted to the Hill equation. Sodium activity was calculated as $\gamma \times [Na^+]$, where γ is the activity coefficient. The activity coefficient is calculated with the Debye-Hückel equation as described (Reyes et al., 2013). All the experiments were performed at least in triplicate.

Sequence analysis

Sodium:dicarboxylate symporter family sequences were harvested from PFAM database (PF00375) (Finn et al., 2008), parsed to remove incomplete sequences and sequences with over 70% identity and aligned in ClustalW (Larkin et al., 2007). The alignment was manually adjusted and the final dataset containing 463 aligned sequences was used to generate a consensus sequence using WebLogo (Crooks et al., 2004).

Molecular modeling

To model the structures of the transport domains with HP2 in the bound conformation and the NMD motif in the apo conformation, and *vice versa*, we superimposed the structures of the fully bound and apo forms of the transport domains using TM6, HP1, and TM7. We then generated new coordinates files combining the coordinates of TM7, including the NMD motif, from the bound form and the coordinates for HP2 from the apo form or *vice versa*. In both of

these models, we observed steric clashes between Met311 and residues in HP2. To construct a model of the intermediate state with an open tip of HP2, we superimposed the structure of Na^+-only bound Glt_{Ph}-R397A and the intermediate state (PDB accession code 3V8G) using TM6, HP1, and TM7. We then replaced HP2 in the structure of the intermediate with HP2 from Na^+-only bound Glt_{Ph}-R397A. We moved slightly the side chain of Lys55 that was involved in a minor steric clash with the HP2 tip. We observed no major steric clashes in the resulting model.

CHAPTER 3

Sodium-coupled ligand binding and dissociation of a glutamate transporter homologue in an inward-facing state

3.1 Abstract

Glutamate transporters symport their substrate glutamate and three Na^+ ions across the membranes of glial and neuronal cells. The molecular mechanism of coupling between Na^+ ions and substrate is largely based on the studies of an archaeal homologue Glt_{Ph}. Both thermodynamic and structural information is available, but the kinetic mechanism of coupling has not been studied. Here, we describe a kinetic study of substrate and inhibitor binding and dissociation using a tryptophan mutant of Glt_{Ph} conformationally constrained in an inward-facing state ($P11W^{IFS}$). Our results show that Na^+ ions control the rates of both substrate binding and dissociation. First, substrate dissociation rates decrease steeply with increased Na^+ concentrations in sub-millimolar range. This observation implies that at least one Na^+ ion binds and dissociates rapidly to and from the substrate-bound $P11W^{IFS}$, and determines the rate of substrate dissociation. The rates of inhibitor binding, a process that mimics early events in substrate binding, decrease hyperbolically with the concentration of the inhibitor and increases with the concentration of Na^+ ion. These observations suggest that inhibitor and substrate binding to $P11W^{IFS}$ follows the 'conformational selection' mechanism. The rate-limiting conformational selection that precedes rapid L-asp binding depends on binding one or two Na^+ ions. Collectively the data allows us to construct a complete kinetic model of binding and release of three Na^+ ions and L-asp.

3.2 Introduction

Glutamate transporters (excitatory amino acid transporters, EAATs) move neurotransmitter glutamate across glial and neuronal cell membranes from the synaptic cleft into the cytoplasm thereby terminating neurotransmission (Danbolt 2001). Glutamate transport is a thermodynamically uphill process; cytoplasmic concentration of glutamate is nearly a million-fold higher than its extracellular concentration. To drive glutamate uptake, the transporters harness the free energy of electrochemical gradients of ions across the membrane. Transport of one glutamate molecule is coupled to symport of three sodium ions (Na^+) and one proton (H^+) and to antiport of one potassium ion (K^+) (Zerangue and Kavanaugh, 1996; Levy et al., 1998; Owe et al., 2006). Under pathophysiologic conditions, such as ischemia and stroke, when ionic gradients across cell membranes are dissipated, glutamate transporters operate in reverse, releasing glutamate from the cytoplasm into the synaptic cleft. Sustained increased glutamate concentration in the cleft leads to excitotoxicity and ultimately to cell death and brain damage (Danbolt, 2001).

Many of the structural and mechanistic insights into the transport cycle events of glutamate transporters are based on the studies of an archaeal homologue Glt_{Ph}, a Na^+/aspartate (L-asp) symporter with the transport stoichiometry of 3 Na^+ : 1 L-asp (Groeneveld and Slotboom, 2010). Glt_{Ph} shares about ~37 % of sequence identity with mammalian EAATs including conservation of many key functional residues. Overall, L-asp transport process in Glt_{Ph} and likely EAATs consists of at least four discrete reversible steps (Figure 1.3). First, substrate and ions in the extracellular space bind to the transporter in an outward-facing structural state. Second, the substrate-bound

transporter undergoes a conformational transition from the outward- to an inward-facing state, in which the substrate-binding site is accessible from the cytoplasm. Through this conformational change, the substrate and ions are translocated across the membrane. Third, the substrate and ions dissociate from the inward-facing transporter; and lastly, the substrate-free transporter undergoes a reverse conformational change back into the outward-facing state where it is ready for the next transport cycle. In EAATs, the return of the transporter into the outward-facing state also requires binding of a potassium ion (Zerangue and Kavanaugh, 1996; Levy et al., 1998).

Structural studies on Glt_{Ph} and EAAT1 showed that these proteins are homotrimers. Each protomer consists of two domains: a transport domain, which is a mobile unit harboring the substrate- and ion-binding sites, and a relatively rigid scaffold or trimerization domain. Scaffold domain provides inter-subunit interface and serves as a track for the movements of the transport domain (Figure 1.3). Comparison of crystal structures of Glt_{Ph} in the outward and inward facing states showed that the conformational transition involves a rigid-body translocation of the transport domain across the membrane by ~15 Å (Reyes et al., 2009). The energetics of Na^+-coupled substrate binding to Glt_{Ph} has been elucidated along with the corresponding structural events in the outward-facing state. The crystal structures of the apo and a Na^+-only bound mutant R397A (showing reduced affinity for the substrate) suggest that binding of one or two Na^+ ions to the outward-facing Glt_{Ph} shifts the transport domain structure from a closed apo conformation with a collapsed substrate-binding site to an open state, competent to bind substrate (Verdon et al, 2014). Consequent substrate binding favors again a closed occluded state as pictured by the crystal structure of Na^+/Asp-bound transporter. During these

binding events, a helical hairpin 2 (HP2) domain acts as a gate for Na^+ ions and substrate binding (Figure 2.11). The propensity of HP2 to open was also emphasized by the crystal structure of the transporter in complex with a transport blocker, DL-*threo*-β-benzyloxyaspartate (DL-TBOA), which seems to induce a more pronounced opening of HP2 than that observed in Na^+-only bound transporter (Boudker et al. 2007). In contrast to the detailed knowledge of the substrate binding and related gating events in the outward-facing state, how substrate dissociates from the inward-facing state is still unclear.

Several models have been proposed. For example, it was hypothesized that the helical hairpin HP1 functions as an intracellular gate based on structural pseudo-symmetry of HP1 and HP2 (Yernool et al., 2004, Reyes et al., 2009). However, unlike HP2, which shows conservation of high glycine frequency in the tip consistent with functional flexibility, HP1 contains no conserved glycine. A molecular dynamics study suggested that HP2 gates access to the substrate-binding site in the inward-facing state by providing a small local opening (Zomot and Bahar, 2013) distinct from larger HP2 motions seen in the outward-facing state. Notably, large HP2 motions would be impossible in in the canonical inward-facing state of Glt_{Ph}, because HP2 forms part of the interface between the transport and scaffold domains. Recently, a structure has been determined of a mutant of Glt_{Ph}, R276S/M395R, which shows transport rate about 4 to 5 times faster than the wild-type protein (Ryan et al, 2010, Akyuz et al., 2015). R276S/M395R mutant crystallized in an inward-facing state with two of three protomers in a distinct conformation, which was termed unlocked, such that a crevice opens between the transport and scaffold domains. Molecular dynamics suggested that a lipid molecule would likely occupy such crevice, but it can also provide space for the opening

of HP2. We hypothesize that such unlocking may constitute an integral part of the gating event in the inward-facing state allowing gating of the substrate-binding site by HP2.

To allow binding studies in isolated outward- and inward-facing states of the transporter, an approach was developed to introduce double cysteine mutations at strategic locations so that the transporter can be constrained by cross-linking (Reyes et al., 2009). Using this approach, the thermodynamics of L-asp binding to the outward- and inward-facing states was investigated (Reyes et al., 2013). It was found that the L-asp binding affinity was similar and tightly coupled to binding of three Na^+ ions in both states. Crystal structures also showed that substrate and ion coordination is largely identical in the two states (Reyes et al., 2009). Interestingly, calorimetric measurements revealed that substrate binding to both states was characterized by anomalously large heat capacity changes incompatible with simple amino acid binding to a preformed binding site. Moreover, the heat capacity changes (ΔCp) upon L-asp binding were significantly large in the inward-facing state compared to the outward-facing state. These observations suggested that the conformational changes associated with substrate binding were more complex than those revealed by crystal structures of the outward-facing state and significantly different in the inward-facing state.

Here we show kinetics of substrate binding, substrate dissociation and inhibitor binding to Glt_{Ph} constrained in an inward-facing state. The kinetic data show that Na^+ ion binding on cytoplasmic side determines the rate of both substrate binding and dissociation.

3.3 Results

Glt_{Ph} tryptophan mutant sensitive to aspartate binding and dissociation in the inward-facing state.

To investigate ligand binding and dissociation kinetics in the inward-facing state, we generated a tryptophan mutant sensitive to L-asp binding and dissociation. We replaced a proline residue in the scaffold domain, Pro 11, which is near the substrate-binding site in the inward-facing state but expected not to affect binding process directly, with a tryptophan (Figure 3.1A). The mutation was introduced in the context of the previously established Glt_{Ph} mutant, K55C/A364C constrained in the inward-facing state by a crosslink between the transport and scaffold domains (referred to as $P11W^{IFS}$) (Figure 3.1B). Notably, Glt_{Ph} contains no native tryptophan.

$P11W^{IFS}$ fluorescence emission spectrum is red-shifted and shows signal increase upon binding of Asp or an inhibitor DL-TBOA (Figure 3.1C). The red shift suggests that P11W becomes more solvent-exposed when ligands bind. It is unlikely that Trp 11 undergoes a conformational change itself because it is in trans-membrane segment (TM) 1, part of the trimerization domain which remains mostly unchanged in all crystal structures of Glt_{Ph} in either outward- or inward-facing states. Instead, a conformational change of the transport domain upon ligand binding may affect the tryptophan environment because Trp 11 is near the interface between the domains. Rigidification of the transport domain upon ligand binding may increase water accessibility to Trp 11. Both L-asp and TBOA binding show increase of fluorescence intensity, which is consistent with increased solvent exposure, away from potentially quenching amino acids.

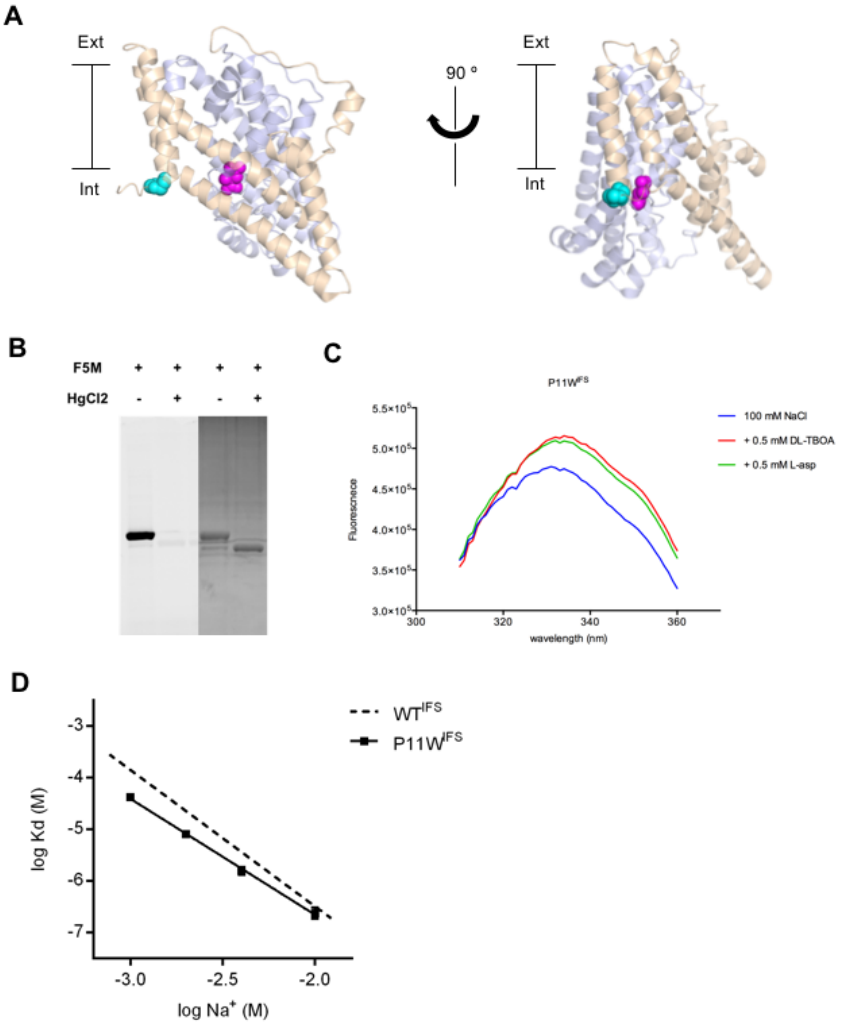

Figure 3.1. Design and characterization of P11W^{IFS} Glt$_{Ph}$.
(**A**) The position of Pro 11 in Glt$_{Ph}$. Pro 11 (cyan) is replaced with tryptophan in the context of crosslinked K55C/A364C mutant, WT^{IFS} (PDB ID: 3KBC). Pro 11 is located in the trimerization domain (wheat, transparent) and close to substrate (magenta) binding site in the transport domain (blue, transparent).
(**B**) Hg^{2+}-mediated crosslinking of P11W^{IFS}. Left panel shows a gel of fluorescein-5-maleimide (F5M) labeling of uncrosslinked and crosslinked P11W^{IFS}, imaged under blue epi illumination. Right panel represents the same gel stained with Coomassie Blue, under white epi illumination.
(**C**) Fluorescence emission spectrum of P11W^{IFS}. DL-TBOA (red) and L-asp (green) binding induced red-shift and fluorescence signal increase. Excitation wavelength was 295 nm.
(**D**) Na^+ dependence of L-asp dissociation constant, K_D, of P11W^{IFS}. The data were fitted to a solid straight line with slope of 2.2. The dashed line is a fit for Na^+ dependence of L-asp K_D of WT^{IFS}, with slope of 2.6. The data of WT^{IFS} is adapted from Reyes et al., 2013.

To confirm that P11W^{IFS} mimics Na^+ dependent L-asp binding properties of the wild type Glt_{Ph} K55C/A364C crosslinked in the inward-facing state (WT^{IFS}), we measured L-asp affinity of P11W^{IFS} in a range of Na^+ concentrations (Figure 3.1D). There are two important similarities between P11W^{IFS} and WT^{IFS}. First, the values of L-asp affinity of P11W^{IFS} are similar to those of WT^{IFS} in same Na^+ concentrations. Second, the coupling stoichiometry of Na^+ and L-asp binding to P11W^{IFS} is 2.2, similar to the coupling stoichiometry of WT^{IFS}, 2.6. It indicates that three Na^+ ion binding is coupled to 1 L-asp binding, in line with previous coupling stoichiometry studies (Groeneveld and Slotboom, 2010, Reyes et al., 2013). Deviations of the apparent number of coupled ions from three reflects incomplete coupling. Taken together, these results show that Na^+-coupled L-asp binding to Glt_{Ph} is not significantly affected by P11W mutation and the mutant can be used to study binding kinetics of Glt_{Ph}.

L-asp dissociation kinetics

P11W^{IFS} saturated with L-asp was diluted into low Na^+, L-asp-free buffer, and the decrease of fluorescence signal was measured (Figure 3.2A). The data were fitted to single exponential decay curves. These experiments produced a series of $k_{obs,diss}$ constants that decreased with increasing Na^+ ion concentration. These results show that in the fully bound Na^+/L-asp complex at least one Na^+ ion is in rapid equilibrium between bound and unbound state, and that its unbinding is a prerequisite for the release of L-asp. The data can be fitted to the following expression:

$$k_{obs,diss} = k_{-A} \frac{K_{Na}^n}{K_{Na}^n + [Na]^n} \tag{3.1}$$

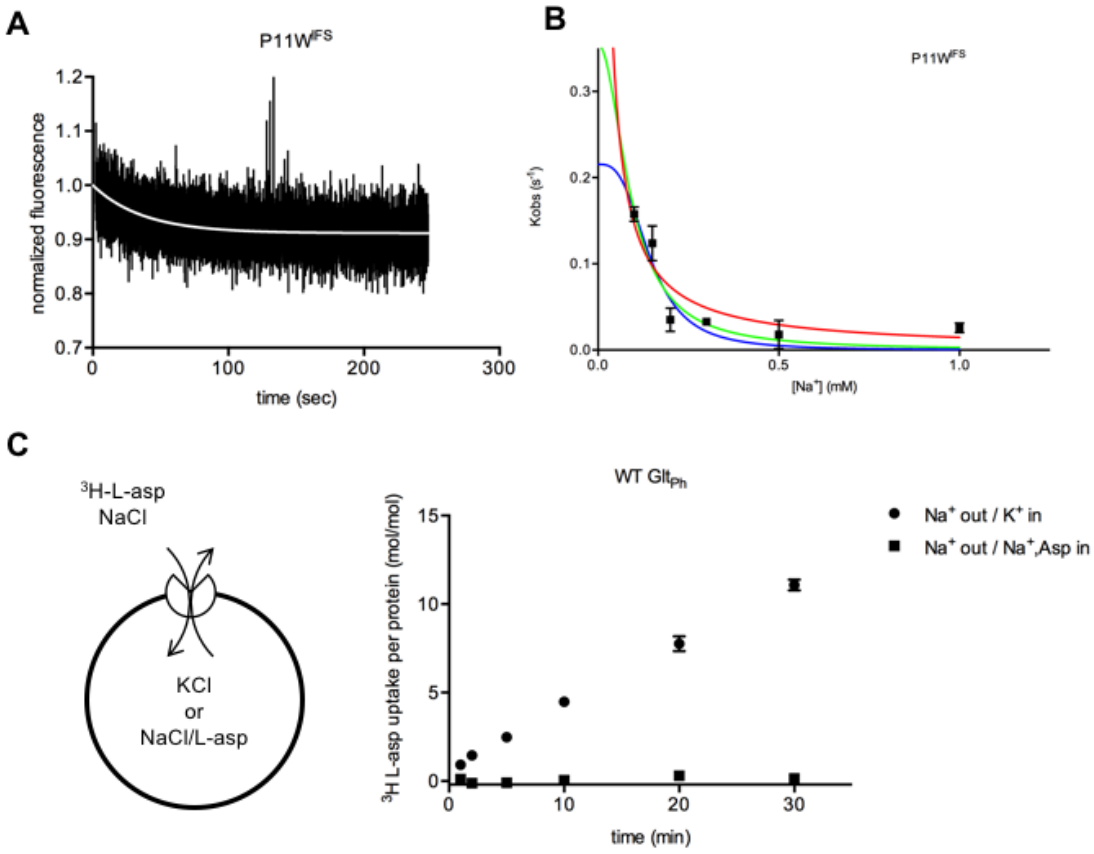

Figure 3.2. L-asp dissociation kinetics of P11W^{IFS} Glt$_{Ph}$.
(**A**) Representative image of normalized fluorescence change upon L-asp dissociation of P11W^{IFS} in the presence of 0.2 mM NaCl in solution. The white line is the fit to a single exponential decay function with $k_{obs,diss}$, 0.027.
(**B**) $k_{obs,diss}$ of L-asp dissociation as a function of solvent Na^+ concentration. The lines are the fits to the equation 3.1, with n = 1, K_{-A} = 560 S^{-1}, K_{Na} = 0.026 μM (red); n = 2, K_{-A} = 0.35 S^{-1}, K_{Na} = 8,000 μM^2 (green); n = 3, K_{-A} = 0.22 S^{-1}, K_{Na} = 3,000,000 μM^3 (blue). All experiments were performed in triplicate and standard errors are shown.
(**C**) Comparison of rate of L-asp net uptake and exchange in reconstituted proteoliposome. Wildtype Glt$_{Ph}$ proteoliposomes containing 20 mM Hepes/Tris pH 7.4, 200 mM KCl were diluted into reaction buffer 20 mM Hepes/Tris pH 7.4, 200 mM NaCl and 500 nM ^{3}H-L-asp (filled circle). Wild type Glt$_{Ph}$ proteoliposomes containing 20 mM Hepes/Tris pH 7.4, 200 mM NaCl, 100 uM L-asp were diluted into the same reaction buffer (filled box). Background radioactivity was measured in a reaction buffer containing 20 mM Hepes/Tris pH 7.4, 200 mM KCl and 500 nM ^{3}H-asp, and subtracted from the data. All uptake assays were performed at 35 °C.

where k_{-A} is the rate of L-asp unbinding once Na^+ ion(s) dissociated, K_{Na} is the affinity of the Na^+ ion(s) for the L-asp-bound transporter and n is the number of Na^+ ions that are in rapid equilibrium between bound and free states. Because k_{-A}, K_{Na} and n are significantly correlated parameters, their exact values could not be unambiguously determined. Constraining n = 1, 2 or 3, we observed that the fits with n = 2 or 3 describe data better. When n is constrained to 1, the fit is unable to recapitulate the steep drop-off of the dissociation rates. It also requires an unrealistically high affinity for the ion of 26 nM. It is also difficult to establish whether at high Na^+ concentrations, the curve approaches zero, as one would expect if Na^+ release were essential for L-asp dissociation, or a non-zero value. In this case, one would argue that at high Na^+ concentrations, a Na^+-independent L-asp release becomes dominant. Collectively, the data shows that solution Na^+ controls the rate of L-asp release. The data are most consistent with at least two Na^+ ions being in rapid equilibrium between bound and free states. At physiologically relevant Na^+ concentrations of several mM, the release of aspartate is very slow at ambient temperatures and occurs with characteristic time of no less than 100-200 sec.

To investigate whether the slow L-asp dissociation in the presence of Na^+ affects L-asp transport by Glt_{Ph} across the membrane, we reconstituted wild type Glt_{Ph} into liposomes and measured the rate of net uptake and exchange of radioactive ^{3H}L-asp (Figure 3.2C). In line with the slow dissociation in the presence of Na^+, L-asp exchange rate is very slow, almost zero, during the examined time. This remarkable slow exchange rate cannot be explained with the translocation rates of apo' (0.5 s^{-1}) and 'fully-loaded' transport domains (0.02 s^{-1}) (Akyuz et al, 2013). Thus, L-asp dissociation in

the lumen of the Na^+-loaded proteoliposomes occurs much slower than in Na^+-free proteoliposomes.

Kinetics of L-asp binding to Glt_{Ph}

In complementary binding experiments, addition of L-asp to the apo protein in the presence of Na^+ ions led to an increase of fluorescence signal from $P11W^{IFS}$ (Figure 3.3A). These curves could also be fitted to single exponential decay functions yielding $k_{obs,b}$ values. The measured rates of L-asp binding were dependent on both L-asp and Na^+ ions concentrations (Figure 3.3B and 3.3C). Notably, $k_{obs,b}$-s show non-linear dependence on [L-asp]. Therefore, L-asp binding cannot be approximated as a one-step process; at high L-asp concentrations, a substrate-independent process becomes rate limiting for the formation of the final tight complex. Interestingly, $k_{obs,b}$-s at all L-asp concentrations depend on Na^+ ion concentrations. Plotting $k_{obs,b}$-s as functions of Na^+ ions, (Figure 3.3C-E), we observe that the dependence is not linear at low L-asp concentrations. Fitting $k_{obs,b}$-s to the equation:

$$k_{obs,b} = k_{Na,b}[Na]^m \qquad (3.2)$$

where $k_{Na,b}$ is the rate constant for binding of Na^+ ions and m is the apparent number of ions bind during the rate-limiting step of L-asp binding. These results suggest that at low L-asp concentrations, binding of two Na^+ ions and L-asp determine the overall rate of complex formation. As the concentration of L-asp increases, binding of L-asp and one of the Na^+ ions are no longer rate limiting, and the rate of the overall reaction is determined by the binding of the first Na^+ ion.

Figure 3.3. L-asp binding kinetics of P11W^{IFS} Glt$_{Ph}$.
(A) Representative image of normalized fluorescence upon 0.5 mM L-asp addition to P11W^{IFS} in the presence of 4 mM NaCl in solution. The white line is the fit to a single exponential function with k_{obs}, 0.0712. (**B**) k_{obs} of L-asp binding as a function of L-asp concentration. In low L-asp concentration region, k_{obs} steeply depends on L-asp concentration, whereas in high L-asp concentration region, the L-asp-dependence of k_{obs} reduces. All experiments were performed in triplicate and means and standard error bars are shown. (**C**) k_{obs} of L-asp binding as a function of Na^+ concentration. Data represented in figure (**B**) is replotted as a function of Na^+ concentration. (**D**) Na^+ dependence of L-asp binding kinetics in low L-asp concentration. Among the data used in (**C**), k_{obs} of 0.1 mM and 0.05 mM L-asp binding are shown in red and blue, respectively. The curves are fits to quadratic equations, $k_{obs} = k_{Na}*[Na^+]^2 + k_{off,Na}$, with of k_{Na} of 0.00149 (red) and 0.00122 (blue). (**E**) Na^+ dependence of L-asp binding kinetics in high L-asp concentration. Among the data used in (C), k_{obs} of 2 mM and 1 mM L-asp binding are shown in red and blue, respectively. The lines are fits to linear equations with slope of 0.0359 (red) and 0.0244 (blue).

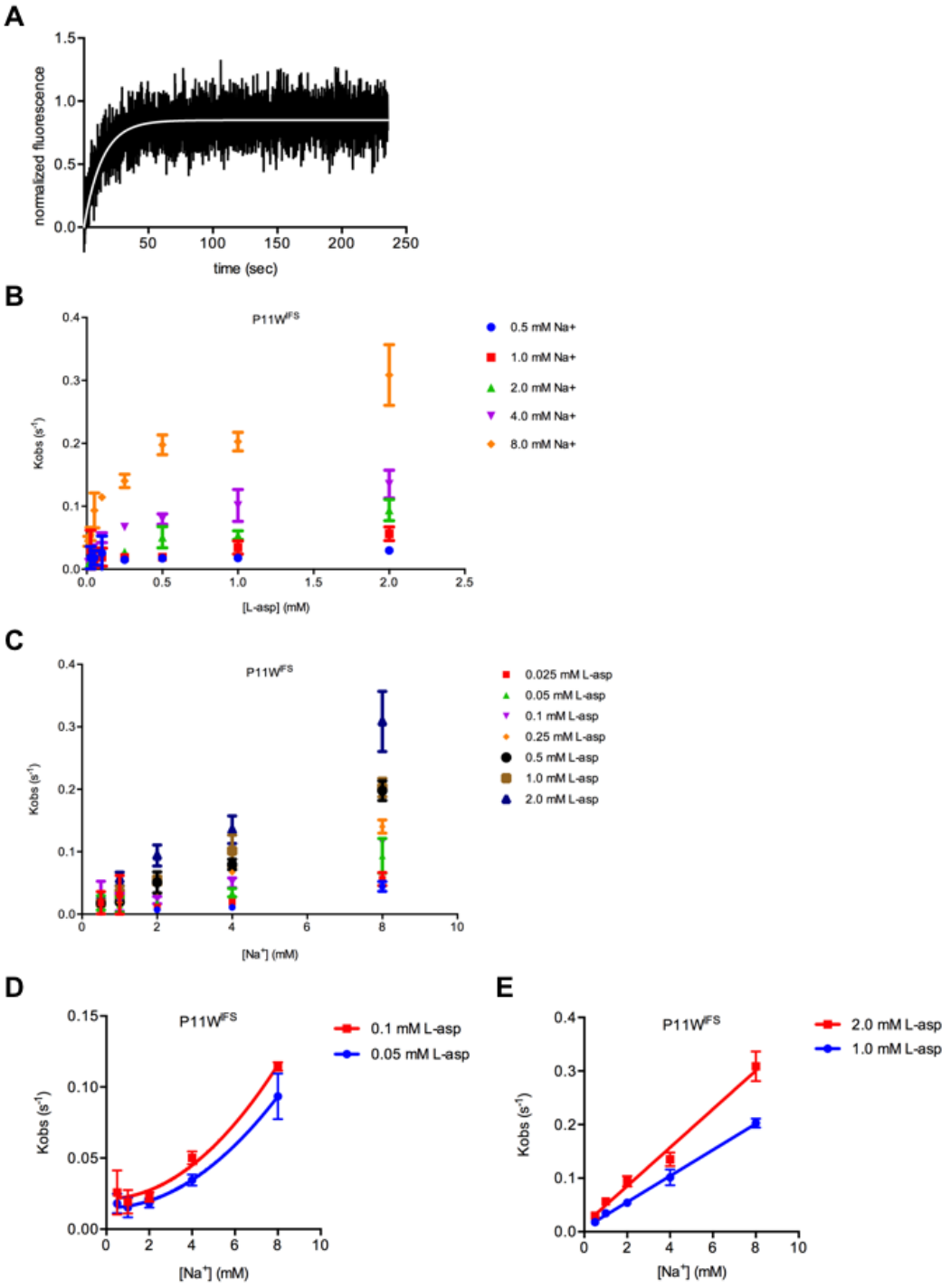
A
normalized fluorescence
time (sec)
B
P11W^FS
Kobs (s-1)
[L-asp] (mM)
0.5 mM Na+
1.0 mM Na+
2.0 mM Na+
4.0 mM Na+
8.0 mM Na+
C
P11W^FS
Kobs (s-1)
[Na+] (mM)
0.025 mM L-asp
0.05 mM L-asp
0.1 mM L-asp
0.25 mM L-asp
0.5 mM L-asp
1.0 mM L-asp
2.0 mM L-asp
D
P11W^FS
Kobs (s-1)
[Na+] (mM)
0.1 mM L-asp
0.05 mM L-asp
E
P11W^FS
Kobs (s-1)
[Na+] (mM)
2.0 mM L-asp
1.0 mM L-asp

Inhibitor binding to Glt_{Ph} follow conformation selection mechanism

The non-linear, hyperbolic increase of k_{obs} with [L-asp] indicates that during the L-asp binding reaction, there are additional rate-determining steps either before or after L-asp binding. Theoretically, there are two classical, mutually exclusive ligand binding mechanisms explaining this substrate dependency: 'induced-fit and 'conformational selection'. In 'induced-fit', isomerization of protein to higher substrate affinity state follows fast but weak initial binding. In 'conformational selection', slow isomerization of protein from a binding-incompetent state to a binding-competent state occurs before comparatively rapid substrate binding (Vogt and Di Cera, 2012). Hyperbolic increasing k_{obs} with [L-asp] can be explained by either of the mechanisms.

To distinguish the possible mechanisms of L-asp binding to the $P11W^{IFS}$, we investigated binding mechanism of DL-TBOA, which is a non-transportable blocker of glutamate transporters and Glt_{Ph} (Figure 3.4). In the outward-facing state, DL-TBOA binds in the same pocket and in the same orientation as L-asp, but its benzyl group props HP2 in an open conformation (Boudker et al., 2007). While we have been unable to crystallized complex of Glt_{Ph}^{IFS} with DL-TBOA bound, thermodynamic studies suggest that DL-TBOA and a closely related molecule L-TBA do bind to the inwardly constrained protein with affinity not too different from the outward-facing state, further supporting the idea that gating in the inward-facing state involves opening of HP2.

DL-TBOA binding is thought to mimic earlier events of substrate binding, where binding of two Na^+ ions and the ligand is completed, but HP2 is still open and the third Na^+ ion is not bound (Reyes et al, 2013). Remarkably, Figure 3.4 shows hyperbolical decrease in k_{obs} as DL-TBOA concentration is

Figure 3.4. DL-TBOA binding kinetics of P11W^{IFS} Glt$_{Ph}$.
(A) Representative image of normalized fluorescence change upon 8 mM DL-TBOA binding of P11W^{IFS} in the presence of 4 mM NaCl in solution. The white line is the fit to a single exponential function with K_{obs}, 0.2106.
(**B**) K_{obs} of DL-TBOA binding in various Na^+ conditions. The lines are the fits to the equation 3.3 with asymptotic values K_r of 0.188, 0.3168, 0.3383 and 0.4032 in 4,8,12 and 16 mM Na^+, respectively. All experiments were performed in triplicate and standard errors are shown.
(**C**) Na^+-dependence of the forward rate constant (K_r, asymptotic values in (**B**)) of conformational change before L-asp binding.

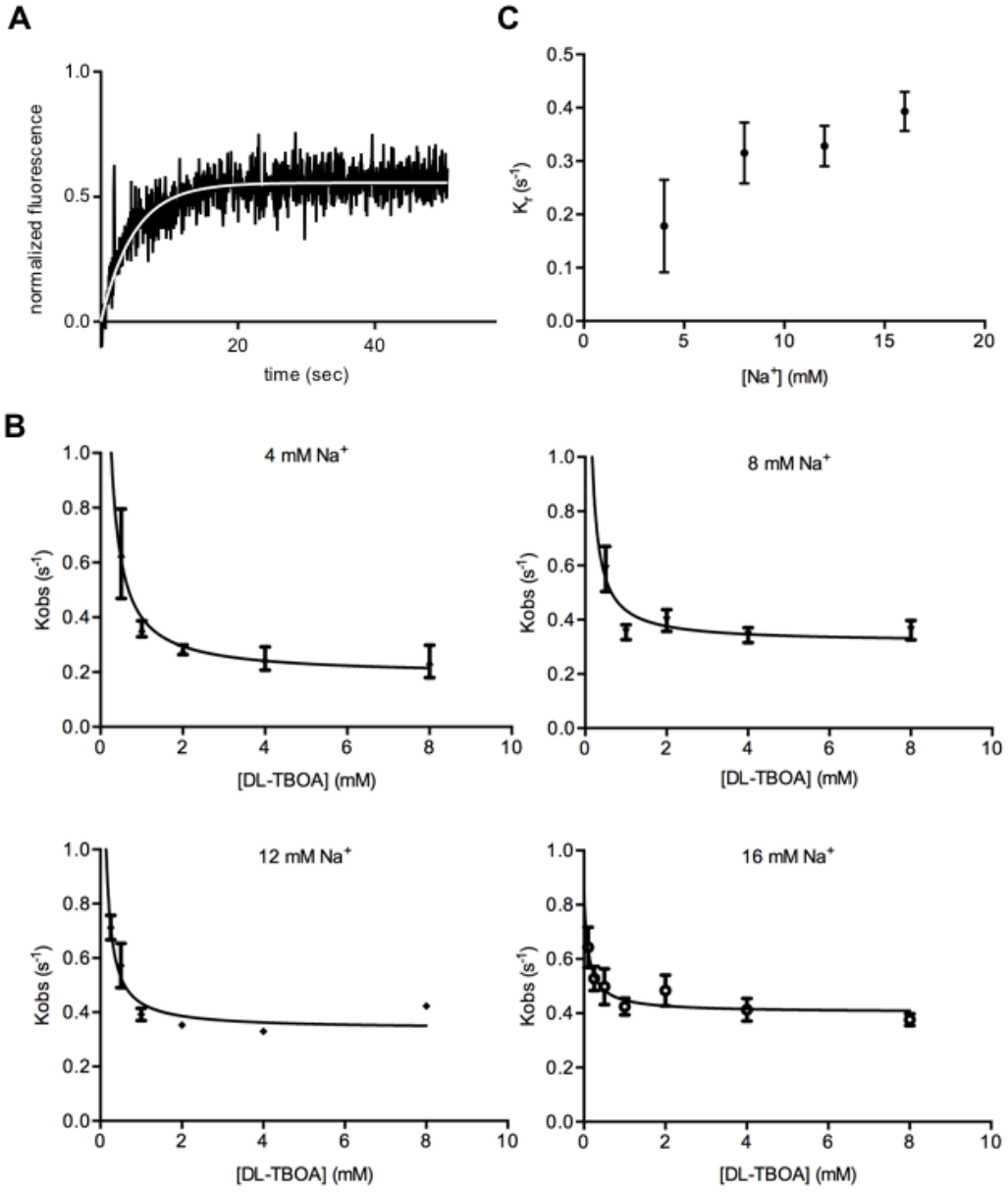
A
normalized fluorescence
time (sec)
C
K_T (s^{-1})
[Na^+] (mM)
B
4 mM Na^+
8 mM Na^+
12 mM Na^+
16 mM Na^+
Kobs (s^{-1})
[DL-TBOA] (mM)

increased, which is an obvious evidence that DL-TBOA binding follows conformational selection mechanism. Under 'rapid equilibrium approximation' in which binding and unbinding of ligand are assumed to be faster than conformational changes, we can fit the data with an equation below:

$$k_{obs} = k_r + k_{-r} \frac{K_D}{K_D + [L]} \quad (3.3)$$

where k_r and k_{-r} are rate constants of conformational change that precedes rapid binding. K_D is the dissociation constant describing the affinity of the ligand to the competent conformation of the transporter, and [L] is the concentration of DL-TBOA. Because k_{-r} and K_D are correlated parameters, their exact values could not be unambiguously determined. However, asymptotic value of k_r for [L] = ∞ can be fitted unambiguously (Figure 3.4B and 3.4C). k_r increases with Na^+ concentration suggesting that in the inward-facings state, slow Na^+ binding to the 'empty' transporter shifts the transporter to from a binding-incompetent state to a binding competent state and determines the overall rate of DL-TBOA binding. Rapid binding of DL-TBOA and likely the second Na^+ ion follows the slow initial binding of the first Na^+ ion.

Because the first Na^+ binding and related conformational change precede ligand binding, it should be common to DL-TBOA and L-asp. Thus we conclude that L-asp binding also follows Na^+-driven 'conformational selection' mechanism. However, it is not a proof that there are no slow steps following L-asp binding: unlike DL-TBOA, L-asp binding is followed by HP2 closure, and 3rd Na^+ binding.

Comparison with kinetics of substrate binding in the outward-facing state

We compared L-asp binding kinetics in the inward- and outward-facing states. To measure L-asp binding kinetics in an outward-facing state, we used a previously established outwardly-crosslinked double cysteine mutant (L66C S300C, in here we refer it as WT^{OFS}) (Reyes et al., 2013). Substrate bindings kinetics were measured using the previously established RH421 method (Figure 3.5) (Reyes et al., 2013). Figure 3.5 shows k_{obs} of L-asp binding to WT^{OFS}. It shows three interesting aspects. First, k_{obs} increases linearly with L-asp concentration. It means that L-asp binding to an outward-facing state can be approximated as a simple pseudo-first order ligand binding in the tested range. Second, k_{obs} values are approximately 5-15 folds higher than that of $P11W^{IFS}$ in same Na^+ and L-asp concentrations. Previous thermodynamics studies showed that L-asp affinities of WT^{OFS} and WT^{IFS} are almost same. For example, $K_{D,asp}$ is 220 and 211 nM in the outward- and inward-facing state in the presence of 10 mM Na^+, respectively (Reyes et al., 2013). Thus, both L-asp binding and dissociation are slower in the inward-facing state than in the outward-facing state. Third, under approximation of a simple pseudo-first order ligand binding, $k_{obs} = k_{on}*[L] + k_{off}$ with k_{on} dependent on Na^+ concentration (Figure 3.5D). To examine how many Na^+ ions are involved in determening k_{on}, we fitted the data to the equation 3.4,

$$k_{on} = k_{Na}[Na]^m \quad (3.4)$$

where k_{on} is the rate of L-asp binding, k_{Na} is the joint rate constant for Na^+ and L-asp binding and and m is the number of Na^+ ions involved. The dependence

is close to linear or quadratic. Best fit was gained when m is 1.3. It suggests that binding of one or two Na^+ ion(s) precedes L-asp binding and shifts the transporter a binding-competent state, but these events are no long rate limiting in the concentration ranges of L-asp and Na^+ that are used in these experiments. It is noteworthy, however, that there simple pseudo-first order approximation suggest that the equilibrium $K_D = k_{off}/k_{on}$. However, the ratios of the rate constants significantly underestimate known equilibrium constants. For example K_D at 1 mM is ~200 μM, while the ratio of the rate constants yields 2.9 mM. Therefore, the mechanism of binding is more complicated even if we are unable to resolve details in these experiments.

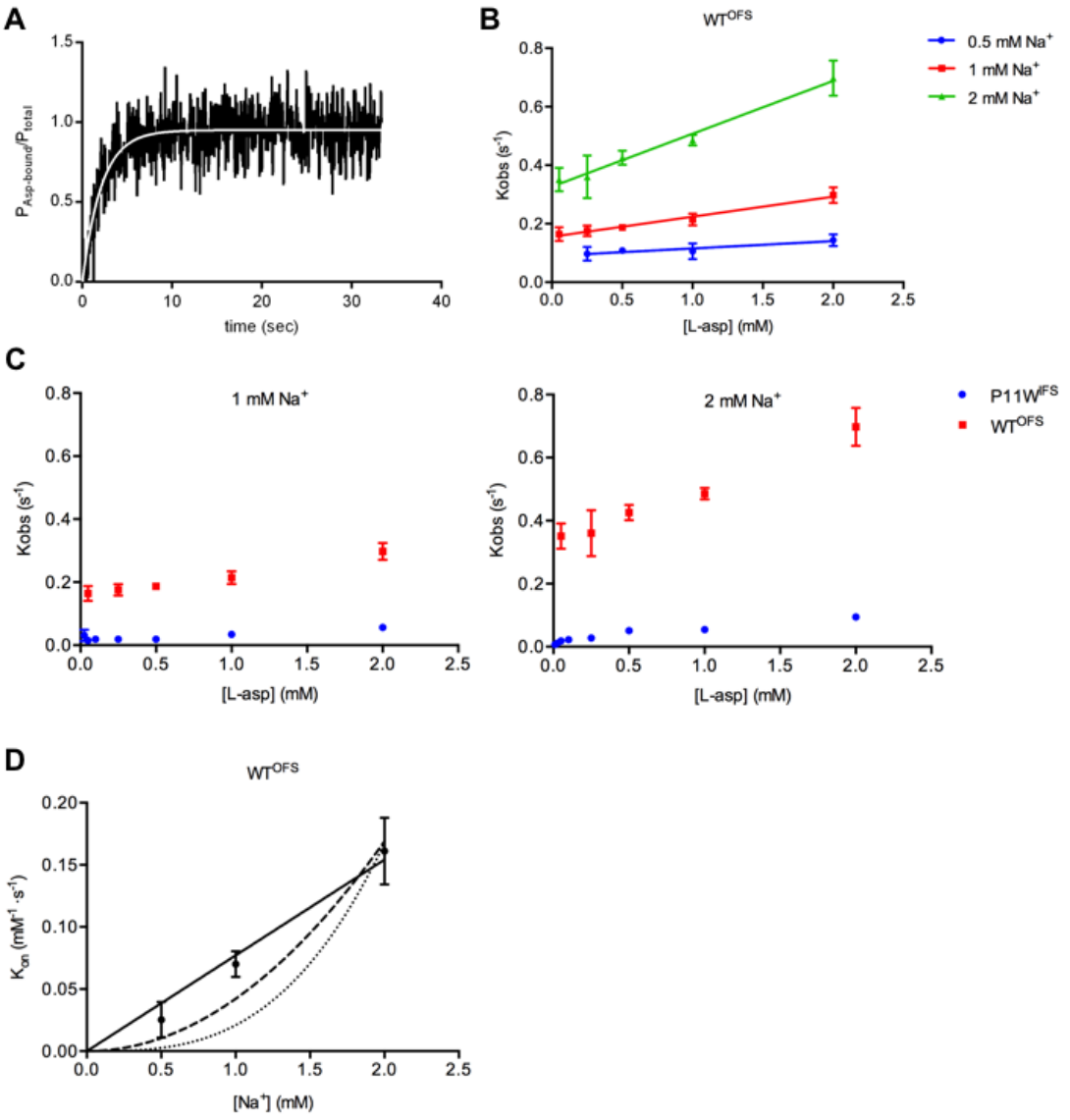

Figure 3.5. Comparison of L-asp binding kinetics of P11W^{IFS} and WT^{OFS}
(**A**) Representative image of L-asp binding kinetics of WT^{OFS}. 1 mM L-asp was added to the protein in 2 mM NaCl condition. The white line is the fit to a single exponential function with K_{obs} of 0.4689.
(**B**) K_{obs} of L-asp binding kinetics as a function of L-asp concentration. The lines are the fits to linear functions with slope of 0.025, 0.068 and 0.18 $mM^{-1} \cdot S^{-1}$, in 0.5, 1 and 2 mM NaCl conditions, respectively.
(**C**) Comparison of K_{obs} of L-asp binding of P11W^{IFS} and WT^{OFS} in same Na^+ concentrations. In brief, K_{obs} of WT^{OFS} (red) are 5-15 folds of those of P11W^{IFS} (blue).
(**D**) Na^+-dependence of K_{on} of L-asp binding of WT^{OFS}. The lines are fits to the polynomial equation 3.4, when m = 1 (solid), m = 2 (dashed) and m = 3 (dotted).

3.4 Discussion

In the transport cycle of Glt_{Ph} and EAATs, how substrate and coupled ions are released into the cytoplasm is still not understood well. Here we investigated kinetics of ligand dissociation and binding in an inward-facing state using fluorescence-based methods with a tryptophan mutant of Glt_{Ph}. To the best our knowledge, this is the first case of a kinetic study of Glt_{Ph} trapped in an inward-facing state.

The Na^+-dependence of k_{obs} of L-asp dissociation (Figure 3.2) suggests that at least one Na^+ ion binds to and dissociates from substrate-bound state Glt_{Ph} in the inward-facing state. In other words, at least one Na^+ ion dissociation precedes L-asp dissociation from the inward-facing state, and the Na^+ ion dissociation determines the rate of L-asp release. L-asp dissociation is very slow even in low Na^+ concentrations (k_{obs} ~0.02 sec^{-1} at 0.5 mM Na^+), and gets slower as Na^+ concentration increases. The slow dissociation can be a reason of why L-asp exchange rate is almost zero (Figure 3.2C) in our liposome experiments. In the L-asp exchange experiments, we have high concentration of Na^+ (200 mM) on both sides of the liposome membrane. Thus whether the transporter was in apo or asp-bound, once L-asp binds, it is not released from the transporter in our time scale (30 mins). The Na^+ ion dissociation preceding L-asp dissociation probably happens in Na2 site, which has been thought the last Na^+ binding occurs in Glt_{Ph} and EAATs (Huang and Tajkhorshid, 2010). Previous crystallographic studies show that only the Na2 site among three Na^+ sites is immature before substrate binding even in high Na^+ concentration (Verdon et al., 2014, Boudker et al., 2007).

The Na^+-dependence of k_{obs} of L-asp binding (Figure 3.3) gives us insight of sequence of binding of L-asp and three Na^+ ions. In low and high L-

asp concentrations, Na^+-dependence of k_{obs} are quadratic and linear, respectively. How the Na^+-dependence can be different in different ligand concentrations? The difference reminds us a previously proposed scheme of sequence of binding of the substrate and three Na^+ ions to Glt_{Ph} (Huang and Tajkhorshid, 2010). In the scheme, there are two possibilities after the first Na^+ binding; 1) second Na^+ binds, then substrate binds, and the third Na^+ binds at last, or 2) substrate binds, then second Na^+ binds, and the third Na^+ binds at last. The scheme is well consistent with the results. In low L-asp concentration, the possibility 1 is dominant, two Na^+ bindings preceding L-asp binding determine the rate of L-asp binding (quadratic dependence). In high L-asp concentration (and low Na^+ concentration), on the other hand, the possibility 2 is dominant, one Na^+ binding preceding L-asp binding determines the rate of L-asp binding (linear dependence).

Hyperbolic decrease of k_{obs} with DL-TBOA concentration (Figure 3.4) unambiguously shows that DL-TBOA binding follows the 'conformational selection' mechanism and the 'conformational selection' is a rate-determining step of DL-TBOA binding to Glt_{Ph} in the inward-facing state. Interestingly, the forward rate of the conformational selection, K_r, depends Na^+ concentration (Figure 3.4C). Thus we suggest that the slow 1 or 2 Na^+ binding induces conformational change of Glt_{Ph} to ligand-binding-competent state and determines the rate of ligand binding, in the inward-facing state. It is in line with the previously kinetics studies of uncrosslinked Glt_{Ph} which show that one or two Na^+ binding precedes L-asp binding (Ewers at al., 2013, Hanelt et al., 2015). Taken together our results and the previously structural and functional studies, we hypothesize the structural basis of the slow 'conformational selection'. First Na^+ binding in Na1 site is associated with flipping of the

strongly conserved NMD motif. Met311 side chain towards out from the substrate binding site in apo and flips in when Na1 is occupied. The NMD motif flipping is associated with reshaping (or opening) of HP2 domain (Verdon et al., 2014). In the inward-facing state, the reshaping of HP2 domain is more restricted than in the outward-facing state because of its structural environment. Then one can suspect that Na^+ binding is weaker in the inward-facing state than the outward-facing state. Indeed, $k_{D,Na+}$ of the inward-facing state about three-fold higher than of the outward-facing state: 198.0 mM and 64.2 mM, respectively (Reyes et al., 2013). Also, one can expect that Na^+-associated conformational selection before ligand binding in the outward-facing state is faster than in the inward-facing state. As expected, $k_{obs,L\text{-}asp}$ in the WT^{OFS} is linear with L-asp concentration rather than hyperbolic (Figure 3.5).

The 'conformational selection' step precedes ligand binding step. Therefore, it is reasonable to assume that the same event occurs before L-asp and DL-TBOA binding to Glt_{Ph} in an inward-facing state. However, $k_{obs,L\text{-}asp}$ hyperbolically increases with L-asp concentration unlike DL-TBOA binding. It tells us that L-asp binding occur under a certain condition of 'conformational selection' in which the rate of ligand dissociation (k_{off}) is smaller than the rate of conformational change (k_r) (Vogt and Di cera, 2012). The slow dissociation is well consistent with the results from our direct measurement of L-asp dissociation rate (Figure 3.2). Then why the dissociation of L-asp is slow otherwise the dissociation of DL-TBOA is fast? We can find an answer from the crystal structures of Glt_{Ph}. In L-asp-bound states, the substrate binding site is closed by HP2 domain and separated from the solvent and Na2 site is fully formed and occupied by Na^+ ion (Boudker et al., 2007, Reyes et al., 2009). In

DL-TBOA-bound state, HP2 domain is prevented from closure because of the benzoyl group of DL-TBOA props it, and the substrate binding site is open to the solvent, and Na2 site is not formed (Boudker et al., 2007). As we mentioned above, the first Na^+ dissociation determines the rate of ligand dissociation. The tested Na^+ concentration region (0.5 ~ 8 mM) is already high enough to occupy Na2 site in L-asp-bound state, thus L-asp dissociation is slow. On the other hand, L-TBOA-bound state mimics the state after the first Na^+ dissociation from Na2 site and therefore DL-TBOA dissociation is fast. Moreover, in the L-asp-bound, inward-facing state, HP2 domain faces the scaffold domain (TM2 and TM5) and tightly packed in the interface of the transport and the scaffold domain. Thus conformational change of HP2 domain, which is required for binding and dissociation of L-asp, might be slow in the inward-facing state and therefore reduce the rate of L-asp dissociation in the inward-facing state.

Our kinetics studies give insight into how Na^+ ion bindings on cytoplasmic side determine the rate of substrate binding and dissociation of Glt_{Ph} on the cytoplasmic side of the membrane. Taken together our results, we propose a scheme of Na^+-coupled L-asp binding mechanism of Glt_{Ph} in an inward-facing state (Figure 3.6). The first, slow Na^+ binding induces conformational change of Glt_{Ph} to an ‘open’ state which is competent to ligand binding. After the first Na^+ binding, to the ‘open’ state of the transporter, either second Na^+ or ligand binding occurs, then the other binding follows. The third Na^+ binding with high affinity ‘locks’ the transporter, and prevent release of ligand.

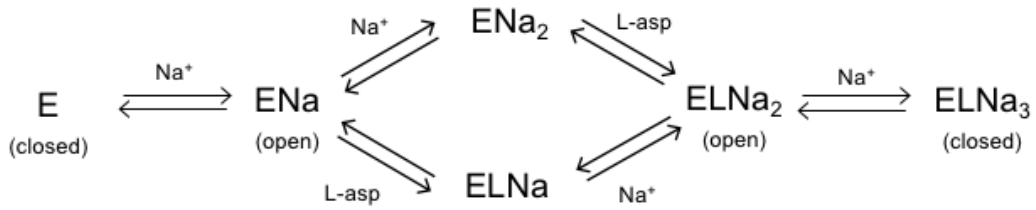

Figure 3.6. A scheme of Na^+ and L-asp binding of Glt_{Ph} in an inward-facing state. E, L and Na represent Glt_{Ph} in an inward-facing state, L-asp and Na^+ ion, respectively. All steps are reversible.

3.5 Materials and methods

Mutagenesis, protein expression, and purification

All Glt_{Ph} mutants were expressed and purified as described previously (Boudker et al., 2007, Reyes et al., 2009). In brief, glycerol stock of Glt_{Ph} mutant were inoculated in small volume of LB with 100 mg/ml ampicillin, and incubated at 37 °C, 220 rpm overnight. The cultures were diluted in large volume of LB/ampicillin media then grown at 37 °C, 220 rpm. After 0.2 % L-arabinose induction at $O.D_{600}$ = 0.6, culture were incubated 3 hrs at 37 °C, 220 rpm. Cells were harvested by centrifuge in 5,000 rpm, 15 min, at 4 °C. Cell pellets were frozen in liquid nitrogen and stored at -80 deg. Thawed cell pellets were disrupted by pressure ~15,000 psi, 4 times. Cell debris were removed by centrifuge, 8,000 rpm, 15 min at 4 °C. Supernatant were ultracentrifuged in 40,000 rpm, 1 hr at 4 °C. Pelleted membranes were homogenized in 20 mM HEPES/Tris pH 7.4, 200 mM NaCl buffer and ultracentrifuged again in 40,000 rpm, 1 hr at 4 °C. Washed membranes were homogenized and then solubilized in the same buffer supplemented with 40 mM DDM for 1 hr. Solubilized proteins were separated by ultracentrifugation 40,000 rpm, 1 hr at 4 °C. Separated solubilized proteins were incubated with 10-15 mL of pre-equilibrated Ni-NTA resin (QIAGEN) in cold room with gentle shaking. Protein-bound Ni-NTA resin was washed with seven column volume (CV) of 20 mM HEPES/Tris pH 7.4, 200 mM NaCl, 40 mM imidazole and 1 mM DDM. Proteins were eluted with 5 CV of 20 mM HEPES/Tris pH 7.4, 200 mM NaCl, 250 mM imidazole and 1 mM DDM. Eluted proteins were concentrated using Amicon Ultra (100 KDa cutoff). After Ni-NTA affinity chromatography, His-tag was cleaved by thrombin at room temperature, overnight. Then proteins were

further purified using size exclusion chromatography (GE Healthcare) with 20 mM HEPES/Tris pH 7.4, 300 mM Choline Cl and 1 mM DDM.

Crosslinking

To crosslink, 10-molar fold of $HgCl_2$ was added to the protein solution after imidazole in protein solution was removed by filtration with Amicon Ultra (100 kDa cutoff). Crosslinking takes 15 minutes at room temperature. Crosslinked proteins were purified using size exclusion chromatography (GE Healthcare). Peak fractions were collected and concentrated. Concentrations of protein samples were measured in Nanodrop (ThermoFisher Scientific) with an extinction coefficient determined using ProtParam on the ExPASy server (Gasteiger et al., 2005). To check existence of free thiol after crosslinking, purified proteins were labeled with 5-molar fold of fluorosein-5-maleimide (F5M). F5M labeled proteins were imaged in a SDS-PAGE gel under epi blue illumination (Bio-rad). The same gel was imaged under epi white illumination after coomassie staining.

Fluorescence-based kinetics assay.

For emission scan, 1 uM of protein sample in 2 mL of 20 mM HEPES/Tris pH 7.4, 300 mM Choline chloride and 1 mM DDM wasexcited at 295 nm and emission-scanned from 300 to 500 nm (PTI instrument), in the absence and presence of Na^+ and ligand. Baseline was determined by scanning buffer only, and subtracted from data. For real-time fluorescence measurement upon ligand dissociation, protein sample in 20 mM Hepes/Tris pH 7.4, 300 mM ChoCl, 10 mM NaCl, 0.5 mM L-asp was diluted into 100-fold (volume) of buffer with various NaCl concentration with fast stirring at 25 °C. Final concentration

of the protein in dilution buffer was 1 uM. For real-time fluorescence measurement upon ligand binding, 1 uM of protein sample in 2.0 mL of 20 mM HEPES/Tris pH 7.4, 300 mM Choline chloride and 1 mM DDM with various NaCl concentrations were incubated at 25 °C until the fluorescence signal is in plateau, then ligands were added with fast stirring. Excitation/emission wavelengths were 295/350 nm and 532/628nm for tryptophan fluorescence and RH421 fluorescence, respectively. All experiments were performed at 25 °C. Data were analysed using SigmaPlot 12.0 (Systat Software, Inc)

Protein reconstitution into liposome

Wildtype Glt_{Ph} was reconstituted into liposomes as previously described (Ryan et al., 2009, Boudker et al., 2007). In brief, 0.1% chicken rhodamine B labeled PE (L-α-Phosphatidylethanolamine-N-(lissamine rhodamine B sulfonyl) (Ammonium Salt) (Avanti Polar Lipids, Egg-Transphosphatidylated, Chicken) was mixed with 3:1 (w/w) mixture of *E.coli* polar lipid extract and egg phosphatidylcholine (Avanti Polar Lipids), dried in rotary evaporator and vacuum overnight. The mixture was wet by buffer 20 mM Tris/HEPES, pH 7.4 and 200 mM KCl to final concentration 5 mg/ml, by freeze and thaw in liquid nitrogen and at RT, 10 times, and formed multi-lamellar liposomes. The liposomes were extruded through 400 nm filter membrane (Whatman) 10 times to form uni-lamellar liposomes. The liposomes were used to make calibration line for liposome concentration by rhodamine fluorescence, excitation and emission wavelengths were 560 and 583 nm, respectively. The liposomes were destabilized by addition of TX-100 (0.5:1 (w/w), TX-100 to lipid) (Sigma-Aldrich). Proteins were added to the destabilized liposome at a ratio of 1:1000 (w/w) of protein to lipid, and incubated for 30 mins at RT. To

reconstitute the protein into liposomes, detergents in the mixture were removed by three rounds of incubation with 80 mg/ml of pre-washed SM-2 biobead (Bio-rad): 2 hrs at RT, 2 hrs in cold room and overnight in cold room. The proteoliposomes were extruded again through 400 nm filter, 10 times. The proteoliposomes were concentrated by ultracentrifugation, 40,000 rpm, 45 min at 4 °C. To exchange buffer inside of the proteoliposomes, supernatant was removed and 1 mL of appropriate buffers were added. After gentle agitation, the proteoliposomes were frozen in liquid nitrogen and thawed at RT, three times. The proteoliposomes were extruded again through 400 nm filter, 10 times. After concentration by ultracentrifugation, supernatants were removed. Small volume of appropriate buffers was added and gently mixed. Concentration of the proteoliposomes were measured by rhodamine fluorescence.

Uptake assay

To start uptake or exchange of radioactive aspartate, the prepared proteoliposomes were diluted into reaction buffer 20 mM Hepes/Tris pH 7.4, 200 mM NaCl, and 500 nM ^{3}H-asp, at a volume ratio of 1:1000. All uptake assays were performed at 35 °C. At time points, 200 µl of reaction mixtures were aliquoted and diluted into 2 mL of ice-cold quenching buffer, 20 mM Hepes/Tris pH 7.4, 200 mM LiCl, then immediately filtered through 0.22 µM filter membrane (Millipore) and washed with 3 mL of the ice-cold quenching buffer. The washed filter membranes were transferred into scintillation vials and filled with scintillation liquid (RPI Research products international). Scintillations were measured in LS6500 multi-purposed scintillation counter (Beckman Coulter).

CHAPTER 4

SUMMARY AND FUTURE DIRECTIONS

4.1 Summary

EAATs transport neurotransmitter glutamate from the synaptic cleft into cytoplasm and thereby terminate neurotransmission. The glutamate transport is coupled to 3 Na^+ ion symports, 1 proton symport and 1 K^+ ion antiport. The ion-coupled transport mechanism is not understood well because of lack of the available high-resolution structure of EAATs. In this thesis, we studied Na^+ coupled substrate binding and gating mechanism of GltPh, an archeal homologue of EAATs, using X-ray crystallography, fluorescence-based substrate binding assay, uptake assay and isothermal titration calorimetry.

Here we reported new crystal structure of Glt_{Ph} in ligand-free and Na^+-only bound outward- and inward-facing states. Comparisons of those structure enrich our understanding of the mechanism of Na^+ coupled substrate binding and gating of Glt_{Ph}, and in analogy, EAATs. The structures of the transport domain in apo, outward- and inward-states are same to each other, but different from substrate-bound, outward- and inward-states. It means that the translocation of the 'empty' transport domain across the membrane is a 'rigid-body' movement, and the movement is different from that of the 'fully-loaded' transport domain.

In apo state, the substrate binding site is blocked from the solvent, by HP2 domain, an extracellular gate. However, in Na^+-bound state, the site is open to the solvent because of the conformational changes of HP2 domain. The blocking and opening of the substrate binding site explains why substrate binding affinity is low (almost zero) and highly increases in the absence and

presence of Na^+, respectively. Striking structural change of NMD motif in TM7 was observed from the comparison of apo and Na^+-bound states. The side chain of the methionine shows flipping toward out and in upon Na^+ binding. Thus we hypothesize that the Met is a key residue for the coupling of Na^+ and substrate binding. Indeed, the Met to Ala mutation almost lose the coupling Na^+ and substrate binding but the Met to Leu mutation maintain the coupling. We also identified a new cation binding site from Thallium soaks of Glt_{Ph} crystals. The site overlaps with substrate binding site. It means that ion binding to a corresponding site in EAATs can compete with substrate binding. Loss- and gain-of-function mutagenesis studies of dicarboxylate transporters and EAATs have shown that the residues making up the corresponding site is critical for K^+ coupled transport. Also the corresponding site in EAATs has been predicted a K^+ binding site. Thus we propose that the corresponding site of the newly identified cation binding site in EAATs is the K^+ binding site. Taken together the results, we suggest a Na^+-coupled transport mechanism of Glt_{Ph} and EAATs.

To understand the mechanism of substrate and ion binding in the cytoplasmic side, we studied kinetics of substrate release, binding and inhibitor binding to Glt_{Ph} in an inward-facing state using a tryptophan mutant sensitive to ligand binding and release. The kinetics of substrate release and binding strongly depend on Na^+ concentration in the solvent. The results suggest us two interesting points of Na^+-coupled substrate binding and release. First, the rates of substrate binding and release are determined by the first Na^+ binding and the first Na^+ release, respectively. Second, the sequence of second Na^+ and substrate binding after the first Na^+ binding is not fixed. Both bindings are possible, and the sequence is determined by concentrations

of Na^+ and L-asp. For example, substrate binding occurs before the second Na^+ binding in high substrate concentration. The inhibitor binding kinetics study suggests that substrate and inhibitor binding follows the 'conformational selection' mechanism, and the rate of conformational selection depends on the Na^+ concentrations. It means that the first Na^+ binding determines the rate of conformational selection and ultimately, the rate of substrate binding. Taken together the kinetics studies, we suggested a scheme of Na^+ and substrate binding to and release from Glt_{Ph} in an inward-facing state.

4.2 Future directions

In chapter 2, we showed crystal structures of Glt_{Ph} in an apo, outward-, apo, inward- and Na^+-bound, outward (open) states. Taken together with previously solved crystal structures, we proposed a model of transport cycle of Glt_{Ph} (Figure 2.22). The only hypothetical part in the model is 'inward-open' state because we have no structure available. In chapter 3, we studied how Na^+ bindings facilitate ligand binding and release in the inward-facing state. The kinetics is expected to be associated with opening and locking of the substrate binding site. To fully understand how Na^+ bindings open and lock the transporter, structural studies of Na^+-bound or an inward-open state will be necessary. Taken together, structural information of Glt_{Ph} in an inward-open state is invaluable to complete the model and to understand how ligand and Na^+ ions are released into cytoplasm in Glt_{Ph}, an in analogy, EAATs.

APPEDIX A

A highly-conserved arginine residue in substrate binding site controls Na^+ binding in Glt_{Ph}

A.1 Abstract

In Na^+ coupled mammalian glutamate transporter family, they have a strongly conserved arginine in transmembrane domain 8 (TM8). It has been suggested that the arginine locates in substrate binding site and interacts with substrate directly. Indeed, in crystal structures of Glt_{Ph}, an archaeal homologue Na^+ coupled aspartate transporter, in substrate-bound conformations the side chain of Arg 397 directly interacts with the ß-carboxyl group of the substrate L-aspartate. Many mutagenesis studies have supported that this arginine is a key residue for substrate binding and specificity in Glt_{Ph} and mammalian glutamate transporters. However, role of the arginine in Na^+ binding has not been investigated well. Here I show that the arginine controls Na^+ binding to Glt_{Ph}. Replacement of the arginine by alanine (R397A) shows remarkably increased Na^+ affinity, whereas replacement by lysine shows no significant change. As previously shown, Na^+ binding affinity increases in substrate-bound conformations, in other words, when negative charge occupies substrate-binding site. Furthermore, K^+ can inhibit Na^+ binding in R397A whereas affect insignificantly in wild type. Taken together, I propose that positive charge in substrate binding site decreases Na^+ binding to Glt_{Ph} and glutamate transporters, and facilitates Na^+ release from the transporters.

A.2 Introduction

In brain mammalian glutamate transporters (EAATs) on the membrane of neuronal cells uptake neurotransmitter glutamate from the synaptic cleft and terminate neurotransmission. To capture glutamate EAATs have an arginine, a strongly conserved residue that directly interacts with the gamma-carboxyl group of glutamate. It has been shown that the arginine play important roles in substrate binding and specificity. When the arginine is replaced by neutral amino acids, EAATs lose glutamate binding and gain increased binding to other neutral amino acids such as cysteine and serine.

Structural information of the arginine has been gained mainly from the crystal structures of Glt_{Ph}, an archaeal homologue of EAATs. In the crystal structures of Glt_{Ph} the arginine, Arg 397, locates substrate-binding site and directly interacts with beta-carboxyl group of its substrate aspartate. In the absence of substrate, the side chain of Arg 397 moves and partially occupies substrate-binding site. Figure A.1 shows the arginine movement in crystal structures of Glt_{Ph}. The side chain of the arginine occupies substrate-binding site in the apo conformations, while moves away from the substrate-binding site and interacts with D390 and Y317 (Glt_{Ph} numbering) in the asp-bound conformations.

Both EAATs and Glt_{Ph} are Na^+ coupled transporters with a stoichiometry of 3 Na^+ for 1 substrate molecule. The coupling is strikingly tight: Na^+ binding and substrate binding encourages each other whereas in the absence of either, binding of the other is very low. For Na^+ binding, Kd is ~ 100 mM in the absence of substrate. Taken together with the arginine movements mentioned above, I hypothesize that the arginine also play a role in Na^+ binding to EAATs and Glt_{Ph}. Getting rid of the side chain by alanine

mutation R397A increased Na^+ binding. Binding of substrate, a negatively charged amino acid, L-aspartate, increased Na^+ binding. Also, addition of a positive charged ion K^+ inhibits Na^+ binding to R397A, whereas inhibition by K^+ was not observed in Na^+ binding to wild type Glt_{Ph}. I also tested mutations that affect on preference or steric hindrance of arginine side chain in substrate binding site.

Taken together I propose that positive charge in substrate binding site weaken Na^+ binding to Glt_{Ph} and EAATs, and thus facilitates Na^+ unbinding im their apo conformations. This property might contribute to give EAAT functional identity as net transporters, rather than exchangers.

A.3 Results

R397A mutation increases Na^+ binding to Glt_{Ph}

To test arginine inhibits Na^+ binding to Glt_{Ph}, I mutated the arginine 397 (R397) to alanine, which has a smaller side chain and neutral charge, and measured Na^+ binding to the R397A mutant. Dissociation constant (Kd) of Na^+ binding to R397A mutant in 600 mM choline chloride (ChoCl) at pH 7.4, was ~15 mM, whereas Na^+ Kd is ~70 mM for wild type in the same experimental condition (Figure A.1, A.2). Even Na^+ binding affinity increases in an engineered Glt_{Ph} in which R397 is replaced by citrulline, which has the same size of side chain but neutrally charged (personal communication with PJ Focke). In contrast, the arginine to lysine (R397K) mutant shows similar Na^+ Kd (~90 mM) with that of wild type (Figure A.3). It seems that when positive charged group occupies substrate-binding site, Na^+ binding affinity is low. In the presence of aspartate, in both wild type and R397A, Na^+ affinity is highly increased. Na^+ Kd is ~4 mM in 1 uM asp and ~6 mM in 1 mM asp for wild type and R397A, respectively (Figure A.1 and A.2). In summary, when positively charged side chains such as arginine and lysine are in substrate binding site, Na^+ binding affinity is very low, but when the positive charged group is removed from the binding site like in R397A or replaced by negative charged group such as aspartate, Na^+ affinity is highly increased in Glt_{Ph}.

K^+ inhibits Na^+ binding to R397A

To test other kinds positive charge in substrate binding site can also reduce Na^+ binding site, I measured Na^+ binding in R397A in the presence of K^+, which has 6 Å effective radius similar to van der Waals radius of side chains arginine and lysine (Levitt, 1976). Figure A.1 shows Na^+ binding to R397A

measured by using voltage-dependent styryl dye, RH421, in various concentrations of KCl (total salt concentrations were maintained in 600 mM, choline chloride was used as a replacement cations in the left and middle panels, 100 mM in the right panel). In the absence of L-asp, dissociation constants (Kd) of Na^+ binding in 0 and 600 mM KCl are 3.5 folds: 15.4 mM and 53.5 mM, respectively. In the presence of L-asp, Kds of Na^+ binding in 0 and 600 mM KCl are 3.8 folds: 4.2 mM and 15.9 mM, respectively. However, in 100 mM salt condition, Kds in ChoCl and KCl show no significant difference; 18.9 mM and 23.6 mM, respectively. The results reveal that a small positive charge such as K^+ inhibits Na^+ binding whereas larger ones such as $choline^+$ does not inhibit Na^+ binding in R397A.

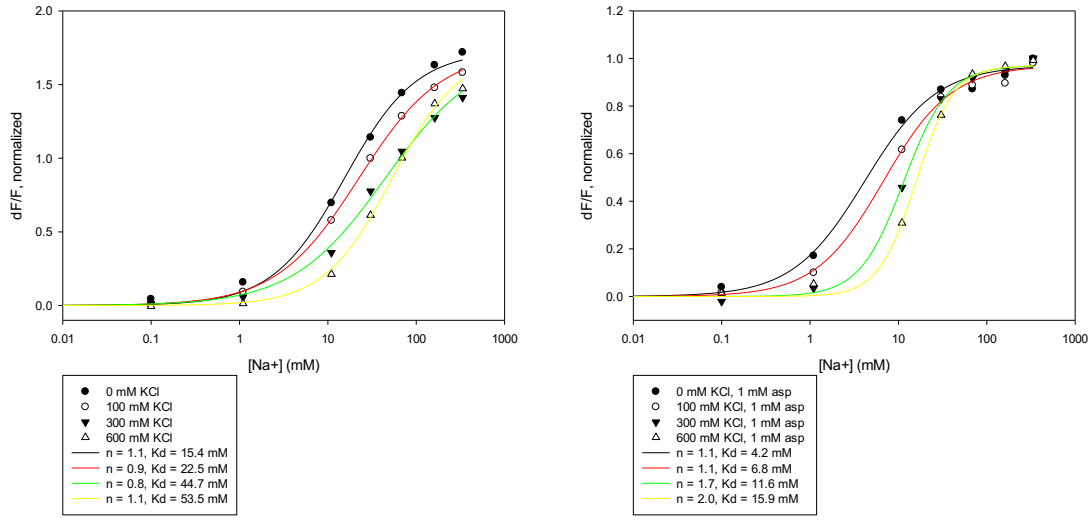

Figure A.1. K^+-dependent Na^+ binding to R397A. Na^+ titrations in 0 mM (filled circles), 100 mM (empty circles), 300 mM (inverted triangles) and 600 mM KCl (empty triangles) in the absence of L-asp (left) and in the presence of 1 mM L-asp (right) are shown. Ionic strength was maintained by replacement of KCl by choline chloride. All titration curves are fitted in Hill equation. Hill coefficients and Kd values are shown.

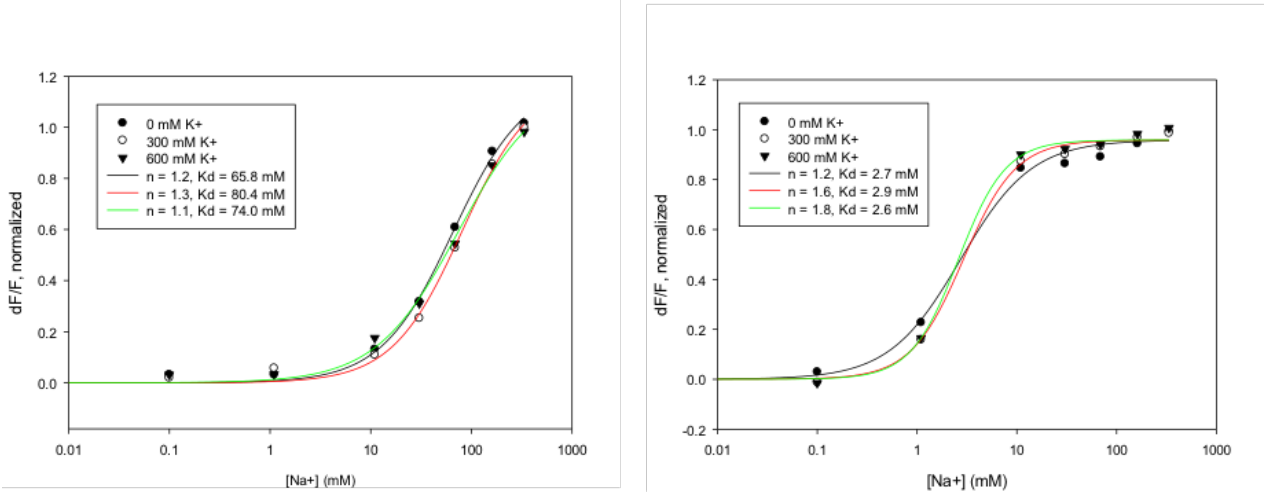

Figure A.2. Na^+ binding to wild type Glt_{Ph}. Na^+ titrations in 0 mM (filled circles), 300 mM (empty circles) and 600 mM KCl (inverted triangles) in the absence of L-asp (left) and in the presence of 10 uM L-asp (right) are shown. Ionic strength was maintained by replacement of KCl by choline chloride. All titration curves are fitted in Hill equation. Hill coefficients and Kd values are shown.

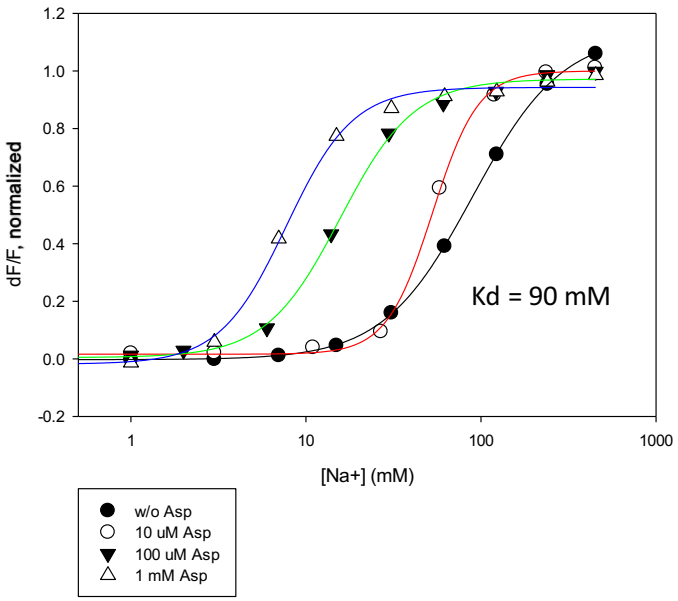

Figure A.3. Na^+ binding to R397K. Na^+ titrations in 0 mM (filled circles), 0.01 mM (empty circles), 0.1 mM (inverted triangles) and 1 mM L-asp (empty triangles) are shown. Ionic strength was maintained by replacement of KCl by choline chloride. All titration curves are fitted in Hill equation. In the absence of L-asp, Na^+ Kd is ~90 mM, similar to that of wild type.

Reduced steric hindrance between R397 and M311 increases Na^+ affinity. In the comparison of Glt_{Ph} structures in apo, Na^+-bound and asp-bound states Met 311 shows a dramatic conformational change looks flipping upon Na^+ binding (Verdon et al., 2014). In the superposition of Glt_{Ph} structures in apo state and the asp-bound state (PDB code: 3KBC and 4P19), I measured distance between the side chain of R397 in apo and the side chain of M311 in the asp-bound state. The distance was 2.2 Å, too short to avoid steric hindrance between the two residues. It implies that M311 flipping towards the substrate binding site coupled with Na^+ binding is hindered by the steric hindrance and probably the steric hindrance contributes the low Na^+ affinity of wild type Glt_{Ph}. To test that Na^+ binding is less inhibited by R397 side chain if the steric hindrance is reduced, I mutated the M311 to alanine, a smaller residue, and measure Na^+ binding. Na^+ Kd of M311A was ~22 mM, so Na^+ affinity is four-fold higher than wild type (Figure A.4). Previous asp-binding studies of this mutant showed that M311A loses Na^+/asp coupling which is tight in wild type (Verdon et al., 2014). With the increased Na^+ affinity of M311A, the previous result can be explained in a view of the steric clash between the side chains of R397 and M311: in M311A, Na^+ binding less inhibited by the side chain of R397 because the lack of the steric clash between R397 and M311. In other words, R397 movement is not coupled with Na^+ binding in M311A mutant. In M311A, even in the Na^+-bound state, the side chain of R397 can still prefer to occupy substrate-binding site like in apo state and thus does not increase substrate-binding affinity steeply, unlike in wild type.

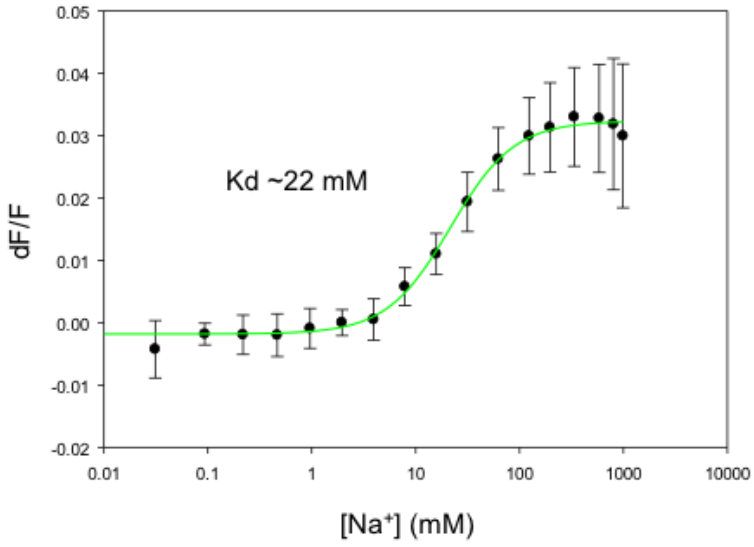

Figure A.4. Na^+ binding to M311A. Na^+ titrations in 0 mM (filled circles) L-asp. Titrations were performed in triplicate, mean values and standard errors are shown.

A.4 Discussion

In Na^+ coupled glutamate transporters EAATs and aspartate transporter Glt_{Ph}, it has been reported that Na^+ affinity to the transporters in the absence of substrates is quiet low (~100 mM) (Tao et al., 2006, Reyes et al., 2013). This low Na^+ affinity is required to maximize thermodynamic coupling of Na^+ and aspartate transport and build up a steep gradient of glutamate across the cell membrane.

In this report, I investigated Na^+ binding to a series of Glt_{Ph} mutants. I observed increase of Na^+ affinity when positive charge such as side chains of Arg 397 is removed from the substrate-binding site. Furthermore, applying a small positive ion, K^+, decrease Na^+ binding affinity in the absence of the side chain of R397. Also reducing steric clash between Arg397 and M311 shows increase of Na^+ affinity. Taken together the results, I propose a working model. In EAATs and Glt_{Ph}, a Na^+-coupled transporters with a stoichiometry of 3:1 Na^+:substrate coupling, there is a strongly conserved arginine in TM8 and the side chain occupies substrate binding site in apo state. The side chain prevents the flipping of M311 side chain, which is a hallmark of conformational change upon Na^+ binding, by steric hindrance (or electrostatic repulsive force). Thus, in the absence of substrate, EAATs and Glt_{Ph} have low Na^+ affinity. In the presence of substrate, the cooperative binding of Na^+ and aspartate can push the R397 side chain out of substrate binding site as observed in the crystal structures of Glt_{Ph} (Boudker et al., 2007, Verdon et al., 2014). Then the substrate-binding site is occupied with substrate, a negatively charged amino acid, and it allows stable M311 side chain flipping towards the substrate-binding site. In cytoplasm, a low Na^+ conditions, this process happens in reverse. Low Na^+ concentration weakens the substrate binding affinity. When

substrate unbinds from the substrate-binding site, the R397 side chain comes into substrate binding site and make M311 head outward from the substrate-binding site and accelerates Na^+ unbinding. As a result, transport cycles move in one direction and EAATs and Glt_{Ph} work as net transporters.

One of key sequence differences between glutamate transporters family and neutral amino acid transporters (ASCTs) is the presence and absence of the arginine interacting with substrate. EAATs have the strongly conserved arginine in TM8 that interacts directly with carboxyl the gamma-carboxyl group of the substrate. On the other hand, ASCTs have threonine or cysteine instead of arginine in the position and bind to neutral amino acids rather than negatively charged glutamate. Without the arginine, ASCTs have high Na^+ affinity (Na^+ K_d is ~0.2 mM in ASCT2 in the absence of substrate, personal communication with AJ Scopelliti). It makes Na^+ ions remain bound in the transporters and make the transporters exchanger rather than net transporter under physiological conditions.

A.5 Materials and methods

DNA constructs, mutagenesis, protein expression, and purification

Each mutation was introduced by PCR into Glt_{Ph} containing seven point mutations to histidine (Yernool et al., 2004), referred as wild type Glt_{Ph} for brevity. Proteins were produced in *Escherichia coli* DH10b strain (Invitrogen, Inc., Grand Island, NY) as fusions with a thrombin cleavage site, and a metal-affinity octa-histidine at their carboxyl-terminus. Proteins were purified by nickel-affinity chromatography, digested with thrombin to remove the affinity tag, and purified by size exclusion chromatography in appropriate buffers as described.

Fluorescence-based binding assays

Fluorescence-based binding assays were performed as described previously (Reyes et al., 2013). In brief, 1 μM of protein in 20 mM HEPES/Tris, pH 7.4, 200 mM choline chloride, 0.4 mM *n*-dodecyl-β-D-maltopyranoside, 200 nM styryl fluorescent dye RH421 (Invitrogen, Inc., Grand Island, NY) were titrated with NaCl at 25°C. Fluorescence experiments were carried out using a QuantaMaster (Photon International Technology, Inc., Edison, NJ). The excitation/emission wavelengths of RH421 dye were 532/628 nm. Fluorescence emissions were measured after equilibration. The data were analyzed using SigmaPlot12 (Systat software, Inc., San Jose, CA). Fractional fluorescence changes were corrected and normalized with respect to the dilution factors and maximal fluorescence changes, respectively. Corrected fluorescence changes were plotted as a function of ligand concentration and fitted to the Hill equation.

BIBLIOGRAPHY

Akyuz, N., Altman, R.B., Blanchard, S.C., and Boudker, O. (2013). Transport dynamics in a glutamate transporter homologue. Nature *502*, 114.

Akyuz, N., Georgieva, E.R., Zhou, Z., Stolzenberg, S., Cuendet, M.A., Khelashvili, G., Altman, R.B., Terry, D.S., Freed, J.H., and Weinstein, H. (2015). Transport domain unlocking sets the uptake rate of an aspartate transporter. Nature *518*, 68.

Arriza, J.L., Fairman, W.A., Wadiche, J.I., Murdoch, G.H., Kavanaugh, M.P., and Amara, S.G. (1994). Functional comparisons of three glutamate transporter subtypes cloned from human motor cortex. Journal of Neuroscience *14*, 5559–5569.

Bastug, T., Heinzelmann, G., Kuyucak, S., Salim, M., Vandenberg, R.J., and Ryan, R.M. (2012). Position of the third Na+ site in the aspartate transporter GltPh and the human glutamate transporter, EAAT1. PloS One *7*, e33058.

Bendahan, A., Armon, A., Madani, N., Kavanaugh, M.P., and Kanner, B.I. (2000). Arginine 447 plays a pivotal role in substrate interactions in a neuronal glutamate transporter. Journal of Biological Chemistry *275*, 37436–37442.

Bergles, D.E., Tzingounis, A.V., and Jahr, C.E. (2002). Comparison of coupled and uncoupled currents during glutamate uptake by GLT-1 transporters. Journal of Neuroscience *22*, 10153–10162.

Bolla, J.R., Su, C.-C., Delmar, J.A., Radhakrishnan, A., Kumar, N., Chou, T.-H., Long, F., Rajashankar, K.R., and Yu, E.W. (2015). Crystal structure of the Alcanivorax borkumensis YdaH transporter reveals an unusual topology. Nature Communications *6*, 6874.

Boudker, O., Ryan, R.M., Yernool, D., Shimamoto, K., and Gouaux, E. (2007). Coupling substrate and ion binding to extracellular gate of a sodium-dependent aspartate transporter. Nature *445*, 387.

Canul-Tec, J.C., Assal, R., Cirri, E., Legrand, P., Brier, S., Chamot-Rooke, J., and Reyes, N. (2017). Structure and allosteric inhibition of excitatory amino acid transporter 1. Nature *544*, 446–451.

Coincon, M., Uzdavinys, P., Nji, E., Dotson, D.L., Winkelmann, I., Abdul-Hussein, S., Cameron, A.D., Beckstein, O., and Drew, D. (2016). Crystal structures reveal the molecular basis of ion translocation in sodium/proton antiporters. Nature Structural & Molecular Biology *23*, 248.

Collaborative, C.P. (1994). The CCP4 suite: programs for protein crystallography. Acta Crystallographica. Section D, Biological Crystallography *50*, 760.

Crane, R.K. (1977). The gradient hypothesis and other models of carrier-mediated active transport. In Reviews of Physiology, Biochemistry and Pharmacology, Volume 78, (Springer), pp. 99–159.

Crooks, G.E., Hon, G., Chandonia, J.-M., and Brenner, S.E. (2004). WebLogo: a sequence logo generator. Genome Research *14*, 1188–1190.

Danbolt, N.C. (2001). Glutamate uptake. Progress in Neurobiology *65*, 1–105.

DeChancie, J., Shrivastava, I.H., and Bahar, I. (2011). The mechanism of substrate release by the aspartate transporter Glt Ph: insights from simulations. Molecular Biosystems *7*, 832–842.

DeLano, W.L. (2002). The PyMOL molecular graphics system. Http://pymol. Org.

Drew, D., and Boudker, O. (2016). Shared molecular mechanisms of membrane transporters. Annual Review of Biochemistry *85*, 543–572.

Emsley, P., and Cowtan, K. (2004). Coot: model-building tools for molecular graphics. Acta Crystallographica Section D: Biological Crystallography *60*, 2126–2132.

Erkens, G.B., Hänelt, I., Goudsmits, J.M., Slotboom, D.J., and van Oijen, A.M. (2013). Unsynchronised subunit motion in single trimeric sodium-coupled aspartate transporters. Nature *502*, 119.

Ewers, D., Becher, T., Machtens, J.-P., Weyand, I., and Fahlke, C. (2013). Induced fit substrate binding to an archeal glutamate transporter homologue. Proceedings of the National Academy of Sciences *110*, 12486–12491.

Fairman, W.A., Vandenberg, R.J., Arriza, J.L., Kavanaugh, M.P., and Amara, S.G. (1995). An excitatory amino-acid transporter with properties of a ligand-gated chloride channel. Nature *375*, 599.

Finn, R.D., Tate, J., Mistry, J., Coggill, P.C., Sammut, S.J., Hotz, H.-R., Ceric, G., Forslund, K., Eddy, S.R., and Sonnhammer, E.L. (2007). The Pfam protein families database. Nucleic Acids Research *36*, D281–D288.

Focke, P.J., Moenne-Loccoz, P., and Larsson, H.P. (2011). Opposite movement of the external gate of a glutamate transporter homolog upon binding cotransported sodium compared with substrate. Journal of Neuroscience *31*, 6255–6262.

Fukamachi, S., Furuta, A., Ikeda, T., Ikenoue, T., Kaneoka, T., Rothstein, J.D., and Iwaki, T. (2001). Altered expressions of glutamate transporter subtypes in rat model of neonatal cerebral hypoxia–ischemia. Developmental Brain Research *132*, 131–139.

Gaillard, I., Slotboom, D.-J., Knol, J., Lolkema, J.S., and Konings, W.N. (1996). Purification and reconstitution of the glutamate carrier GltT of the thermophilic bacterium Bacillus stearothermophilus. Biochemistry *35*, 6150–6156.

Gendreau, S., Voswinkel, S., Torres-Salazar, D., Lang, N., Heidtmann, H., Detro-Dassen, S., Schmalzing, G., Hidalgo, P., and Fahlke, C. (2004). A trimeric quaternary structure is conserved in bacterial and human glutamate transporters. Journal of Biological Chemistry *279*, 39505–39512.

Georgieva, E.R., Borbat, P.P., Ginter, C., Freed, J.H., and Boudker, O. (2013). Conformational ensemble of the sodium-coupled aspartate transporter. Nature Structural & Molecular Biology *20*, 215–221.

Grewer, C., Watzke, N., Wiessner, M., and Rauen, T. (2000). Glutamate translocation of the neuronal glutamate transporter EAAC1 occurs within milliseconds. Proceedings of the National Academy of Sciences *97*, 9706–9711.

Groeneveld, M., and Slotboom, D.-J. (2010). Na+: aspartate coupling stoichiometry in the glutamate transporter homologue GltPh. Biochemistry *49*, 3511–3513.

Guskov, A., Jensen, S., Faustino, I., Marrink, S.J., and Slotboom, D.J. (2016). Coupled binding mechanism of three sodium ions and aspartate in the glutamate transporter homologue Glt Tk. Nature Communications *7*, ncomms13420.

Hänelt, I., Wunnicke, D., Bordignon, E., Steinhoff, H.-J., and Slotboom, D.J. (2013). Conformational heterogeneity of the aspartate transporter GltPh. Nature Structural & Molecular Biology *20*, 210–214.

Hänelt, I., Jensen, S., Wunnicke, D., and Slotboom, D.J. (2015). Low affinity and slow Na+ binding precedes high affinity aspartate binding in the secondary-active transporter GltPh. Journal of Biological Chemistry *290*, 15962–15972.

Heinzelmann, G., Bastug, T., and Kuyucak, S. (2013). Mechanism and energetics of ligand release in the aspartate transporter GltPh. The Journal of Physical Chemistry B *117*, 5486–5496.

Holley, D.C., and Kavanaugh, M.P. (2009). Interactions of alkali cations with glutamate transporters. Philosophical Transactions of the Royal Society of London B: Biological Sciences *364*, 155–161.

Huang, Z., and Tajkhorshid, E. (2008). Dynamics of the extracellular gate and ion-substrate coupling in the glutamate transporter. Biophysical Journal *95*, 2292–2300.

Huang, Z., and Tajkhorshid, E. (2010). Identification of the third Na+ site and the sequence of extracellular binding events in the glutamate transporter. Biophysical Journal *99*, 1416–1425.

Humphrey, W., Dalke, A., and Schulten, K. (1996). VMD: visual molecular dynamics. Journal of Molecular Graphics *14*, 33–38.

Jensen, S., Guskov, A., Rempel, S., Hänelt, I., and Slotboom, D.J. (2013). Crystal structure of a substrate-free aspartate transporter. Nature Structural & Molecular Biology *20*, 1224–1226.

Johnson, Z.L., Cheong, C.-G., and Lee, S.-Y. (2012). Crystal structure of a concentrative nucleoside transporter from Vibrio cholerae at 2.4 Å. Nature *483*, 489.

Kim, K., Lee, S.-G., Kegelman, T.P., Su, Z.-Z., Das, S.K., Dash, R., Dasgupta, S., Barral, P.M., Hedvat, M., and Diaz, P. (2011). Role of Excitatory Amino Acid Transporter-2 (EAAT2) and glutamate in neurodegeneration: Opportunities for developing novel therapeutics. Journal of Cellular Physiology *226*, 2484–2493.

Krishnamurthy, H., and Gouaux, E. (2012). X-ray structures of LeuT in substrate-free outward-open and apo inward-open states. Nature *481*, 469.

Larkin, M., Blackshields, G., Brown, N., Chenna, R., McGettigan, P.A., McWilliam, H., Valentin, F., Wallace, I.M., Wilm, A., and Lopez, R. (2007). Clustal W and Clustal X version 2.0. Bioinformatic, 23, 2947–2948.

Larsson, H.P., Wang, X., Lev, B., Baconguis, I., Caplan, D.A., Vyleta, N.P., Koch, H.P., Diez-Sampedro, A., and Noskov, S.Y. (2010). Evidence for a third sodium-binding site in glutamate transporters suggests an ion/substrate coupling model. Proceedings of the National Academy of Sciences *107*, 13912–13917.

Lee, C., Kang, H.J., Von Ballmoos, C., Newstead, S., Uzdavinys, P., Dotson, D.L., Iwata, S., Beckstein, O., Cameron, A.D., and Drew, D. (2013). A two-domain elevator mechanism for sodium/proton antiport. Nature *501*, 573.

Levy, L.M., Warr, O., and Attwell, D. (1998). Stoichiometry of the glial glutamate transporter GLT-1 expressed inducibly in a Chinese hamster ovary cell line selected for low endogenous Na+-dependent glutamate uptake. Journal of Neuroscience *18*, 9620–9628.

Li, J., Shaikh, S.A., Enkavi, G., Wen, P.-C., Huang, Z., and Tajkhorshid, E. (2013). Transient formation of water-conducting states in membrane transporters. Proceedings of the National Academy of Sciences *110*, 7696–7701.

Mancusso, R., Gregorio, G.G., Liu, Q., and Wang, D.-N. (2012). Structure and mechanism of a bacterial sodium-dependent dicarboxylate transporter. Nature *491*, 622.

Maragakis, N.J., and Rothstein, J.D. (2004). Glutamate transporters: animal models to neurologic disease. Neurobiology of Disease *15*, 461–473.

McCoy, A.J., Grosse-Kunstleve, R.W., Adams, P.D., Winn, M.D., Storoni, L.C., and Read, R.J. (2007). Phaser crystallographic software. Journal of Applied Crystallography *40*, 658–674.

McIlwain, B.C., Vandenberg, R.J., and Ryan, R.M. (2016). Characterization of the Inward-and Outward-Facing Substrate Binding Sites of the Prokaryotic Aspartate Transporter, GltPh. Biochemistry *55*, 6801–6810.

Mulligan, C., Fitzgerald, G.A., Wang, D.-N., and Mindell, J.A. (2014). Functional characterization of a Na+-dependent dicarboxylate transporter from Vibrio cholerae. The Journal of General Physiology *143*, 745–759.

Otwinowski, Z., and Minor, W. (1997). Processing of X-ray diffraction data collected in oscillation mode. Macromol Crystallogr Part A 276: 307–326.

Owe, S.G., Marcaggi, P., and Attwell, D. (2006). The ionic stoichiometry of the GLAST glutamate transporter in salamander retinal glia. The Journal of Physiology *577*, 591–599.

Rao, V.L.R., Bowen, K.K., and Dempsey, R.J. (2001). Transient focal cerebral ischemia down-regulates glutamate transporters GLT-1 and EAAC1 expression in rat brain. Neurochemical Research *26*, 497–502.

Reyes, N., Ginter, C., and Boudker, O. (2009). Transport mechanism of a bacterial homologue of glutamate transporters. Nature *462*, 880.

Reyes, N., Oh, S., and Boudker, O. (2013). Binding thermodynamics of a glutamate transporter homolog. Nature Structural & Molecular Biology *20*, 634–640.

Rosental, N., and Kanner, B.I. (2010). A conserved methionine residue controls the substrate selectivity of a neuronal glutamate transporter. Journal of Biological Chemistry *285*, 21241–21248.

Rosental, N., Bendahan, A., and Kanner, B.I. (2006). Multiple consequences of mutating two conserved β-bridge forming residues in the translocation cycle of a neuronal glutamate transporter. Journal of Biological Chemistry *281*, 27905–27915.

Ryan, R.M., Compton, E.L., and Mindell, J.A. (2009). Functional characterization of a Na+-dependent aspartate transporter from Pyrococcus horikoshii. Journal of Biological Chemistry *284*, 17540–17548.

Ryan, R.M., Kortt, N.C., Sirivanta, T., and Vandenberg, R.J. (2010). The position of an arginine residue influences substrate affinity and K+ coupling in the human glutamate transporter, EAAT1. Journal of Neurochemistry *114*, 565–575.

Sheldon, A.L., and Robinson, M.B. (2007). The role of glutamate transporters in neurodegenerative diseases and potential opportunities for intervention. Neurochemistry International *51*, 333–355.

Shrivastava, I.H., Jiang, J., Amara, S.G., and Bahar, I. (2008). Time-resolved mechanism of extracellular gate opening and substrate binding in a glutamate transporter. Journal of Biological Chemistry *283*, 28680–28690.

Stolzenberg, S., Khelashvili, G., and Weinstein, H. (2012). Structural intermediates in a model of the substrate translocation path of the bacterial glutamate transporter homologue GltPh. The Journal of Physical Chemistry B *116*, 5372–5383.

Strong, M., Sawaya, M.R., Wang, S., Phillips, M., Cascio, D., and Eisenberg, D. (2006). Toward the structural genomics of complexes: crystal structure of a PE/PPE protein complex from Mycobacterium tuberculosis. Proceedings of the National Academy of Sciences *103*, 8060–8065.

Su, C.-C., Bolla, J.R., Kumar, N., Radhakrishnan, A., Long, F., Delmar, J.A., Chou, T.-H., Rajashankar, K.R., Shafer, W.M., and Edward, W.Y. (2015). Structure and function of Neisseria gonorrhoeae MtrF illuminates a class of antimetabolite efflux pumps. Cell Reports *11*, 61–70.

Tanaka, K., Watase, K., Manabe, T., Yamada, K., Watanabe, M., Takahashi, K., Iwama, H., Nishikawa, T., Ichihara, N., and Kikuchi, T. (1997). Epilepsy and exacerbation of brain injury in mice lacking the glutamate transporter GLT-1. Science *276*, 1699–1702.

Tao, Z., Zhang, Z., and Grewer, C. (2006). Neutralization of the aspartic acid residue Asp-367, but not Asp-454, inhibits binding of Na+ to the glutamate-free form and cycling of the glutamate transporter EAAC1. Journal of Biological Chemistry *281*, 10263–10272.

Tao, Z., Gameiro, A., and Grewer, C. (2008). Thallium ions can replace both sodium and potassium ions in the glutamate transporter excitatory amino acid carrier 1. Biochemistry *47*, 12923–12930.

Tao, Z., Rosental, N., Kanner, B.I., Gameiro, A., Mwaura, J., and Grewer, C. (2010). Mechanism of cation binding to the glutamate transporter EAAC1 probed with mutation of the conserved amino acid residue Thr101. Journal of Biological Chemistry *285*, 17725–17733.

Teichman, S., Qu, S., and Kanner, B.I. (2012). Conserved asparagine residue located in binding pocket controls cation selectivity and substrate interactions in neuronal glutamate transporter. Journal of Biological Chemistry *287*, 17198–17205.

Tzingounis, A.V., and Wadiche, J.I. (2007). Glutamate transporters: confining runaway excitation by shaping synaptic transmission. Nature Reviews. Neuroscience *8*, 935.

Vandenberg, R.J., and Ryan, R.M. (2013). Mechanisms of glutamate transport. Physiological Reviews *93*, 1621–1657.

Verdon, G., and Boudker, O. (2012). Crystal structure of an asymmetric trimer of a bacterial glutamate transporter homolog. Nature Structural & Molecular Biology *19*, 355–357.

Verdon, G., Oh, S., Serio, R.N., and Boudker, O. (2014). Coupled ion binding and structural transitions along the transport cycle of glutamate transporters. Elife *3*, e02283.

Vogt, A.D., and Di Cera, E. (2012). Conformational selection or induced fit? A critical appraisal of the kinetic mechanism. Biochemistry *51*, 5894–5902.

Wadiche, J.I., Arriza, J.L., Amara, S.G., and Kavanaugh, M.P. (1995). Kinetics of a human glutamate transporter. Neuron *14*, 1019–1027.

Wang, H., Rascoe, A.M., Holley, D.C., Gouaux, E., and Kavanaugh, M.P. (2013). Novel dicarboxylate selectivity in an insect glutamate transporter homolog. PloS One *8*, e70947.

Watase, K., Hashimoto, K., Kano, M., Yamada, K., Watanabe, M., Inoue, Y., Okuyama, S., Sakagawa, T., Ogawa, S., and Kawashima, N. (1998). Motor discoordination and increased susceptibility to cerebellar injury in GLAST mutant mice. European Journal of Neuroscience *10*, 976–988.

Weyand, S., Shimamura, T., Yajima, S., Suzuki, S., Mirza, O., Krusong, K., Carpenter, E.P., Rutherford, N.G., Hadden, J.M., and O'reilly, J. (2008). Structure and molecular mechanism of a nucleobase–cation–symport-1 family transporter. Science *322*, 709–713.

Winn, M.D., Isupov, M.N., and Murshudov, G.N. (2001). Use of TLS parameters to model anisotropic displacements in macromolecular refinement. Acta Crystallographica Section D: Biological Crystallography *57*, 122–133.

Yernool, D., Boudker, O., Jin, Y., and Gouaux, E. (2004). Structure of a glutamate transporter homologue from Pyrococcus horikoshii. Nature *431*, 811.

Yi, J.-H., and Hazell, A.S. (2006). Excitotoxic mechanisms and the role of astrocytic glutamate transporters in traumatic brain injury. Neurochemistry International *48*, 394–403.

Zerangue, N., and Kavanaugh, M.P. (1996). Flux coupling in a neuronal glutamate transporter. Nature *383*, 634.

Zomot, E., and Bahar, I. (2013). Intracellular gating in an inward-facing state of aspartate transporter GltPh is regulated by the movements of the helical hairpin HP2. Journal of Biological Chemistry *288*, 8231–8237.